UNIVERSITÀ DEGLI STUDI DI CATANIA

IN CONVENZIONE CON

UNIVERSITÀ DEGLI STUDI DI PALERMO

DOTTORATO DI RICERCA IN
SCIENZA DEI MATERIALI E
NANOTECNOLOGIE - XXXIII CICLO

ANTONINO SCANDURRA

NANO ELECTROCHEMICAL SENSORS FOR HUMAN HEALTH AND ENVIRONMENTAL MONITORING

TUTOR: PROF. SSA M.G. GRIMALDI

SUPERVISORS: PROF. S. MIRABELLA, PROF. F. RUFFINO

COORDINATORE: PROF. G. R. COMPAGNINI

TESI PER IL CONSEGUIMENTO DEL TITOLO DI DOTTORE DI RICERCA

Acknowledgements

I would like to express my sincere gratitude to my Tutor prof. Maria Grazia Grimaldi for the continuous and fair support of my PhD study and related research, for her motivation, and very competent knowledge, who provided me an opportunity to join her team as intern. Besides my Tutor, I would like to thank the rest of my thesis Committee: prof. Salvo Mirabella and prof. Francesco Ruffino for their insightful suggestions and discussions, but also for the hard question which incented me to widen my research from various perspectives.

Prof. Salvo Mirabella is also acknowledged for provided me the access to the Nano Spectro-Electrochemical Laboratory (nanoSPES) and related research facilities. Without his precious support it would not be possible to conduct this research.

The Director of the Institute for Microelectronics and Microsystems of National Research Council of Italy (CNR-IMM) dr. Vittorio Privitera is acknowledged for providing me the access to the research facilities of the “WATER

Laboratory" and Giuseppe Pantè for his technical support. Moreover, I would like to thanks dr. Alessandra Alberti (CNR-IMM) for giving me access to the XRD facility. Prof. Tony Terrasi and prof. Guido Condorelli (Università degli Studi di Catania) are acknowledged for giving me access to the XPS measurements and for useful scientific discussion. Prof. Elena Bruno (Università degli Studi di Catania) is acknowledged for her help in the ZnO NWLs synthesis and many useful scientific discussions.

Furthermore, I would like to thank Prof. Luigi Falciola, (Università degli Studi La Statale di Milano) and prof. Mohamed Boutinguiza, (Universidad de Vigo) for their unbiased and solid review of my PhD activity. Moreover I would like to thank my colleagues dr. Maria Censabella and dr. Mario Urso for the collaboration and useful discussions in many parts of the present work.

Last but not the least I would like to thank my beloved family for supporting me spiritually throughout my PhD activities and my life in general.

Catania, 12th November 2020.

Abstract

Nanostructured materials, suitable for the design and fabrication of nano electrochemical sensors of interest in human health and environmental monitoring, have been prepared and characterized. In particular:

1) Zinc oxide and zinc hydroxynitrate nanowalls for the potentiometric pH sensing;

2) nanostructures by gold layer dewetting onto graphene paper for the amperometric and voltammetric detection of glucose and fructose;

3) graphene paper- pefluorosulfonic ionomer-bismuth nanocomposite for sub-ppb heavy metal determination in drinking water by Square Wave Anodic Stripping Voltammetry (SWASV).

Fast and sensitive pH measurement is an important issue in many scientific and technological fields including health, food, environmental monitoring, and genomics. Zinc based nanostructures are very promising material for pH sensing since they allow the realization of low-cost, sustainable, and high sensitivity nanoelectrodes. The pH sensitivity reported in

literature for different ZnO nanostructures spreads from sub- to super-Nernstian, with the microscopic mechanism behind the H^+ detection often unrevealed. The proposed mechanism to explain the observed non-Nernstian behavior was based on simultaneous and independent complexing of H^+ and OH^- with preferential sites in the structures of ZnO and zinc hydroxynitrate. The reported data and the proposed modeling in this activity are useful to further develop the pH sensitivity of nanoelectrodes based on ZnO nanostructures.

Non-enzymatic electrochemical glucose and fructose sensing was obtained by gold nanostructures onto graphene paper, produced by laser or thermal dewetting of 1.6 and 8 nm-thick Au layers, respectively. Nanosecond laser annealing produces spherical nanoparticles (AuNPs) through the molten-phase dewetting of the gold layer and simultaneous exfoliation of the graphene paper. The resulting composite nanoelectrodes were characterized by X-ray Photoelectron Spectroscopy (XPS), X-ray Diffraction (XRD), Cyclic Voltammetry, Scanning Electron Microscopy (SEM), micro Raman Spectroscopy and Rutherford Backscattering Spectrometry (RBS). Laser dewetted electrode presents graphene nanoplatelets covered by spherical AuNPs. The sizes of AuNPs are in the range of 10–150 nm. A chemical shift in the XPS Au4f core-shell of 0.25–0.3 eV with respect to the Au^0 suggests the occurrence of AuNPs oxidation, which provides high stability under the electrochemical test in alkali pH.

Thermal dewetting leads to electrodes characterized by faceted not oxidized gold structures. Glucose was detected in alkali media at potential of 0.15–0.17 V vs. saturated calomel electrode (SCE), in the concentration range from 2.5 μM to 30 mM, exploiting the peak corresponding to the process of oxidation by two electrons. Sensitivity up to 1240 $\mu A \cdot mM^{-1} \cdot cm^{-2}$, detection limit of 2.5 μM and quantifications limit of 20 μM were obtained with 8 nm gold equivalent thickness. The analytical performances are very promising and competitive to the actual state of art concerning gold based electrodes. The very low detection and quantification limits and the biocompatibility of gold are compliant for glucose detection in saliva or sweat.

SWASV has been successfully employed for rapid, reliable and simultaneous determination of heavy metals at sub-ppb level in drinking water. In particular, the technique has been employed for simultaneous determination of lead and cadmium that represent two of the most poisonous heavy metals in drinking water. The key to obtain the proper analytical performance is represented by the right design of the working electrode. In this work I prepared by simple and low cost method a nanoelectrode based on graphene paper-perfluorosulfonic ionomer (nafion)-Bi composite material for the determination in the sub-ppb concentration level of lead and cadmium in drinking water. The electrode shows detection limits of 0.1 ppb for both Pb^{2+} and Cd^{2+},

respectively. The novelty of the proposed electrode consists in the starting materials and preparation process, characterized by simplicity and low cost. In particular, a key step consisting in the ion exchange of H^+ in the sulfonic groups of the ionomer with Bi^{3+} has been employed. The obtained analytical performances are very competitive with the state of art for the detection of Pb^{2+} and Cd^{2+} in solution.

Keywords: zinc oxide nanowalls; non-Nernstian response; pH sensors; graphene paper; glucose, fructose electrochemical detection; gold nanostructures; thermal and laser dewetting; perfluorosulfonic ionomer; bismuth; heavy metal trace analysis.

Content

List of Figures

List of Tables

Chapter 1. The importance being nanoelectrodes

In the last years, the advent of nanoscience and innovative techniques for the synthesis and characterization of nanomaterials contributed to great developments in electro-analysis science and technology, which led to the new branch named “electrochemical nanotechnology”. This new branch of science and technology combines electrochemical techniques with nanotechnologies to address important issues, particularly in the sensor science.

This introduction Chapter consists of two Paragraphs. In the Paragraph 1.1 the importance of the nanomaterials and an overview on their application in electro-analysis is presented;

Paragraph 1.2 describes the aim of the work done during this PhD activity.

1.1 Nanomaterials and electrochemical sensing

In the last years the use of nanomaterials in combination with electro-analysis techniques has grown considerably. Nanostructures show unique advantages over large area electrodes when used for electro-analysis: enhancement of mass transport, catalysis, high effective surface area and control over electrode microenvironment [1]. Thus, much work has been devoted to their preparation, characterization and employment in the electro-analysis of many electro-active inorganic, organic and biological species. Figure 1.1.1 shows, as example, some important applications based on electro-analysis concerning the continuous blood glucose monitoring, physiological pH monitoring through sweat, immune-sensors assay and heavy metal detection in drinking water. The most used nanomaterials in electro-analysis range roughly from individual carbon-based single and multi-walled nanotubes (CNT), nanoballs, graphene, graphite, or in combination with

oxide-hydroxides of elements with 3d orbital partially filled, or/and in combination with elements in the state of metals having 4d and 5d orbitals partially filled. Moreover, applications of various types of elemental and molecular semiconductor are reported [2]. Nanomaterials can be prepared through a variety of routes that are mainly classified as bottom up, top-down, physical, biological and chemical methods [2]. In the bottom-up process the manufacturing process involves the building up of the atom or molecular constituents. Conversely, the top-down process involves the atomization of the bulk material through a proper physical or chemical method.

The nanomaterial synthesis is very dynamic; also the complexity of preparation methods is very large. Some methods widely used are chemical vapor synthesis, gas condensation, sol-gel technique, mechanical attrition, chemical precipitation, liquid metal ion source, electro-deposition, molecular beam epitaxy, ionized cluster beam, laser beam deposition, thermal and laser dewetting, electron

beam lithography, gas aggregation of monomers, sputtering, chemical precipitation in presence of capping agents, reaction in microemulsions and autocombustion.

The intense interest towards nanomaterials is due to the unique optical, magnetic, electronic, chemical and catalyst properties, which are significant different from those of the respective bulk materials.

Figure 1.1.1 Some important applications of nanomaterials in combination with electro-analysis: A) sweat pH sensor; B) non invasive continuous glucose monitoring system; C) mobile heavy metal analyzer; D) drink water analysis at home; E) immunosensors based on electrochemical sensor.

The high cost of precious metals employed in some electro-analysis can be mitigated by nanoparticle modification

of an inexpensive base material. This approach leads to a larger surface area-to-volume ratio for the precious metal, lowering the final cost of the electrode. Moreover, the large effective surface area is characterized by a larger number of active sites that, in turn, produce an intense electrochemical response and a higher signal-to-noise ratio. It has to be underlined that voltammetry at microelectrodes, where at least one dimension is of the order of microns, implies the change in diffusive mechanisms. This allows to the possibility to explore faster kinetic processes [3].

Simm [4] reported a calculation of the effects of an array of nanoparticles on the current compared to that of a large area electrode. The peak current at a planar macroelectrode for a reversible, one electron reduction is given by the Randles-Sevčik equation (see also section 3.2.3):

$$I_{peak} = 2.686 \times 10^5 \times \sqrt[2]{n^3}\, A_{R-S}\, c_{bulk}\, \sqrt[2]{Dv} \quad \text{(eq. 1.1.1)}$$

Where I_{peak} is the peak current in Amperes, n is the number of electrons transferred, D is the diffusion coefficient,

c_{bulk} is the bulk concentration of active species in solution, ν is the scan rate and $A_{R\text{-}S}$ is the surface area of the electrode. Equation 1.1.1 shows that the peak current depends on the square root of the scan rate. The Cottrel equation, for a linear diffusion and a planar electrode conditions gives the limit of faradic current:

$$I_{lim} = nFAc_{bulk}\sqrt{\frac{D}{\pi t}} \qquad \text{(Eq. 1.1.2)}$$

Where I_{lim} is the current, F is the faraday constant, A is the electrode area c_{bulk} is the concentration of analyte, D is the diffusion coefficient of the analyte and t is the time. For a hemispherical electrode of a radius r_e the Cottrel equation for the limit current became:

$$I_{lim} = 2\pi r_e nFDc \qquad \text{(eq. 1.1.3)}$$

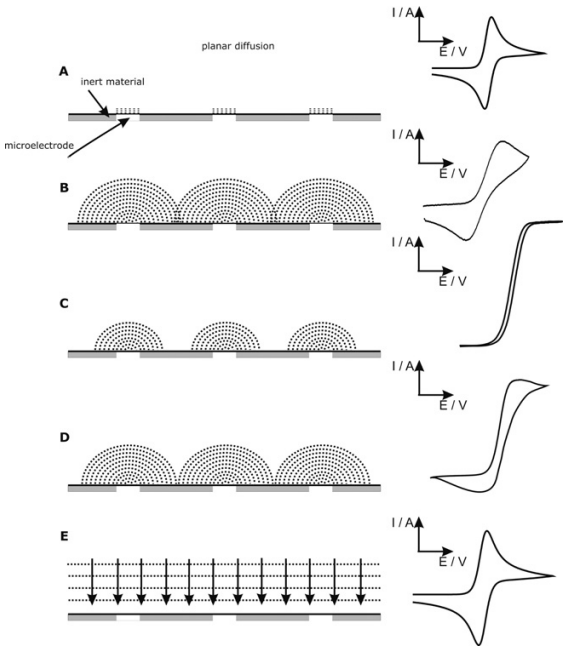

Figure 1.1.2 Schematic diagram of the categories a diffusion profile may take at a microelectrode array and the corresponding expected cyclic voltammogramms: A) diffusion layers are small relative to the magnitude of the microelectrode; B) the diffusion zones overlap with that of their nearest neighbor; C) diffusion layer is large in magnitude relative to the microelectrodes but adjacent diffusion layers do not interact; D) mixed diffusion regime is encountered between planar and hemi-spherical diffusion; E) the diffusion zones excessively exceed the insulating space between microelectrodes which results in complete overlap of diffusion zones and a planar diffusion regime. From Ref. [5].

Equation 1.1.3 is valid when $\sqrt{D\pi t} \gg r_e$ such as in presence of convergent diffusion (Figure 1.1.2) [5, 6]. In the condition of diffusional independence of each hemispherical electrode, which is considered valid when each hemispherical nanoparticle in the array has a distance of 10r from its nearest

neighbor, the total current for an area A of the nanoparticle array is:

$$I_{total} = 2\pi r_e nFDcA\,(10r)^{-2} \quad \text{(eq. 1.1.4)}$$

Equation 1.1.4 shows that, in presence of convergent diffusion, the total current of a faradic process does not depend on the scan rate. Moreover, in condition of convergent diffusion, the peak current described by the equation 1.1.1 is replaced by a current plateau. Taking into account typical values for the parameters of n=1, $D=1\times10^{-5}$ cm^2s^{-1}, c_{bulk}= 1 mM, $\nu=1\times10^{-2}$ Vs^{-1} and A=1 cm^2, the peak current for the macroelectrode can be estimated as 85×10^{-6} A. Assuming the same area of a nanoparticles array with a radius of 1 μm and 10r of spacing, the current is 6×10^{-4} A, about seven times that of the macroelectrode. When the 10r spacing is maintained, reducing the size of the nanoparticles to 100 nm means a current of 6×10^{-3} A, seventy times larger than that for the macroelectrode; even smaller nanoparticles of 10 nm bring about an increase in current over the macroelectrode of seven hundred times [6]. Example of calculation, which is

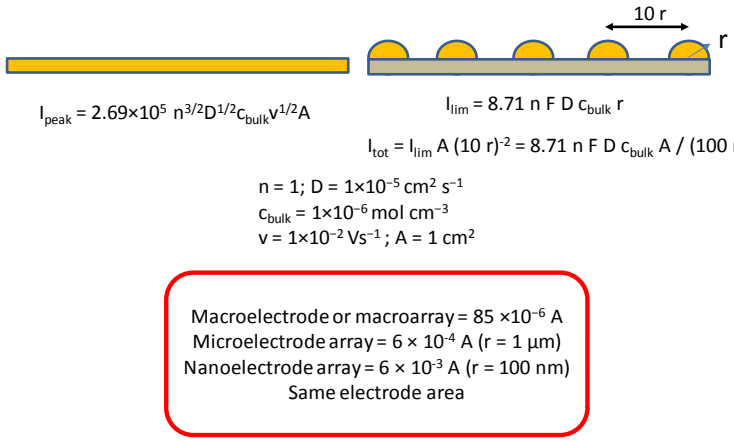

Figure 1.1.3 Current response of micro and nano electrode arrays in comparison to a macroelectrode with the same electrode area, as function of the size and spacing of single elements.

summarized in Figure 1.1.3, illustrates the great advantage in the use of an array of nanoelectrode instead of a single electrode of equivalent area. The small dimensions of nanoparticles properly spaced lead to convergent diffusion rather than linear diffusion. This condition is beneficial for a high rate of mass transport to the electrode surface. On the other hand, this condition can modify the shape of the voltammetric signal due to the increased mass transport over potential. By contrast, the catalytic properties of some nanoparticles often produce a decrease in the over potential, required for a reaction kinetically practicable. This reaction produces voltammetry that appears more reversible than that

displayed by the same material in a macroelectrode form. In a nanoparticles array electrode, the apparent peak potential depends on the effectiveness of the catalytic and mass transport parameters. This is a peculiar advantage presented by nanoparticles because a change in the position of the voltammetric peak potential arising from the species of interest can separate it from peaks due to common interferences [7]. This property produces a highly selective electrochemical analysis. In the next three Chapters 2-4, three different nanomaterials-based electrodes for as many electro-analysis applications will be presented.

1.2 Aim of this work

The nanomaterials here described are suitable for the realization of nano electrochemical sensors for electro-analysis applied in human health sciences and for environmental monitoring. The sensors were prepared preferring the simplicity, low cost and the use of minor hazardous chemical reagents. The activity was done strictly under the supervision of the Physicists of the Physics of Matter Group of the Department of Physics and Astronomy of Catania University, by exploiting the interdisciplinary skills. It is a common experience coming also from other research laboratories that the interdisciplinary collaboration gives the bests results in terms of scientific completeness and breadth of perspectives.

Three classes of nanomaterials have been prepared, characterized and employed for the fabrication of sensors in as many electro-analysis applications:

- Zinc oxide and zinc hydroxynitrate nanowalls based pH electrode (potentiometric method);
- Graphene paper – Au nanostructured electrode for the glucose and fructose sensing (voltammetric and amperometric methods);

- Graphene paper-nafion-Bi nanocomposite electrode for the detection of heavy metal ions in water (square wave anodic stripping voltammetry method).

Chapter 2. Zinc oxide and zinc hydroxynitrate nanowalls pH sensors

2.1 pH measurements and ZnO based nanoelectrodes

The burning of fossil fuels for energy production, the trees that have been cut down, the agriculture and cattle farms produce, according to the experimental observation by the scientific community and corresponding literature, the climate change in terms of global warming and rain and ocean acidification. In the late millennia the oceans had equilibrated to be slightly alkaline, with a pH of about 8.1. Human

activities have disturbed the natural value of pH. Since the start of the industrial revolution, in the middle of the 18th century, about 400 billion tons of carbon has been added to the atmosphere.

In the last decades the oceans are growing more acidic, and scientists think the change is happening faster than at any time in geologic history. Most of carbon dioxide, stays in the atmosphere (nowadays its concentration is about 400 ppm), where it traps heat and contributes to climate change. The oceans adsorb up about 25 percent of all the extra CO_2 emitted every year [8]. Over the last few hundred years, about 80 percent of all the extra carbon dioxide that human activities have added to the atmosphere has absorbed by the oceans.

It is estimated that the ocean pH decreased by 0.1 units since its monitoring due to the adsorption of extra carbon dioxide [8, 9]. This lead to destruction of the coral reefs, reduction of the population of clams with calcareous shell, as well as fish and aquatic mammal disorientation and plankton malfunction according to the reaction 2.1.1:

$CaCO_3$ (solid) + H_2O + CO_2 → $Ca(HCO_3)_2$ (soluble) (eq. 2.1.1)

Moreover, acidic rains affect forest, animals, insects and human life. Figure 2.1.1 summarizes the impact of acidic rain on the most important aspects of the planet life.

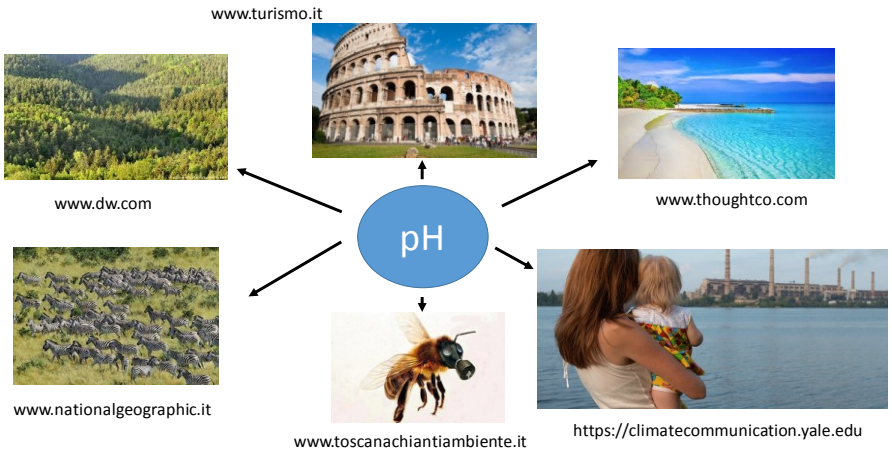

Figure 2.1.1 Effect of pH rains on several aspects of Earth's life.

All the above considerations, non-exhaustive, explain the importance of the pH monitoring using simple and low cost pH sensors. pH is the most measured physico-chemical parameter in the world [3]. Among the various sensing applications, pH measurement represents an important

prerequisite also for many industrial, biochemical and biological processes. Metal oxide based pH sensors represents a valid alternative with respect to the more expensive glass membrane pH sensors. In particular, pH sensor based on ZnO nanostructures has unique biological advantages including non-toxicity, bio-compatibility, bio-safety, high isoelectric point and high electron communication features. Moreover, zinc based nanomaterials are very promising for the realization of several applications such as gas sensing [10], heterogeneous catalysis, as well as electrochemical sensing [11-14], because the very high surface to volume ratio. In particular, ZnO is a broad band gap (3.37 eV) semiconductor, which is appropriate for ultraviolet LEDs and lasers [15, 16]. Moreover, the surface and the quantum confinement effects of ZnO in the nanoscale range make it unique in optical, electrical, mechanical, and chemical properties [17, 18].

Sensors of pH based on ZnO nanotubes [19], nanorods, [19, 20] and nanowires [21, 22] have been reported. According to Fulati [19], the sensitivity or response slope S is around 28

mV/pH for ZnO nanorods and 45 mV/pH for nanotubes. The enhanced sensitivity of nanotubes compared to nanorods has been interpreted as a result of a larger effective surface area with higher surface-to-volume ratio [19]. The response slope in a pH sensing test, representing the sensitivity of the electrode, is desirable as high as possible for the pH sensor performances. However, the response slope is an intensive property and, then, should be not related to nanoparticles extensive properties (shape, size or to surface to volume ratio). On the other hand, the response slope can be heavily dependent on various physico-chemical parameters, such as the presence on the electrode surface of many sites for H^+ binding as well as other interfering or co-adsorbed cations or anions present in the solution phase. Often, a deviation of the sensitivity of the electrode from pure Nernstian behavior (58.15 mV/pH at 20 °C) is observed. In the case of ZnO nanowires, it has been shown that after a 3% Al doping the pH response of extended gate thin transistor based sensors can be improved from 35.23 mV/pH (no Al) to 57.95 mV/pH [21, 22].

Moreover, a response slope of 59 mV/pH was found in the case of sensors based on undoped zinc nanowalls (NWLs), measured with extended gate thin transistor [23]. In the adopted condition of hydrothermal growth [23], the as grown NWLs can be a mixture of zinc oxide and zinc hydroxynitrate. Actually, the species $Zn_5(NO_3)_2(OH)_8{\cdot}2H_2O$ is the main product present in the NWLs if the pH of the bath does not exceed 6 [24, 25]. This is supported by the largest amount of standard Gibbs energy of formation ($-\Delta G_f^o$) of $Zn_5(NO_3)_2(OH)_8{\cdot}2H_2O$ i.e. -3079.89 $kJmole^{-1}$ [26]. $Zn_5(NO_3)_2(OH)_8{\cdot}2H_2O$ represents a material of the family anion-exchangeable layered double hydroxide (LDH), which consists of positively charged hydroxide layers and interlayer, charge-balancing anions [27]. Layered hydroxide zinc nitrate (LHZN) is precursor for useful two-dimensionally (2D) microstructured ZnO films materials such catalyst [28] as UV absorbents in sunscreen formulations [29] and matrices for immobilization of metal complexes and dye-sensitized solar cells [30]. LHZN has recently attracted increasing attention

from researchers worldwide due to the brucite-like structure and consequent ion exchange property and intercalation capacity. In literature the synthesis of LHZN has been reported by wet chemical processes [31], by electro-deposition [32, 33] and by chemical solution method [27]. Zinc hydroxynitrate NWLs is expected to have strong electrochemical response toward H^+ ions, due to the intercalation property and the presence of many polar sites. Nevertheless, such material is more soluble in water solution than zinc oxide [34], and upon thermal annealing at 300 °C it is converted into ZnO [35]. As a matter of fact, many different values of pH sensitivity are reported in the literature for zinc oxide based nanostructures and a straightforward comparison is difficult, given the different synthesis methods used and the lack of a proper chemical/structural characterization. The current study aims to shed light onto the involved mechanisms that influence the response slope of zinc oxide nanostructures towards the sensing of hydrogen ions in solution in the pH range comprised between 4 and 9. This pH

range is that useful in many scientific and technological fields including health [36], food [37], environmental monitoring [38], and genomics [39]. For this purpose, I investigated the electrochemical response of NWLs consisting of zinc hydroxynitrate or ZnO structures at different pH. A mechanism based on crystallographic structures for the explanation of the apparently non-Nernstian responses is proposed and discussed.

2.2 Experimental

2.2.1 Fabrication of nanoelectrodes based on ZnO and $Zn_5(NO_3)_2(OH)_8 \cdot 2H_2O$ nanowalls

ZnO nanowalls (NWLs) were grown vertically on aluminum film 65 nm thick, deposited onto silicon substrates. Pieces of Czochralski Si (100) n^+ doped with size of 1 cm × 2.5 cm and with an electrical resistivity of 0.001-0.01 Ωcm were used. Aluminum film was grown over an area of 1 cm × 1cm (see Figure 2.2.1) using dual-head magnetron Quorum Q300T D sputter.

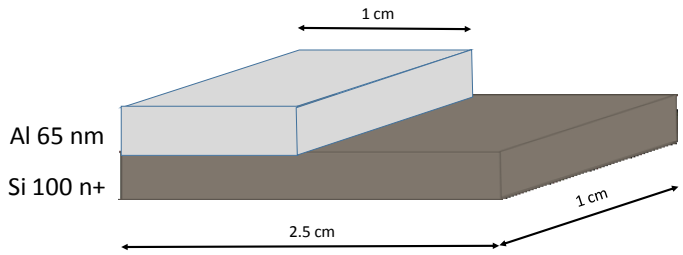

Figure 2.2.1 Schematic drawing of the electrode prepared with Si (100) n^+ substrate (thicknesses not to scale).

The sputtering rate was calibrated measuring the thickness of aluminum films by RBS.

Three series of aluminum films deposited onto quartz substrates were used for the calibration of sputtering rate. The films have nominal thicknesses of 10, 20 and 40 nm, respectively (Table 2.2.1).

Table 2.2.1 Samples used for the calibration of Al sputtering rate.

Sample name	Nominal thickness Th_{nom} (nm)	Position in the sample holder
Al5-10	10	centre
Al5-2803	20	centre
Al5-20 c1	20	centre
Al5-20 c2	20	1 cm from the centre
Al5-20 c3	20	3 cm from the centre
Al5-40	40	centre

The recipe named Al5 was used, that is characterized by the following parameters: Ar atmosphere at 10^{-3} mBar of pressure, 100 mA of plasma current at room temperature, without cleaning step. In this recipe the target was maintained slightly off-axis with respect to the 6 inch rotation stage

(sample holder). The samples Al5-20 c1-c2-c4, with nominal thickness of 20 nm were places at the center and at 1 and 3 cm from the center of the rotation stage, respectively. The aim of this experiment was to verify the homogeneity of the deposition on various positions on the area of the rotation stage. Figure 2.2.2 reports the RBS spectra of the calibration samples. The corresponding simulation curves obtained by SIMNRA software (not shown) gave the measured values of dose (at.cm^{-2}) that can be used for the thicknesses calculation, assuming an aluminum density of 6×10^{22} at.cm^{-3}. Figure 2.2.3 reports the nominal thickness (th_{nom}) versus the measured thickness (th_{meas}). The correlation between th_{nom} and th_{meas} according to the data of Figure 2.2.2 was linear with the relationship $th_{nom}=5{,}334th_{meas}-3{,}413$. Moreover, the deposition was found homogeneous within 3 cm from the center of the sample holder.

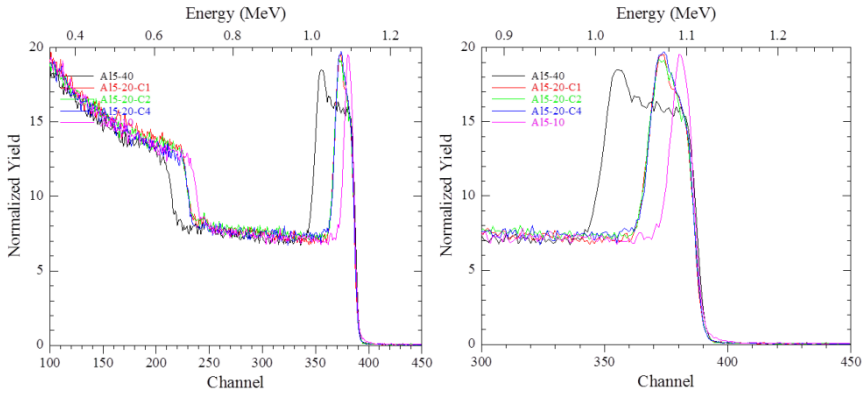

Figure 2.2.2 Rutherford Backscattering spectra of the Al films (Al5-10, Al5-20c1-c3-c4 and Al40) deposited onto quartz (right: expanded region between 0.88-1.26 MeV of the left spectra).

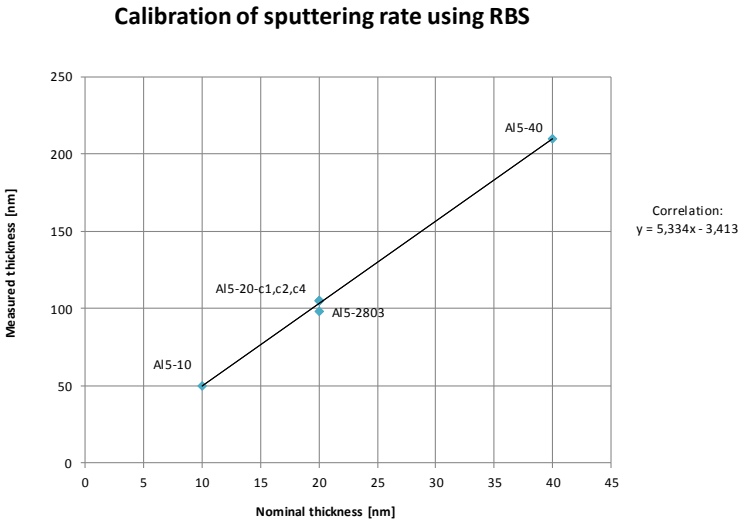

Figure 2.2.3 Correlation between nominal and measured thickness of Al film deposited onto quartz using the sputter Qurum Q300D T prepared by the recipe named Al5 (10^{-3} mBar, 100 mA, no cleaning step). Al5-10: sample having a nominal thickness of 10 nm; Al5-2803: prepared with nominal thickness of 20 nm and placed at the centre of sample holder; Al5-20-c1-c2-4: nominal thickness of 20 nm with substrates places at the center, from 1 cm and 3 cm from the center of the sample holder, respectively; Al5-40: sample with nominal thickness of 40 nm.

Basing on the calibration plot of Figure 2.2.3, the Al film having a thickness of 65 was obtained setting the sputter recipe to a nominal value of 13 nm. The substrates were cleaned with ethanol, dried with a cloth and then mounted on the rotation stage using adhesive carbon tape.

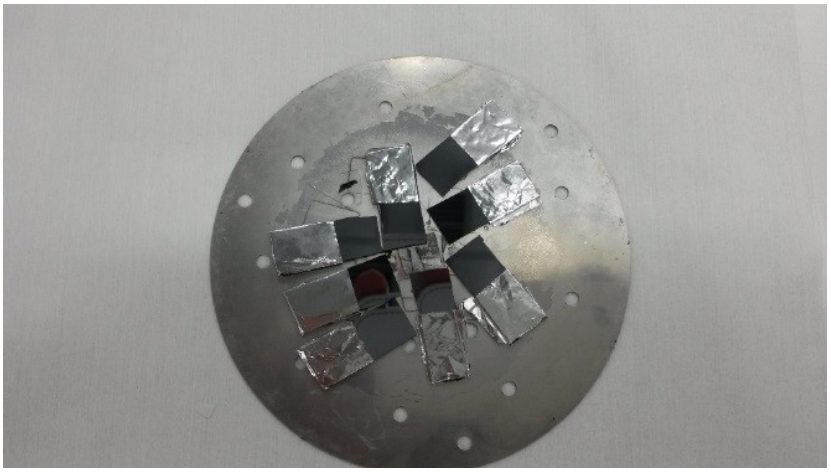

Figure 2.2.4 Picture of eight Si (100) n^+ doped electrodes mounted on the rotation stage. The portion of the electrode masked by an aluminum foil was not metalized.

Figure 2.2.4 reports the picture of the Si (100) n^+ doped electrodes mounted on the rotation stage. The portion of the electrode sputtered with aluminum had a size of 1 cm × 1 cm,

which represents the working area. The region that does not required metallization with sputtered aluminum was masked by an aluminum foil.

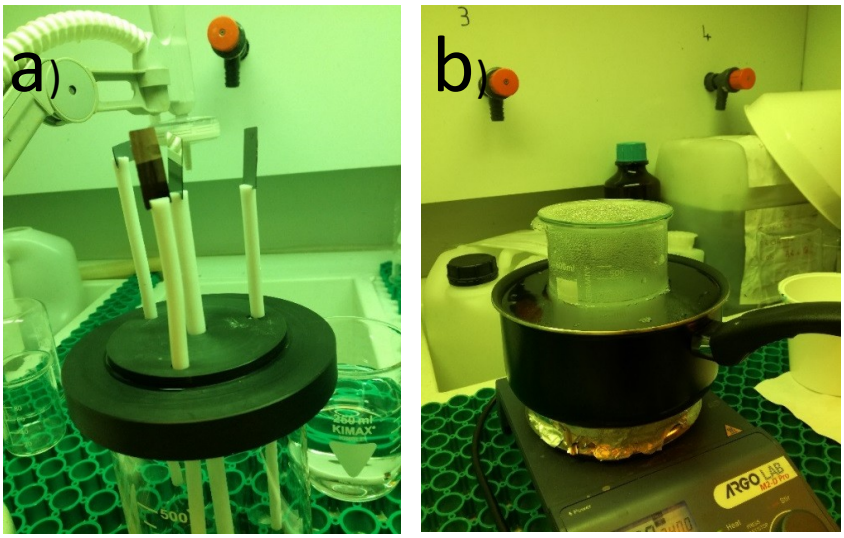

Figure 2.2.5 a) Photo of the electrodes mounted on the support for the immersion in the solution of chemical bath deposition; b) Bain-marie with the suspension of zinc hydroxide used for the chemical bath growth of the ZnO and Zn hydroxinitrate NWLs.

For the hydrothermal synthesis of zinc oxide and zinc hydroxynitrate NWLs, zinc nitrate hexahydrate ($Zn(NO_3)_2 \cdot 6H_2O$, 99.0%) and hexa-methylenetetramine

(HMTA, $(CH_2)_6N_4$, 99.5%, Merck - Sigma Aldrich) were mixed in equimolar ratio (25 mM) in de-ionized water (Milli-Q, carbon free, 18.2 MΩcm). The synthesis was performed at 90 °C, by vertically suspending the aluminum coated substrate in the growth solution (Figure 2.2.5a). The samples were subjected to hydrothermal growth for 60 minutes. Once extracted from the chemical bath, the devices were rinsed with DI water and dried with nitrogen gas. Some samples were annealed at 300 °C for 30 min in N_2 using a tubular oven Carbolite Gero. Figure 2.2.5a reports the photos of four electrodes mounted on the support for the immersion in the CBD solution (Figure 2.2.5b). In some cases, the deposition produced inhomogeneous electrodes, sometime without the ZnO NWLs layer. The inhomogeneous electrodes were discarded for further analysis. The problem faced was attributed, at least in part, to poor adhesion of the Al layer onto the Si (100) n^+ substrate. Additional cause may be the dissolution of the poorly bonded Al layer by reaction with Zn^{++} ions, forming $Al(OH)_4^-$:

$$2\ Al + 3\ Zn^{2+} \rightleftarrows 2\ Al^{3+} + 3\ Zn \qquad E^{o} = 0.9\ V$$

$$Al^{3+} + 4\ OH^{-} \rightleftarrows Al(OH)_4^{-}$$

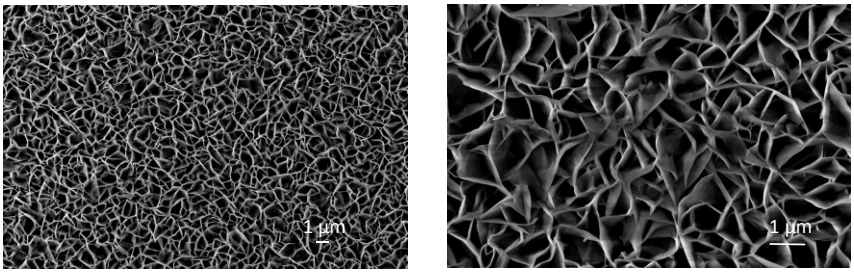

Figure 2.2.6 Scanning Electron Microscopy images of the sensing layer obtained at two magnifications. The characteristic NWLs can be observed.

The presence of ZnO NWLs and the surface morphology of the sensing layer in good electrode used in the pH measurements were screened by SEM. Figure 2.2.6 reports the SEM pictures obtained at two magnifications of a typical surface morphology. The surface is characterized by the presence of thin NWLs with the typical texturing (see Paragraph results and discussions for more detailed description).

Table 2.2.2 reports the buffer solutions traceable to standard reference materials (SRM) from NIST and PTB, used for the potentiometric characterization of the sensors.

Table 2.2.2 Buffer solutions used for the pH response measurements of the electrodes.

pH	Merch/Sigma Aldrich code	Compositions
4	1094061000	Potassium hydrogen phthalate
7	1094071000	Potassium dihydrogen phosphate/disodium hydrogen phosphate
9	1094081000	Boric acid/potassium chloride/sodium hydroxide

2.2.2 Instrumental characterizations

RBS (2.0 MeV He^+ beam, normal incidence) analysis were performed with normal detection modes (165° backscattering angle) using a 3.5 MV HVEE Singletron accelerator system.

Scanning Electron Microscopy (SEM) characterizations were obtained employing the Gemini 152 field emission Carl Zeiss Supra 25 system, at the conditions of 3 kV of accelerating voltage. The in-Lens as well as secondary electrons detectors were used.

Potentiometric measurements were done at 25 ± 1 °C in not deaerated solutions, by Versastat 4 Princeton Applied Research potentiostat. Saturated Calomel Electrode (SCE) was used as reference. 30 ml of solutions were used for each measurement. Platinum electrode was used as counter electrode.

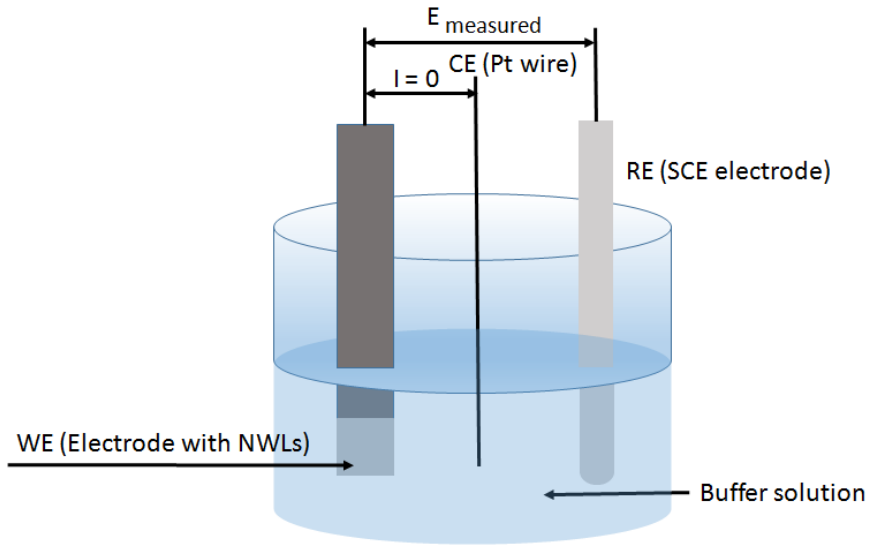

Figure 2.2.7 Schematic representation of the chronopotentiometric measurement: RE reference electrode; CE: counter electrode; WE: working electrode.

The testing of sensors was obtained measuring the potentiometric responses as function of the pH of the solutions. Buffer standard solutions were used (see Table 2.2.2). The dipped sensing area was of 1 cm^2. The test was done in chronopotentiometry mode at zero current between counter and working electrodes. This configuration is equivalent to open circuit voltage measurements. The measured values are the rest or open circuit potentials. The response was measured at pH 4, 7 and 9. Figure 2.2.7 shows

the schematic representation of the chronopotentiometric measurements. Figure 2.2.8 reports the photo of the experimental apparatus used for the chronopotentiometric measurements. The pH buffer solutions were maintained at 25 °C by means of a thermostatic bath.

Figure 2.2.8 Photo of the experimental apparatus used for the chronopotentiometric measurements of the ZnO NWLs electrodes.

Raman characterizations were done by the Horiba Jobin Yvon IHR 550 spectrometer, equipped with the laser source at

632.81 nm. The wavelength scale was calibrated assuming the Si Czochralski peak at 520.8 cm^{-1}.

XPS characterization was obtained by PHI 5600 multi technique ESCA-Auger, employing an average analysis area of 800 μm in diameter. Mg k_α X-ray source of 1253.6 eV was used. The line positions were corrected for surface charging up, assuming the C1s component of adventitious carbon at 285 eV.

2.3 Results and discussion

2.3.1 Morphology and structural characterization

The morphology of the nanoelectrodes based on ZnO and zinc hydroxynitrate NWLs was investigated by means of SEM analyses. Figure 2.3.1a reports typical SEM plan-view of the as grown sample. The surface morphology is characterized by the typical features of NWLs. The NWLs exhibit sheet thickness, which ranges between 8 to 10 nm, as extracted by direct thickness measurements made on bent NWLs that expose a cross-view to the e-beam. This data is in agreement with sheet thickness measured by transmission electron microscopy on similar structures reported by Scuderi [35]. The SEM cross-view of NWLs (Figure 2.3.1b) indicates an average vertical height of 1.7 μm. The NWLs morphology does not change significant after thermal annealing at 300 °C, as revealed by SEM plan and cross-view reported in Figures 2.3.1c and

2.3.1d, respectively. However, only a small reduction (around 200 nm) of the vertical height is revealed after annealing. According to previous works, the as grown NWLs are formed mainly of zinc hydroxynitrate [35]. In fact, the XRD patterns of the as grown sample does not show any diffraction peak related to ZnO wurzite structure, but only peaks relative to zinc hydroxynitrate $Zn_5(OH)_8(NO_3)_2$ also in the hydrate form $Zn_5(OH)_8(NO_3)_2 \cdot 2H_2O$ [35].

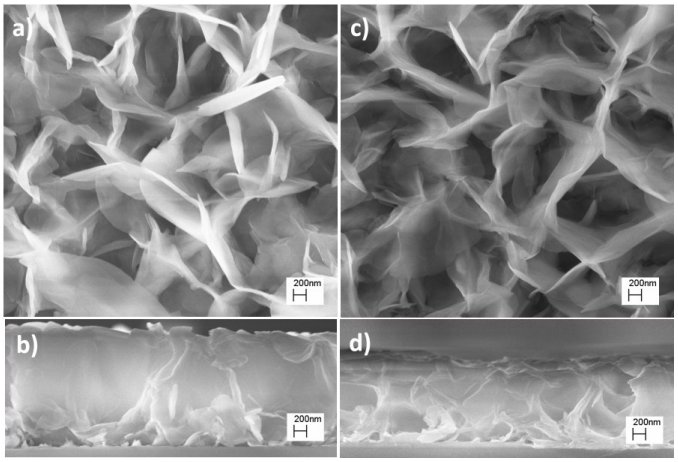

Figure 2.3.1 a) and c) Plan-view and b), d) cross-view SEM images of as grown and annealed NWLs, respectively.

After annealing at 300 °C for 1h, XRD analysis evidenced the appearance of the diffraction peaks of ZnO wurzite structure [35]. Figure 2.3.2 reports the micro Raman spectra

in the range of 100-700 cm^{-1} of as grown and annealed NWLs, respectively. The spectrum of as grown sample does not show significant Raman active transitions in the explored range, whereas the annealed sample shows characteristic peaks, at 98.28 cm^{-1} (E_{2L}), 311.36 cm^{-1} ($3E_{2H}$-E_{2L}), 370.33 cm^{-1} (A_{1T}), 436.89 cm^{-1} (E_{2H}). The peaks are observed at Raman shift with slight drift (in the range of 5-10 cm^{-1}) and different relative intensity with respect to the literature data reported for ZnO nanosheets [40]. This is caused by different crystals size and/or different wavelength of laser source used for the spectral exciting. The spectrum of annealed sample is therefore consistent with a wurtzite ZnO structure. Some marked peaks with round symbol can be attributed to zinc hydroxide species.

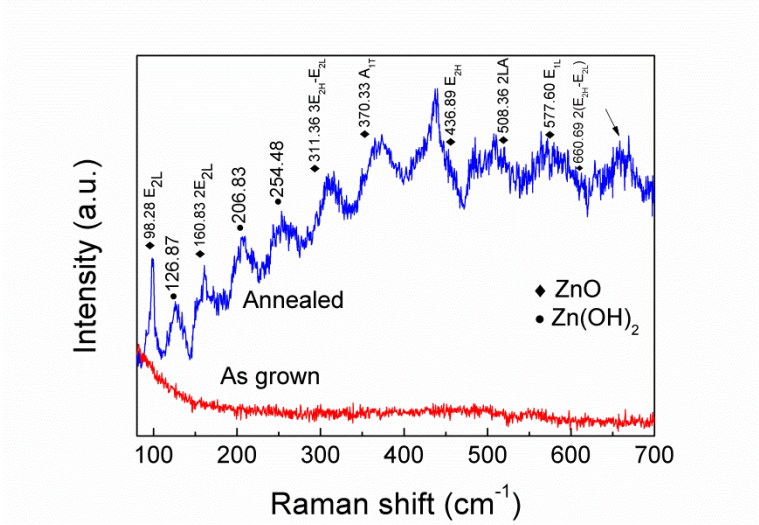

Figure 2.3.2 Micro Raman spectra of as grown and annealed NWLs, respectively.

The results of micro Raman characterizations are in agreement with that expected from the thermal annealing at 300°C, which fully converts the zinc hydroxynitrate into zinc oxide wurtzite [24, 35].

2.3.2 Potentiometric characterization

The chronopotentiometry measurements were performed using the experimental setup reported in the Paragraph 2.2.2. The electrochemical potential produced at the electrode-buffer solution is measured against the reference saturated calomel electrode. The current is fixed to zero through the sensing electrode consisting of a platinum wire. This configuration is equivalent to the open circuit potential measurement. The potential was measured as a function of elapsed time until stabilization. Figure 2.3.3a reports typical potential curves versus elapsed time obtained for the as grown NWLs electrode (zinc hydroxynitrate). The curves were acquired for the pH 4, 7 and 9 standard buffer solutions. The nanoelectrode shows good potential stability within the explored time interval. The initial part of potential curves shows transients whose duration depends on the pH of the standard buffer solutions. In particular, the conventional pH response time, which is the time required to give a stable potential for 3 sec intervals, is fast for acidic solutions and slightly increases on going from

pH 4 to pH 9. This behavior was observed also in the case of RuO_2 based pH sensor by Sardarinejad [41]. The characteristic high H^+ ion mobility and activity, where the latter is higher for acidic solutions, make achieving potential equilibrium of electrode-solution faster. The stabilization of the potential curves can be assumed complete within 30-50 s for the explored pH range.

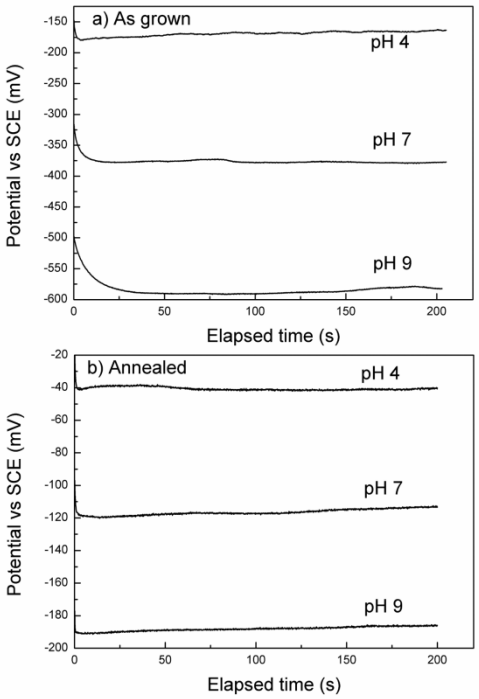

Figure 2.3.3 Potential curves versus elapsed time of NWLs electrodes: a) as grown and b) after annealing, measured at pH 4.01, 7 and 9 standard solutions.

Figure 2.3.3b reports typical potential curves versus elapsed time obtained for the annealed NWLs electrode (zinc oxide). The nanoelectrode shows good potential stability within the explored time interval. Moreover, the transients of potential are shorter for all the pH values, compared to those of as grown NWLs. This finding reflects the faster potential

equilibrium response of pure zinc oxide towards H^+ sensing than zinc hydroxynitrate.

Figure 2.3.4 reports the mean value of the potential of as grown NWLs electrode (open squares) measured at the elapsed time interval between 50 and 150 s, for the pH 4, 7 and 9 standard buffer solutions. Potential of NWLs based electrode was found linearly dependent on the pH value within the explored pH range from 4 to 9. The plot reports the linear fits. The nanoelectrode shows a very high slope value of -83.7 mV/pH. As the pH sensitivity expressed in terms of H^+ ion activity is the opposite of this slope, the as grown NWLs show a super-Nernstian behavior.

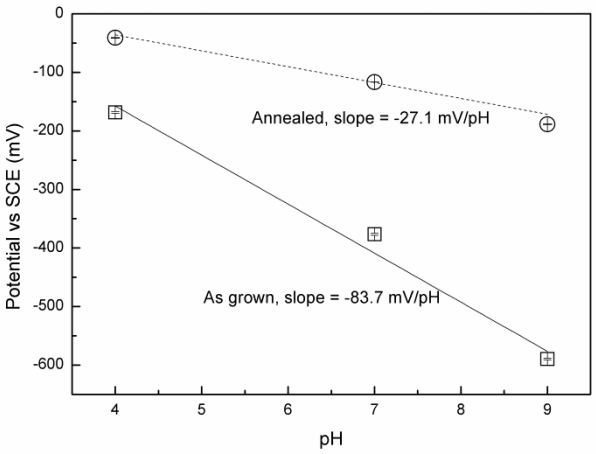

Figure 2.3.4 Equilibrium potential of the Zn based NWLs electrodes as grown (open squares) and after thermal annealing at 300 °C in N_2 (open circles). The mean value (time intervals 50-150 s) of the equilibrium potential is reported for the pH 4.01, 7 and 9 standard solutions.

Furthermore, Figure 2.3.4 reports the mean value of the potentials corresponding to the annealed NWLs electrode (open circles), measured at elapsed time intervals between 50-150 s, for the pH 4, 7 and 9 standard buffer solutions. Once again, the measurements show a good linear response, still the slope is much lower (-27.1 mV/pH) than for as grown NWLs, indicating a sub-Nernstian behavior. It is worth noting that as grown and annealed NWLs have almost the same size, shape and surface to volume ratio (see SEM pictures of Figures

2.3.1a-2.3.1b), still they show super- and sub Nernstian behavior, respectively, as the pH sensing is concerned. Table 2.3.1 reports some slope values of pH sensors from literature data for different type of nominally zinc oxide based nanostructures and the method used for the measurements.

Table 2.3.1 Response slopes for various zinc based materials from the literature.

Structure	Slope mV/pH	Method	Reference
ZnO nanorods (Hydrothermal)	-28.4 initial -26.9 after 5 days ageing	Potentiometric	[19]
ZnO nanotubes (Hydrothermal)	-45.9 initial -41.5 after 5 days ageing	Potentiometric	[19]
ZnO nanowires (Hydrothermal)	-35.23	Extended gate thin film transistor	[21, 22]
ZnO 3 % Al doped nanowires (Hydrothermal)	-57.95	Extended gate thin film transistor	[21, 22]
NWLs (As grown, hydrothermal)	-59	Extended gate thin film transistor	[23]
ZnO amorphous (sol gel deposition and calcinations)	-38	Extended gate thin film transistor	[42]
ZnO polycrystalline (RF sputter deposition)	-43.7	Potentiometric	[43]
Pure zinc oxide NWLs (Hydrothermal)	-27.1	Potentiometric	This work
Zinc hydroxynitrate NWLs (Hydrothermal)	-83.7	Potentiometric	This work

It is clear from Ref. [21] and [22] that even a little amount of aluminum oxide into the zinc oxide nanostructure can significant modifies the slope of pH response. The reported slope value varies from -27.1 to -83.7 mV/pH, depending in some cases apparently on the nanostructure shape. However, in this work the as grown NWLs and the annealed one have the same nanostructure shape, but different chemical structure. According, the pH response of the as grown NWLs is about three times larger than the annealed one. The value of -27.1 mV/pH for zinc oxide nanowalls found in this work is in good agreement with that obtained by Fulati in the case of zinc oxide nanorods of -26.9 and -28 mV/pH [19]. Then, it is clear that shape and size of nanostructures cannot account for the pH response variation. Possible explanation of these findings is discussed in the Paragraph 2.3.4.

2.3.3 Nanoelectrode surface characterization

XPS analyses were performed on both as grown and annealed NWLs electrodes after three cycles of potentiometric test at pH 7, 4 and 9. Figure 2.3.5 reports the survey XPS spectra in the binding energy region of 0-1100 eV. Both spectra show the signals assigned to Zn, Al, O and C. Table 2.3.2 summarizes the positions of the $Zn2p_{3/2}$, O1s, C1s and Al2p (unresolved) peaks with the corresponding assignments and the atomic concentrations as extracted by XPS spectra. The assignments to the various species were based on literature data [44, 45].

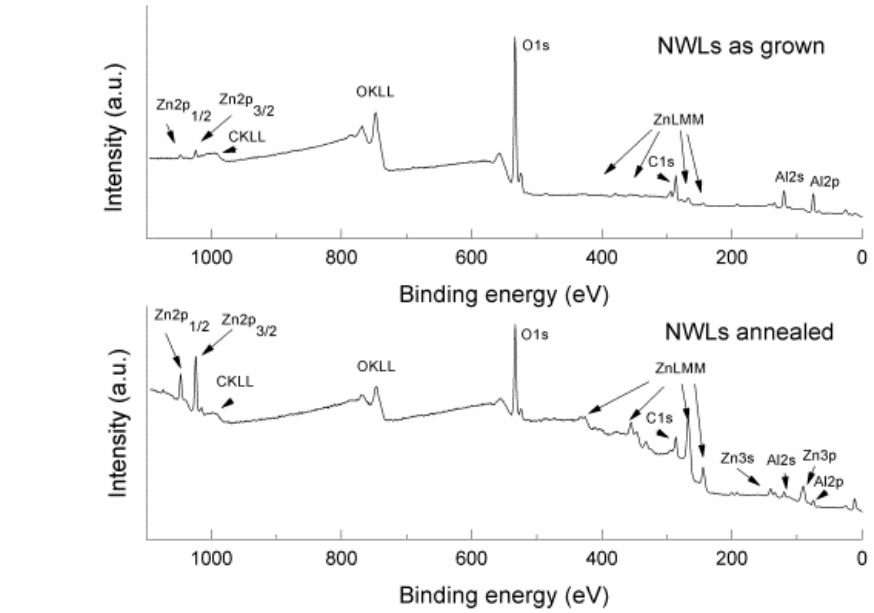

Figure 2.3.5 Survey X-ray Photoelectron spectra of annealed and as grown NWLs after 3 cycles of potentiometric test.

Table 2.3.2 XPS line positions and quantitative surface compositions of as grown and annealed NWLs after 3 cycles (pH 7, 4, 9) of potentiometric test.

Sample	As grown		Annealed	
Element	Position (eV)	% atomic conc.	Position (eV)	% At. conc.
Zn $2p_{3/2}$	1023.1 $Zn(OH)_2$	0.7	1023.3 $Zn(OH)_2$	8.8
O 1s	531.3-531.5 $Zn(OH)_2$ 532.5-532.8 $Al(OH)_3$	57.7	531.3-531.5 $Zn(OH)_2$ 532.5-532.8 $Al(OH)_3$	53.2
C 1s	285 C adventitious	21.1	285 C adventitious	27.5
Al 2p	74 $Al(OH)_3$	20.5	74 $Al(OH)_3$	10.5

Annealing seems to induce a significant variation of the surface chemical composition, as the signal of Al and O clearly gets down while the Zn peaks increase after annealing. Figure 2.3.6a reports the high resolution $Zn2p_{3/2}$ spectral regions. The binding energy of the $Zn2p_{3/2}$ was found at 1023.1 eV for the as grown NWLs and at 1023.3 eV for the annealed NWLs. Both binding energies can be assigned to zinc hydroxide specie present in the zinc hydroxynitrate and hydroxidized zinc

oxide, respectively. The binding energy of $Zn2p_{3/2}$ of zinc oxide is comprised between 1020.7 eV to 1021.2 eV, depending on the morphology of the nanostructures [46]. Then, I can rule out the presence of zinc oxide components in the investigate systems at least in the surface region. The zinc hydroxide in the annealed NWLs can be formed during the pH test, by interaction with the buffer solutions. The Al2p spectra, centered at around 74 eV, can be assigned to $Al(OH)_3$. The aluminum signals in the XPS spectra of both as grown and annealed samples are ascribed to the underlying hydroxide aluminum surface [12] and are detected from the not covered spaces in between vertically aligned NWLs.

Figure 2.3.6b reports the corresponding high resolution O1s spectral regions. Both spectra show a high full width at half maximum (FWHM) (around 2.7 eV) that clearly indicate the presence of at least two components; the first can be centered at 531.3-531.5 eV of binding energy, which is assigned to $Zn(OH)_2$ [44-46]; the second centered at 532.5-532.8 eV is assigned to $Al(OH)_3$ [44, 45].

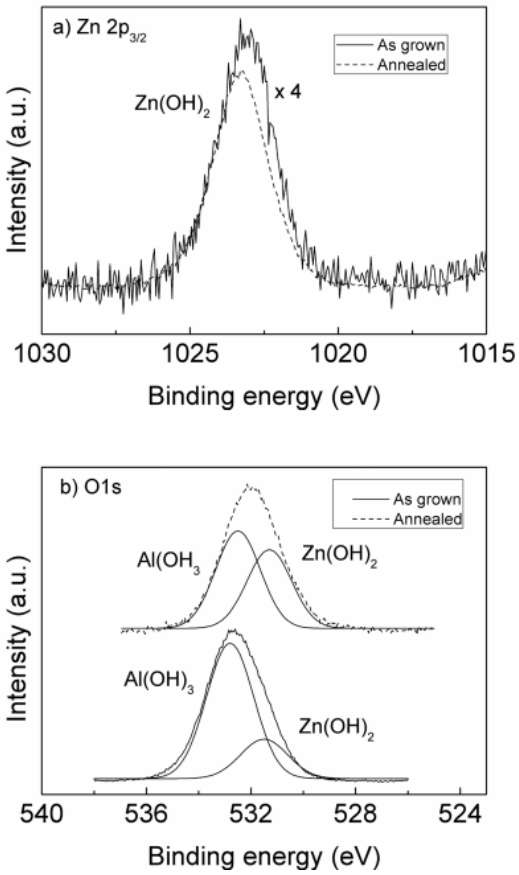

Figure 2.3.6 a) $Zn2p_{3/2}$ and b) O1s high resolution X-ray Photoelectron spectra of as grown (line) and annealed (dashed line) NWLs after potentiometric test.

In particular, the centroid of the spectrum of annealed sample is slightly shifted towards the lower side of binding energy scale. This can be thought as the results of the highest

intensity of the component assigned to zinc hydroxide with respect to the as grown sample. Such XPS data confirm the results reported in the Reference [35], as NWLs after the hydrothermal synthesis are mainly composed of zinc hydroxynitrate, while annealing induces a full transition to zinc oxide.

2.3.4 pH response modeling

The observed difference in the pH responses of as grown and annealed NWLs is explained by assuming the formation of H^+/OH^- complex in specific sites of the crystal structures (Figure 2.3.7). For the zinc hydroxyinitrate based nanoelectrode, the simultaneous and independent absorption of the H^+ ion on two different sites is proposed, while no adsorption of OH^- ion occurs because the structure presents several OH^- termination groups. In the case of zinc oxide nanoelectrode I assume that it is sensitive to both the adsorption of H^+ ions and of OH^- ions.

The pH response is then explained using the generalized model developed for ionophore-based selective electrodes (ISEs) by Amemiya [47, 48], considering the equilibrium phase boundary potentials, and the simultaneous and independent formation of complexes with two ions, I and J (i.e., H^+ on two different sites for zinc hydroxynitrate, or H^+ and OH^- for zinc oxide). The response depends on the charges

of the ion (z_I or z_J) and on the stoichiometry of the complex (1:n_I or 1:n_J). The response slope S is then:

$$E_{measured} = E + S \cdot loga_{H+} \quad S = \frac{RTln10}{z_I F}\left(\frac{1}{1-\frac{n_I z_J}{n_J z_I}}\right) \quad \text{(eq. 2.3.1)}$$

where the constant E includes the contributions rather than the phase boundary potential and the contributions that do not depend on the activity of H^+ ions in solution. Equation 2.3.1 shows that a linear response occurs among the measured open circuit potential and the pH value, and that the response slope depends on the charges of the ions (z_I or z_J) and on the stoichiometries (n_I or n_J). It should also be noted that Eq. 2.3.1 does not depend on the charge of the electrode material.

For the zinc hydroxynitrate NWLs, I assume the independent and simultaneous formation of two complexes with H^+ ions:

$$n_I\ Zn_5(NO_3)_2(OH)_8{\cdot}2H_2O + H^+ \rightleftarrows \{[Zn_5(NO_3)_2(OH)_8{\cdot}2H_2O]_{nI} : H\}^+ \quad (2.3.2)$$

$$n_J\ Zn_5(NO_3)_2(OH)_8{\cdot}2H_2O + H^+ \rightleftarrows \{[Zn_5(NO_3)_2(OH)_8{\cdot}2H_2O]_{nJ} : H\}^+ \quad (2.3.3)$$

Figure 2.3.7a illustrates the formation of these two complexes. The H atoms of the hydroxynitrate structure are not shown to facilitate visualization. By crystallographic considerations I derive that there are two different sites where H^+ can be accommodated: within the octahedral site (z_I=+1, n_I=1) or forming a bridge between two NO_3^- groups (z_J=+1, n_J=3). The structure of the zinc hydroxynitrate can be considered a structural variation of the $Zn(OH)_2$ structure, where one fourth of the octahedral Zn^{2+} cations are removed from the layer. Every octahedral site occupied by a Zn^{2+} cation shares edges with two empty and four occupied octahedra, producing a layer with a residual negative charge ($[Zn_3(OH)_8]^{2-}$) [49, 50]. In this configuration, the layer is positively charged $[Zn_3(oct.)(OH)_8Zn_2(tet.)(H_2O)_2]^{2+}$, where oct. and tet. represent the Zn^{2+} cations located in octahedral and tetrahedral sites, respectively. To neutralize the residual positive charge of the layer, nitrate anions intercalate between the layers [49, 50]. Considering the crystallographic structure of zinc hydroxynitrate reported in Figure 2.3.7a, there is 1

empty octahedral cavity for each formula unit of $Zn_5(OH)_8(NO_3)_2{\cdot}2H_2O$ where one hydrogen ion can be allocated. Moreover, in the structure I assume that there is only 1 site every 3 formula units $Zn_5(OH)_8(NO_3)_2{\cdot}2H_2O$ where H^+ ions can form hydrogen bonds bridged between two NO_3^- groups coming from two vicinal $[Zn_3(oct.)(OH)_8Zn_2(tet.)(H_2O)_2]^{2+}$ layers.

For the zinc oxide NWLs, I assume the independent and simultaneous formation of a complex with H^+ ion and a complex with OH^- ion:

$$n_I ZnO_{(S)} + H^+ \rightleftarrows \{[Zn_{(nI)}O_{(nI-1)}(OH)]\}^+_{(S)} \quad (2.3.4)$$

$$n_J ZnO_{(S)} + H_2O \rightleftarrows \{[Zn_{nJ}O_{(nJ-1)}(OH)]\}^-_{(S)} + H^+ \quad (2.3.5)$$

Figure 2.3.7b illustrates the formation of these two complexes. By crystallographic considerations I derive that I can have 1:1 complexes in any case, with $z=\pm1$.

Given these hypothesis for the two materials, Table 2.3.3 reports the pH response slopes using the Eq. 2.3.1. A super-Nernstian slope of 87 mV/decade is expected for $z_J = z_I = +1$ and stoichiometries n_I and n_J of 1 and 3, respectively. I got an

experimental value of +83.7 mV/decade for the as grown sample that is in very good agreement with the employed model. Sub-Nernstian slope of +29 mV/decade descends when z_I=+1, z_J = -1 and stoichiometries n_I=n_J=1. The experimental slope of +27.1 mV/decade obtained in the case of annealed sample fits very well with the proposed model.

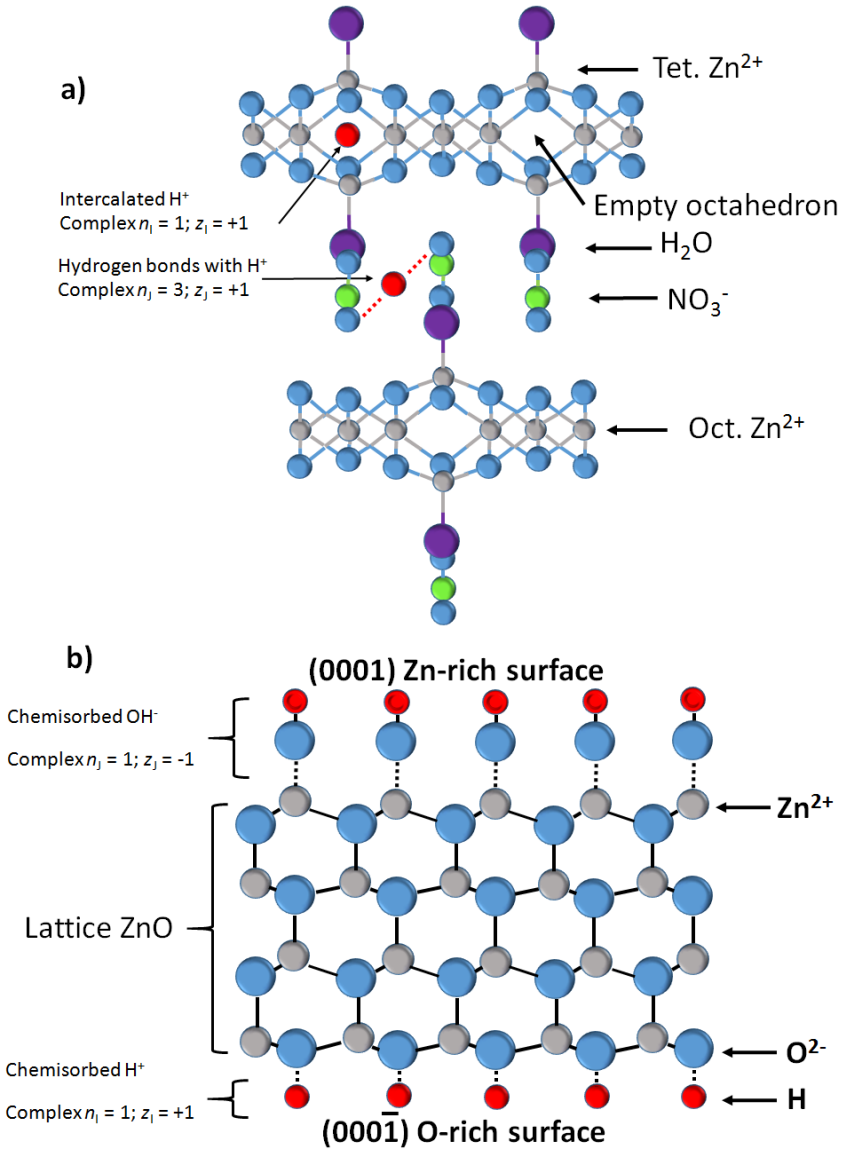

Figure 2.3.7 pH sensing mechanism through H^+/OH^- complex formation in: a) $Zn_5(OH)_8(NO_3)_2{\cdot}2H_2O$ (2 sites for H^+ complex); b) ZnO wurtzite (H^+ complex and OH^- complex). Crystal pictures modified from References [50] and [51].

Table 2.3.3 pH response slopes calculated according to the proposed model assuming the simultaneous and independent formation of complexes with two ions. z_I or z_J represents the charge of the two ions while 1:n_I or 1:n_J is the stoichiometry of the two complexes.

Structure	Charge		Stoichiometry		Response slope mV /decade	
	z_I	z_J	n_I	n_J	Model	Experimental
As grown	+1	+1	1	3	+87	+83.7
Annealed	+1	-1	1	1	+29	+27.1

2.4 Conclusions

The involved microscopic mechanisms that influence the sensitivity of pH sensors based on zinc oxide nanostructures have been studied. By chemical bath deposition I grew nanowalls made of zinc hydroxynitrate or ZnO structures and evaluated the potentiometric response to pH 4, 7 and 9 standard solutions. Zinc hydroxynitrate showed a super-Nernstian behavior (+83.7 mV/decade) with transient response depending on the pH value. This was explained with the insertion of H^+ into octahedral empty sites and with a secondary simultaneous and independent complexing of H^+ that forms bridging bond between two NO_3^- groups from two vicinal zinc hydroxide layers. Zinc oxide NWLs showed a sub-Nernstian behavior (+27.1 mV/decade) with transient response almost independent of the pH value. In this case a simultaneous and independent response to H^+ and OH^- of zinc oxide explain the evidenced sensitivity. In a similar manner here reported, the described model could explain the different

literature data, if all the involved parameters are fully taken into accounts. From a practical point of view, zinc oxide nanowalls confirm their sensitivity toward H^+ activity in solution and their great potential to be used as disposable, low cost, environmental friendly nanoscale pH sensors.

Chapter 3. Gold nanostructures for glucose and fructose sensing

3.1 The challenge of non-enzymatic electrochemical sensing of glucose and fructose

Glucose and fructose determination by fast and reliable and user friendly method is still a challenge in several scientific and technological fields including health [52], food [53], environmental monitoring [54], and genomics [55]. In particular, dating to 2014 it was estimated that over 422 million people throughout the world suffer from diabetic

pathologies [56]. In this regard, in the insulin-dependent diabetes up to 300 monitoring of glucose per month are needed for the patients. To make the patient life acceptable, in the last year continuous non-invasive glucose monitoring and self-monitoring glucose systems have been developed [57]. Applications include clinical, hospital and home settings, where the major cost is represented by the sensor [58]. The global glucose biosensor market was estimated at USD 15.3 billion in 2015, which account for approximately 85% of the biosensor industry, making the glucose sensors a highly active area of sensor research. Figure 3.1.1 reports the global glucose monitoring system market forecast 2019-2028 [58, 59]. For a continuous glucose monitoring applications (Figure 3.1.2), among to the sensors based on spectroscopy [60], chromatography [61] or colorimetry [62] principles, electrochemical sensors are attractive due to low-cost, simplicity, and reliability [63].

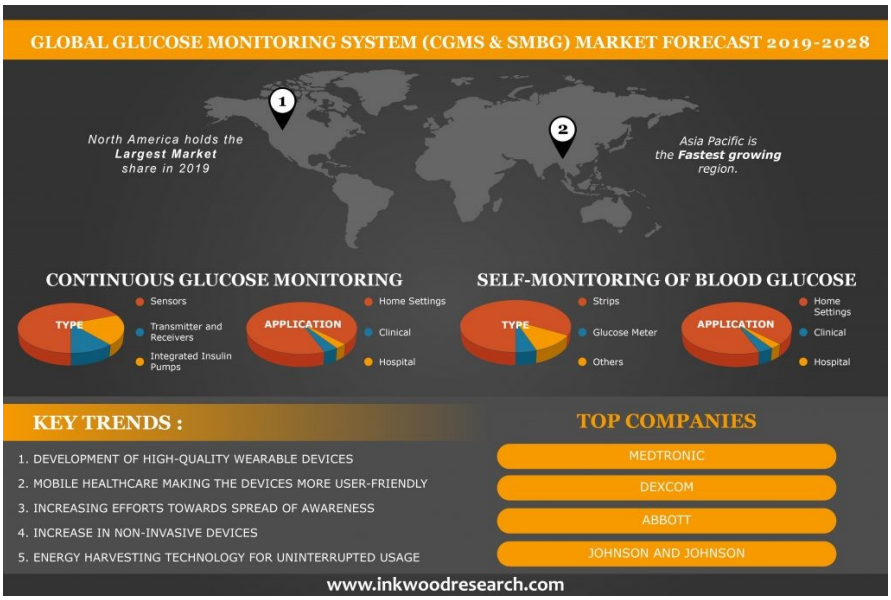

Figure 3.1.1 Global glucose monitoring system market forecast 2019-2028 source: Ref. [58]. Available online at: www.inkwoodresearch.com (accessed on May 14, 2020).

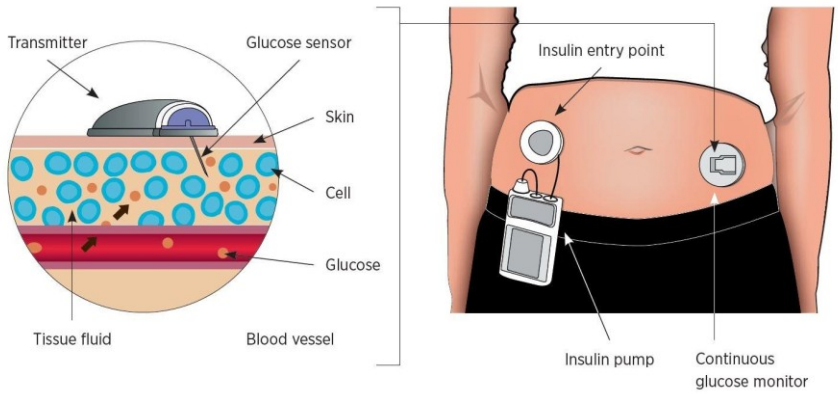

Source: www.topimages.com

Figure 3.1.2 Example of typical continuous glucose monitoring system.

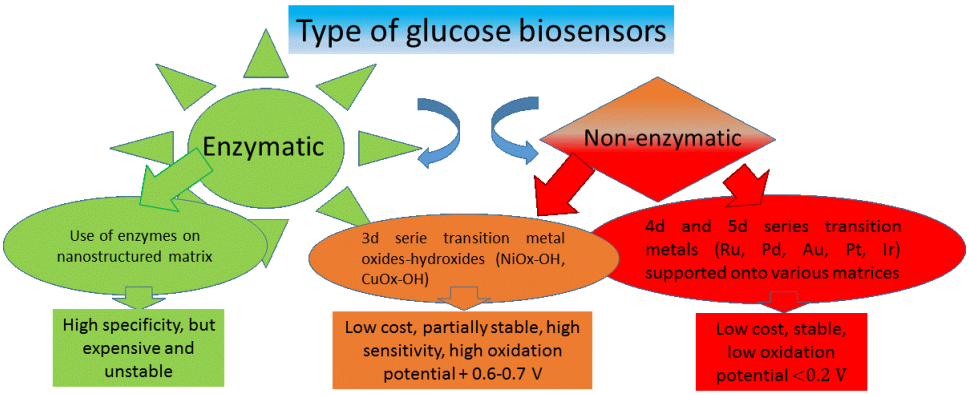

Figure 3.1.3 Scheme of various types of glucose biosensors.

The glucose electrochemical sensors can be divided into two main categories: enzymatic and non-enzymatic (Figure 3.1.3). Although glucose oxidase (GOx) has been widely used to fabricate various kinds of enzymatic amperometric biosensors for detection of glucose due to its specificity, the enzymatic modified electrodes have some drawbacks such as high price, limited conditions of use (easily affected by temperature, pH, humidity, and toxic chemicals) and complex immobilization procedures [64-69].

The non-enzymatic electrochemical sensors provide several advantages, such as higher stability, lower production costs and tolerance to broader range of operating conditions [70, 71]. Several classes of nanomaterials such as 3d block metal oxides/hydroxides-based nanostructures supported onto carbon nanotubes, nanowires, graphene and polymers, are widely investigated to make biosensors with fast response, high sensitivity, high stability and user-friendly [72-76]. In these devices the enzymatic activity of the enzymes is mimicked by the catalytic activity of inorganic nanomaterials, such as copper or nickel oxides being more stable and versatile. Numerous recent works reported that glucose molecules are oxidized on the electrode surface by CuOOH or NiOOH species to radical intermediates that are rapidly converted to gluconolactone [77]. The produced $Cu(OH)_2$ or $Ni(OH)_2$ species are reconverted into CuOOH or NiOOH by applying a specific potential. This class of sensors has been demonstrated to work for the detection of fructose too [78]. In particular, copper oxide-hydroxides based sensors are

characterized by significant sensitivity. Copper oxide nanowires supported unto copper foam structures showed sensitivity up to several thousand of $\mu A \cdot mM^{-1} \cdot cm^{-2}$ [79]. Despite the high sensitivity, this class of sensors is characterized by relatively high oxidation potential, in the range of 0.4-0.7 V, with very broad faradic peaks up to 0.7 V. These characteristics could cause lack of specificity in presence of interfering redox active species. Usually, the preparation procedures are complex and produce a lot of dangerous waste.

Other class of non-enzymatic electrochemical glucose sensors is based on nanostructures of 4d and 5d blocks metals such as palladium, platinum and gold, being the latter the most used for its high electro-catalytic activity capable to mimic the enzymatic activity of GOx [80-82]. It has proven that the electro-catalytic activity towards glucose oxidation is presented by nanostructured gold surfaces, conversely to flat gold surfaces that do not exhibit activity [83]. Electro-catalytic activity of gold is based on the reaction:

AuOH + glucose → Au + gluconolactone

OH^- ions in alkali media strongly adsorb to the surface of gold nanoelectrode and mediate the conversion of glucose. Electrodes based on gold nanostructures present a low oxidation potential of glucose, around 0.2 V, which is preferable to obtain high sensor specificity and low interference by other organic redox active materials.

In recent years, many nanostructured and porous gold surfaces [83, 84], gold nanoparticles [85], nanocomposites [86, 87], graphene and carbon nanotubes based nanostructures [88, 89] have been prepared for the glucose electro-oxidation and sensitive detection. The most common fabrication methods of nanostructured gold electrodes include chemical [90] and electrochemical etching [91], electrochemical dealloying [92], direct electrochemical deposition and electro-deposition in pores of the template [93], electrochemical deposition in hydrophilic gel templates– gelatin and agarose [80].

Solid state dewetting of gold thin films has several advantages for producing metal nanostructures with respect to the former fabrication methods [94]. In particular, solid state dewetting, obtained at temperature below the metal melting point, is suitable for producing nanoparticles arrays over a large area [95]. The average size and separation of metal nanostructures can be controlled with the initial thickness of a thin metal film. However, the simultaneous fabrication of narrow spaced and large size area of nanostructures still remains challenging. In fact, as the film thickness increases, both the average nanostructures size and the interstitial spacing simultaneously increase after solid state dewetting process. Solid state dewetting in metals depends, in addition to the initial film thickness, on many factors, including the high melting point of most metals, thermal diffusivity and self diffusion coefficient. Dewetting of thin films is caused by a hydrodynamic instability which occurs when attractive intermolecular forces overcome the stabilizing effect of interfacial tension [96]. Moreover, metal dewetting under

conventional long-time annealing is complicated and influenced by additional phenomena such as surface processes including metal-substrate chemical interactions and metal diffusion into the substrate. Thus, the reproducibility of thermal dewetting processes is guarantee by proper optimization of the experimental parameters (film thickness, temperature and duration of dewetting). The experimental parameters of thermal process influence the particles size, size distribution and surface density [97, 98]. On the other hand, temperature dewetting above the melting point of electro-active metal films such as Ag, Au, Cu, and Ni is a challenging task. High temperatures amplify the effects of interfacial interactions and metal diffusion, which further complicate dewetting. In order to overcome this difficulty, nanosecond pulsed laser heating technique to raise the temperature, in a controllable and rapid manner, has been proposed. In this experiment, the solid metal film can be melted and subsequently undergo morphological changes due to dewetting. In several cases, dewetting with characteristics

similar to that for spinodally unstable polymer systems was observed [99, 100]. In this regards, the substrate used for the realization of the nanoelectrode represents an important issue. The advantages of carbon materials used as substrate include low cost, wide electrochemical potential window, and the possibility of a variety of chemical functionalization [101]. Furthermore, the use of carbon materials, which are characterized by relatively poor electrochemical activity with respect to metal substrates, reduces the interference in the detection of the analyte. In particular, graphene-based materials are very promising for their high electrical conductivity and large electrochemical potential window (~2.5 V in 0.1 mM phosphate buffered saline) [102]. Recently, a number of works have demonstrated that graphene-nanoparticle hybrid structures can act synergistically to offer a number of unique physicochemical properties that are desirable and advantageous for sensing applications. They display the individual properties of the nanoparticles and of graphene, but they can also exhibit additional synergistic

properties thereby enhancing the achievable sensitivity and selectivity using a variety of sensing mechanisms [103].

Wan, described the preparation of large sized graphene sheets to fabricate lightweight and flexible graphene paper with remarkable performances of electromagnetic interference shielding, higher electrical conductivity and strength [104]. Large sized graphene sheets compared to the smaller sized show fewer defects and more conjugated carbon domain size as well as better alignment. Large sized graphene sheets were obtained by reduction process of graphene oxide sheets, which were first separated from as prepared graphene oxide solution by centrifugation with different rotating speed. After filtration and chemical reduction process, the graphene paper was subjected to a typical annealing at 1600 °C for 60 min.

Herein, I used graphene paper as substrate to prepare graphene-gold nanostructured electrodes for glucose and fructose detection. The material possesses a high electrical conductivity, similar to that of metals, and is characterized by enhanced electron transfer at the electrode surface. These

properties make direct electronic conduction without the use of an additional conductive path material. The fabrication processes and the characterization of nanoelectrodes for glucose and fructose monitoring are presented and discussed. The fabrication processes consist on the solid state dewetting (thermal) or liquid state dewetting (laser) [105] of 1.6 and 8 nm layer of gold deposited onto graphene paper. The main difference exhibited by the solid state and liquid state dewetting process lies in the size and shape of the resulting gold nanoparticles: liquid state dewetting originate smaller particles than that obtained by solid state dewetting. In addition, the particles obtained by liquid state dewetting are almost spherical, while those obtained by the solid state process present a characteristic faceting. The electrodes were characterized by SEM, Micro Raman Spectroscopy, XRD, RBS and Cyclic Voltammetry. The electro-catalytic activities toward glucose and fructose oxidation in alkali phosphate buffer solution are presented and discussed.

3.2 Experimental

3.2.1 Fabrication of nanoelectrodes for the determination of glucose and fructose

D-(+)-glucose, D-(-)-fructose, phosphate buffer solution at pH 12 and graphene paper foil 240 μm thick (XG Sciences) were purchased from Sigma Aldrich, Milan, Italy. Others reagents were also of analytical grade and used as received, and all aqueous solutions were made using Milli-Q water.

Electrodes consist of gold nanoparticles prepared onto graphene paper (GP-AuNPs). Graphene paper is suitable for a wide variety of applications to optimize thermal conductivity, thermal spreading, electrical properties, corrosion resistance and sensing. Graphene paper is a thin, flexible, and lightweight sheet, obtained by tailoring the composition, density and manufacturing process. The main physical properties are (data sheet supplied by the producer and available online at: www.sigmaaldrich.com):

• Thermal conductivity: 550 W/mK (in-plane), 3 W/mK (through plane).

• Electrical conductivity: 3700 Scm^{-1} (in-plane).

• Electrical resistivity: surface 0.06 Ω/sq, sheet 2.7 μΩ·m.

• EMI shielding: 53 dB @ 30 MHz, 58 dB @ 1.5 GHz.

In this research activity graphene paper was used with multi-functional scopes, as support, active material and conductive path for the realization of electrochemical sensors. The high electrical conductivity of graphene paper avoids the use of an additional conductive path for the realization of the sensors.

Pieces of graphene paper of measuring 1 cm × 2.5 cm were used. Au films (1.6 or 8 nm thick) were sputtered onto 1 cm × 1 cm of the support area, leaving the remaining surface not metalized (Figure 3.2.1a). The gold films were deposited by sputtering using the Emitech K550X sputter coater. The conditions of 50 mA, 40 s and 10 mA, 60 s of plasma current and time deposition were used for 8 nm and 1.6 nm of Au, respectively. Molten-phase dewetting of gold layer was

obtained by nanosecond laser annealing using a pulsed (10 ns) Nd: yttrium aluminum garnet laser operating at 532 nm (Figure 3.2.1b). To irradiate surface area of 1 cm × 1 cm on the sample, several nearby single beam spots were overlapped (Figure 3.2.1c).

Solid state dewetting (thermal dewetting) of gold layer was done by a tubular horizontal oven Carbolite Gero. The annealing was done at the conditions of 300, 400 and 500 °C, N_2, 1 hour.

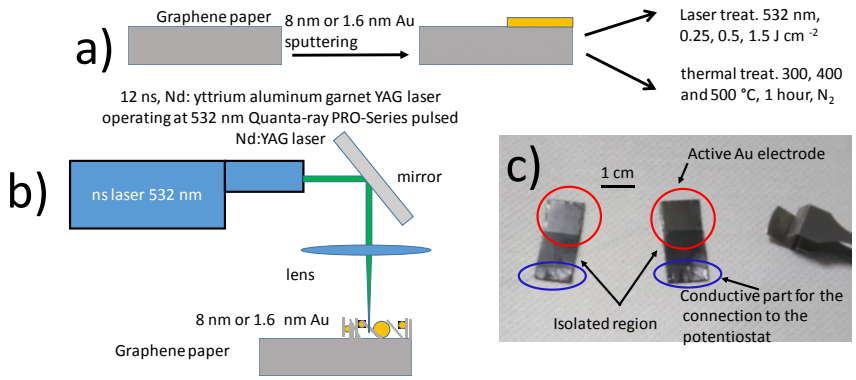

Figure 3.2.1 a) Scheme of the procedure used for the laser or thermal dewetted electrodes; b) laser irradiation of samples; c) photo of the electrodes used for the glucose and fructose sensing.

3.2.2 Instrumental characterizations

Cyclic voltammograms and current responses were used to investigate the electro-catalytic oxidation properties of GP-AuNPs nanoelectrodes towards glucose and fructose. The measurements were done in phosphate buffer solution at pH 12. The presence of buffer guarantees the pH value that would be modified by the neutralization reaction with gluconic acid to gluconate. Before the acquisition of glucose and fructose voltammograms, the electrodes were cleaned by 5 cycles between -0.5/+1 V, in phosphate buffer solution at pH 12. Cyclic voltammograms were obtained at a scan rate of 0.020 Vs^{-1}. XRD measurements were done by a D8-Discover Bruker AXS diffractometer equipped with a Cu-Kα source/Goebel mirror and soller slits at the primary beam, and with variable slits and detector at the secondary pathway. Symmetric and grazing incidence configurations are used for a complete characterization of the layers.

XPS characterization was obtained by VG Microtech CLAM4 instrument equipped with a multi-channeltron

detector (MCD) and a hemispherical electron analyzer. Mg k_α X-ray source of 1253.6 eV was used. The line positions were corrected for surface charging up assuming the Au $4f_{7/2}$ line at 84 eV.

For the description and characteristics of the other instrumental characterizations see Paragraph 2.2.2.

3.3 Results and discussions

3.3.1 Micro Raman and XRD characterization of graphene paper

Figure 3.3.1 reports the micro Raman spectra of pristine graphene paper and after thermal treatment at 500 °C, 1h in N_2, and laser irradiation at fluence of 1.5 Jcm^{-2}. The sample treated at 500 °C was analyzed in a flat region and over a bump, which is likely produced by thermal blistering. The spectrum of pristine graphene paper shows a first order peak centered at 1581.4 cm^{-1}, assigned to G-peak, and a second order broad signal centered at about 2689.9 cm^{-1}, assigned to 2D-peak. Similar assignments were done for the spectra of thermally and laser treated samples. These results indicate that significant structural disorder of the substrate can be ruled out under the explored conditions. In graphene-based materials, there are three main peaks that are

characteristically observed in the micro Raman spectrum [106].

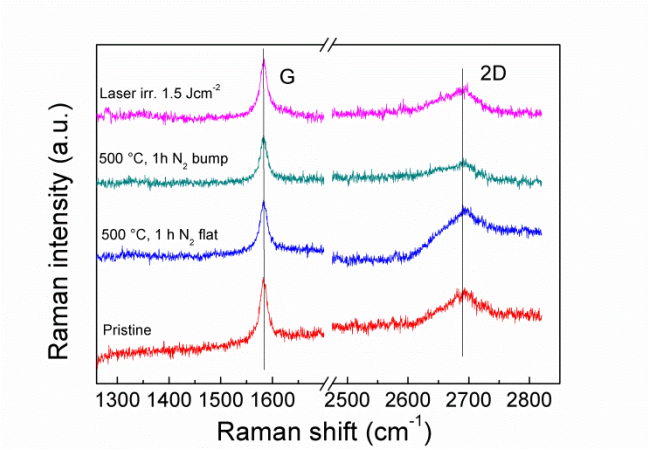

Figure 3.3.1 Micro Raman spectra of pristine graphene paper (red line), after thermal treatment at 500°C, 1h in N_2 (blue line) and after laser irradiation at fluence of 1.5 Jcm^{-2} (magenta line).

Specifically, these are known as the D-peak, G-peak and 2D-peak. The G-peak is a first order transition assigned to the in-plane carbon-carbon bond stretching, while the existence of D-peak at about 1350 cm^{-1} indicates the presence of impurities or structural disorder e.g. in graphene oxide or doped material [106, 107]. The 2D-peak is produced by second order two phonon process. The G and 2D Raman peaks change in shape, position and relative intensity with number of graphene

layers. This reflects the evolution of the electronic structure and electron–phonon interactions [108-111]. The Raman shifts of G and 2D peaks observed in this study are close to that of highly oriented pyrolytic graphite (HOPG). The Raman spectrum of HOPG consists of two main peaks at 1581 and 2687 cm^{-1}, which are assigned to the G-peak and 2D-peak, respectively [108-111].

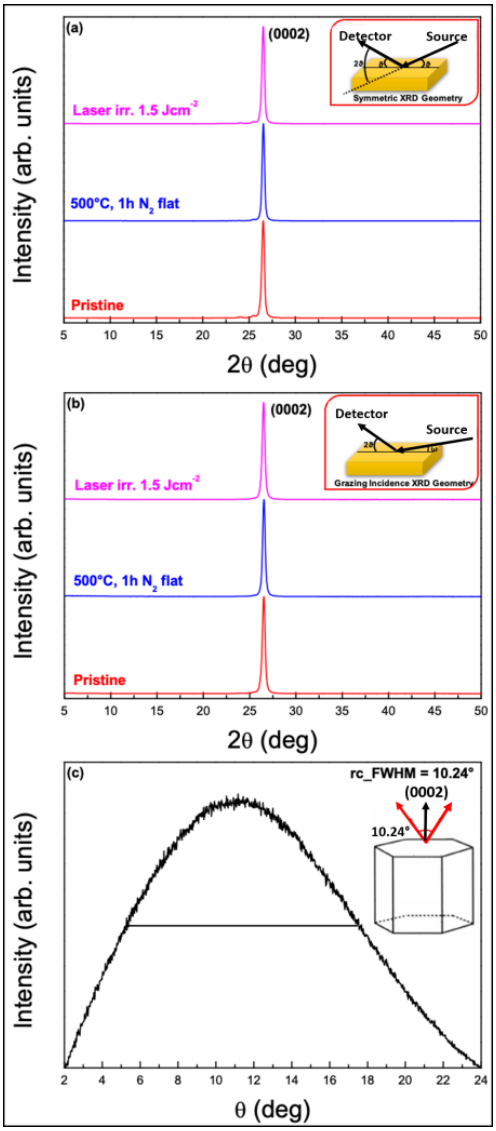

Figure 3.3.2 X-ray Diffraction patterns in (a) symmetric geometry and in (b) grazing incidence geometry of pristine sample (red line), after thermal treatment at 500°C, 1h in N_2 (blue line) and after laser irradiation at fluence of 1.5 Jcm^{-2} (magenta line). (c) Rocking curve taken at 2ϑ = 26.54° with FWHM = 10.24°.

Figure 3.3.2 shows the XRD patterns acquired in symmetric geometry (a) and in grazing incidence geometry (b) of pristine sample, after thermal treatment at 500°C, 1h in N_2, and after laser irradiation at fluence of 1.5 Jcm^{-2}. In both diffraction geometries, only one peak at $2\vartheta = 26.54°$ is observed i.e. the main graphite contribution (symmetric group P63/mmc) corresponding to the (0002) crystallographic planes, with growth axis along the [0001] direction. The patterns in Figures 3.3.2a, and 3.3.2b, according to Johra [112], do not contain specific features to be attributed to single graphene layers or graphene oxides. Figure 3.3.2c shows the rocking curve taken at $2\vartheta = 26.54°$ as representative of all the analyzed samples. The full width at half maximum (FWHM) along the (0002) plane is 10.24° and represents the spread of the growth axis. All the samples analyzed share similar lattice structure. According to the Raman spectra, the XRD characterization is consistent with a material having a high degree of structural order.

3.3.2 Morphology characterization of laser irradiated graphene paper

Figure 3.3.3 reports typical SEM pictures of pristine graphene paper (a, b) and after laser irradiation at fluence of 0.25 Jcm^{-2} (c, d), 0.5 Jcm^{-2} (e, f) and 1.5 Jcm^{-2} (g, h), respectively. The picture of pristine sample shows overlapped flat layers with different orientation. In addition, defects consisting of cracks and voids are present. The laser irradiation induces the graphene paper exfoliation, visible by the presence of numerous nanosheets. Moreover, some bright spots with a size of about 50 nm can be observed. These spots can be ascribed to the presence in some regions of surface blistering. No significant differences have been found within the explored range of fluence. Thermal treatment at 400 °C of graphene paper does not produce significant modifications of the morphology (Figures 3.3.3i, l).

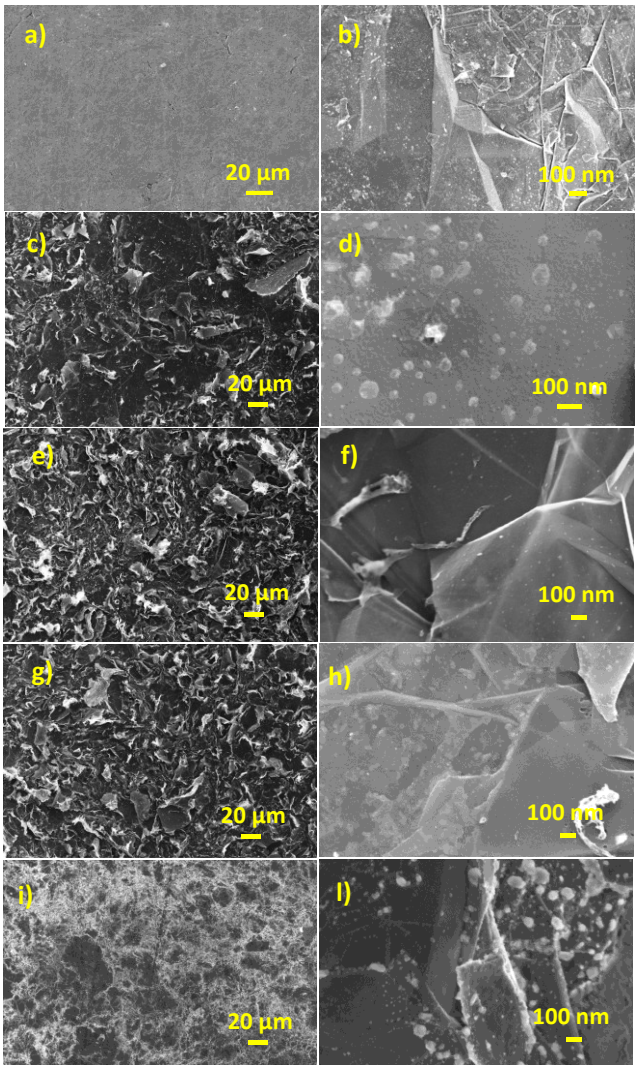

Figure 3.3.3 Scanning Electron Microscopy images of graphene paper (a, b) pristine; laser irradiated at fluence of (c, d) 0.25 Jcm^{-2}; (e, f) 0.5 Jcm^{-2}; (g, h) 1.5 Jcm^{-2}; (i, l) thermal treated at 400 °C, 1 h in N_2.

3.3.3 Electrochemical characterization of graphene paper modified by laser irradiation

Carbon-based materials, conversely to other substrates, reduce the interference in the detection of the analyte in electro-analysis. In particular, graphene-based materials offer high electrical conductivity and large electrochemical working potential [113]. The exfoliation of graphene paper induced by laser irradiation and the subsequent formation of nanosheets increase the real area of the nanoelectrode. The electrochemical characterization of laser modified graphene paper was carried out by cyclic voltammetry, using ferricyanide complex as probing molecule. The electro-active surface area $A_{R\text{-}S}$, the heterogeneous rate constant k^0 and the capacitance C of electrode-solution interface were determined by cyclic voltammetric curves. Figure 3.3.4 reports typical cyclic voltammograms of pristine graphene paper (untreated) and after laser irradiation at 0.25, 0.5, and 1.5 Jcm^{-2}. Voltammograms are characterized by the presence of ferrocyanide anodic and cathodic peaks, whose position is

influenced by the laser surface treatment. The two peaks are superimposed to significant capacitive current. The high electrode-solution capacitance is likely produced by potassium ions intercalation in between graphene planes. The intercalation is favored by the applied potential and proceeds via adsorption of potassium ions on the graphene paper surface and absorption of potassium ions below the top graphene layer, then further exposure to potassium ions leads the intercalate structure [114]. Voltammograms curves shown in Figure 3.3.4 were employed for the quantitative analysis of $A_{R\text{-}S}$, k^o, and C. The active electrode area was determined using the Randles-Sevčik equation valid in quasi-reversible electron transfer processes [115]:

$I_{peak} = 2.686 \times 10^5 \times \sqrt[2]{n^3}\, A_{R-S}\, c_{bulk}\, \sqrt[2]{Dv}$ (See Paragraph 1.1)

where n represents the number of electrons participating in the redox process (n = 1 for ferricyanide), D is the diffusion coefficient (7.6×10^{-6} cm^2s^{-1}) [116], c_{bulk} (1 mM) is the concentration of the probe molecule, ν is the scan rate (0.02

Vs^{-1}) and I_p is the anodic peak current. According to the experimental condition adopted by us, the working area was calculated using the following Equation (3.3.1):

$$A_{R-S}\,[cm^2] = \frac{I_p\,[A]}{1.0475 \times 10^{-4}} \qquad \text{(eq.3.3.1)}$$

The heterogeneous rate constant, k^0, was estimated using the Nicholson model [117]:

$$k^0 = \Psi \sqrt{\frac{\pi n F \nu D ox}{RT}} \left(\frac{Dox}{Dred}\right)^{-\left(\frac{nF\nu}{2RT}\right)} \qquad \text{(eq. 3.3.2)}$$

In Equation (3.3.2), the heterogeneous rate constant k^0 is related to (Ψ), which is a kinetic parameter depending on the anodic-cathodic peak separation ΔEp (Ea-Ec), according to the working curves [117]. Dox is the diffusion coefficient of the potassium ferricyanide, Dred is the diffusion coefficient of the potassium ferrocyanide $Fe(CN)_6^{4-}$ (6.3×10^{-6} cm^2s^{-1}) [116], $\alpha = \frac{nF\nu}{RT} = 0.78$ is the transfer coefficient, while R, T, n, F represent the universal gas constant, the absolute temperature, the number of electrons involved in the redox reaction, and the Faraday constant, respectively. Basing on the

experimental conditions here adopted, the heterogeneous rate constant k^0 was calculated according to the following Equation (3.3.3):

$$k^0 = \Psi \times 4 \times 10^{-3} \qquad \text{(eq. 3.3.3)}$$

Table 3.3.1 reports the data of the various parameters obtained for the graphene paper based nanoelectrodes. The real electro-active area, A_{real}, which is described also as the 'roughness factor', provides information on active surface area and on the presence of inactive regions over the electrode area, was calculated by the following Equation (3.3.4):

$$A_{real} = \frac{A_{R-S}}{A_{geo}} \qquad \text{(eq. 3.3.4)}$$

where A_{geo} is the geometric area of the electrode. The graphene paper reference shows a high real area, which is much greater with respect to that of screen printed carbon paste electrodes, typical of about 0.6 [118]. The laser irradiated samples show an increase of the real area, which achieves a maximum in the case of a fluence of 0.5 Jcm^{-2}. This result is in agreement with SEM analyses that revealed the

presence of numerous flakes on the surface, as consequence of graphene paper exfoliation. Moreover, the trend observed for the real area in laser irradiated samples maybe due to balancing effects of air trapped at interface (that decreases) and of graphene edges (that increase) the number of sites for the electron transfer of the reaction: $Fe(CN)_6^{3-} + 1\ e^- \rightleftarrows Fe(CN)_6^{4-}$

The peak separation, which is related to the reversibility of the electrochemical process, is low for untreated graphene paper and increases with the fluence. According, the heterogeneous rate constant k^o decreases for irradiated samples with respect to the untreated, indicating a rising of the irreversibility of the process. This finding could be attributed to the partial oxidation of the laser irradiated surfaces. Another interpretation may be based on the presence of very thin air layer trapped at the electrode-solution interface, which is formed for the presence of graphene flakes structures. Moreover, the air trapped at electrode-solution

interface maybe the consequence of reduced wettability of highly wrinkled surface.

The capacitance of electrode-solution interface has been calculated using the following equation:

$$C = \frac{\int_{E_1}^{E_2} i(E)dE}{2\nu(E_2 - E_1)} \qquad \text{(eq. 3.3.5)}$$

where ν is the scan rate dV/dt, $i(E)$ is the instantaneous current, $\int_{E_1}^{E_2} i(E)dE$ is the absolute area obtained by integration of positive and negative portion of voltammogramm, except the faradic peak portions. ($E_2 - E_1$) is the potential width. The capacitance of the electrode-solution interface, which provides an indication on the electrode-solution interface extension, increases in laser irradiated samples. However, slight diminution with fluence on going from 0.25 to 1.5 Jcm^{-2} has been observed. The latter experimental finding does not have a straightforward explanation nevertheless air trapping at the highly wrinkled electrode-solution interface could influence the capacitance. The parameters reported in Table 3.3.1 and the size

distribution of gold nanoparticles (see next Paragraph), were used for the selection of the optimal laser fluence in the realization of the GP-AuNPs sensors and for further investigations.

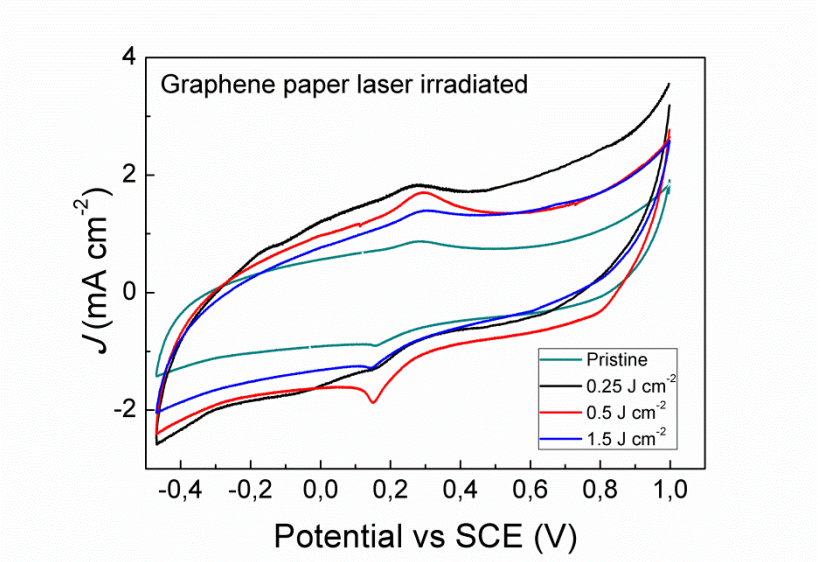

Figure 3.3.4 Cyclic voltammograms of graphene paper as received and after laser irradiation recorded at 0.02 Vs^{-1}, obtained using $Fe(CN)_6^{3-}/FeCN)_6^{4-}$ 1 mM in KCl 1 M as supporting electrolyte.

Table 3.3.1 Electrochemical parameters of laser irradiated graphene paper obtained by cyclic voltammetry.

Sample	Working Area[1] $A_{R\text{-}S}$ (cm^2)	$A_{real} = A_{R\text{-}S}/A_{Geom}$	$\Delta Ep = Ea\text{-}Ec$ (mV)	$k^o(\times 10^{-3})$ (cms^{-1})	C ($mFcm^{-2}$)
Pristine	0.764	1.70	84.4	4	35.3
0.25 Jcm^{-2}	0.477	1.91	101	2	69.1
0.5 Jcm^{-2}	0.954	3.82	128.8	1.2	60.7
1.5 Jcm^{-2}	0.582	2.32	134	1.1	53.3

[1] calculated by the Randles-Sevčik equation using anodic peak current.

3.3.4 Characterization of GP-AuNPs nanoelectrodes

The surface morphology of pristine graphene paper analyzed by SEM is characterized by packed flat layers presenting different orientations (Figures 3.3.3a, b). To facilitate visualization and comparison with metalized samples, Figures 3.3.5a, b reports once again the SEM pictures of pristine graphene paper at comparable magnifications. Figures 3.3.5c, d report representative SEM pictures, acquired at two magnifications, of the gold layer as deposited onto graphene paper. The gold layer is conformal to the surface morphology of the graphene paper. Moreover, a fine structure with the presence of holes can be observed.

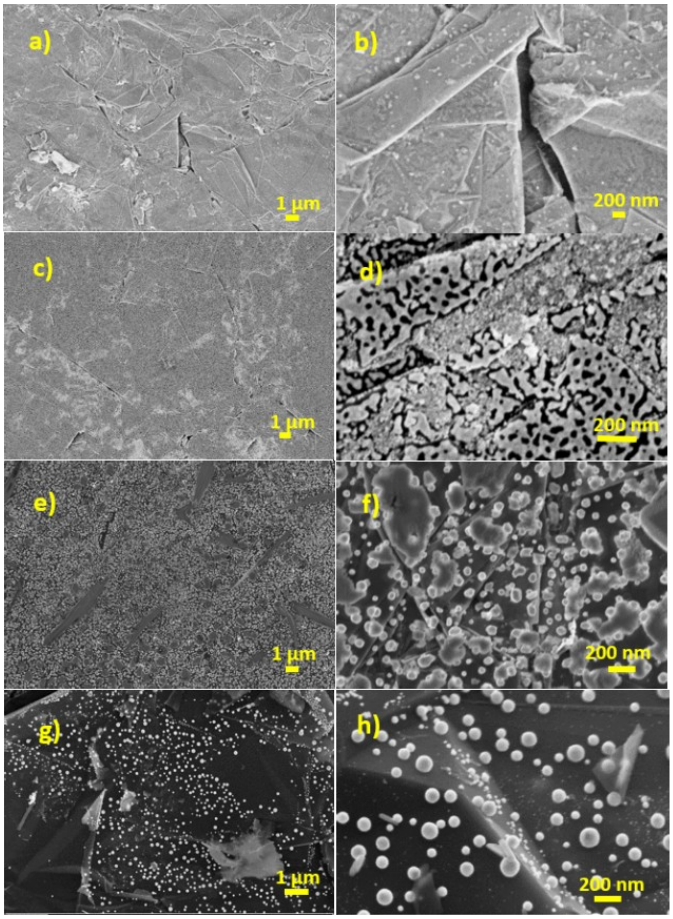

Figure 3.3.5 Scanning Electron Microscopy images of: a)-b) graphene paper pristine; c)-d) Au layer as deposited onto graphene paper; e)-f) thermal dewetted at 500 °C; g)-h) laser dewetted at fluence of 0.5 Jcm^{-2}.

The gold morphology reflects the nucleation and growth mechanisms of thin films at room temperature [119]. Figures 3.3.5e and 3.3.5f report representative SEM pictures of graphene paper-gold nanostructures obtained by thermal

dewetting at 500 °C. The surface shows the presence of typical gold faceted nanostructures. The structures have wide distribution, where the typical size is around 200-400 nm. Moreover, the presence of very small AuNPs with typical size less than 100 nm can be observed. The dewetting conditions at 300 and 400 °C gave similar gold nanostructures (data not shown). Figures 3.3.5g and 3.3.5h report representative SEM pictures of the gold layer after the laser dewetting at fluence of 0.5 Jcm^{-2}. Laser dewetted surfaces are characterized by the presence of gold rich regions consisting of platelets covered with spherical AuNPs. Typical size of AuNPs, which distribution depends on the laser fluence, is in the ranges of 10-150 nm.

The dewetting process is driven by the total surface free energy minimization of the system. Gold thin films deposited on non-metal substrates are, typically, thermodynamically unstable at elevated temperatures, and dewetting, well below the melting temperature (1337.33 K) [120] will occurs upon heating. The entire transformation occurs in the solid state.

This is the case of performed furnace dewetting. Calculation based on the bond-orientational order parameters show that the shape of an assembled gold structure is found to change from spherical to hexagonal, with a marked propensity towards an icosahedral structure [121]. Conversely, laser dewetting induces an increase of temperature that depends on pulse power and duration, heat loss and substrate thermal diffusivity. Typical temperature increase is around 2000 K [105]. Then, laser dewetting occurs at temperature above the gold melting point and the obtained nanoparticles are almost spherical. Moreover, laser pulse produces the curling of the graphene paper and nanoplatelets, which increases the real area of the sensor. Briefly, the main differences exhibited by the solid state (furnace) and liquid state (laser) dewetting process lies in the size distribution and shape of the resulting nanoparticles. Thorough discussion of the involved phenomena in the dewetting was reported by Ruffino [105].

The gold content on the nanoelectrode surfaces was measured by RBS. Figure 3.3.6 reports the spectra of pristine

graphene paper and of gold nanostructures obtained by thermal (500 °C) and laser (0.5 Jcm^{-2}) dewetting. The spectra show the signals assigned to C, O, Na and Au, which in the configuration used in this work, are located at 170, 245, 340 and 660 channels, respectively. Oxygen and sodium can be ascribed to the residues of the preparation process of graphene paper. The spectra were best fitted (simulation not reported) with SIMNRA software assuming an Au volumetric density of 5.9×10^{22} $at.cm^{-3}$. In the spectrum of laser dewetted electrode the gold profile shows a tail at the lower side of channel scale, which is attributed to the gold diffusion into the graphene paper.

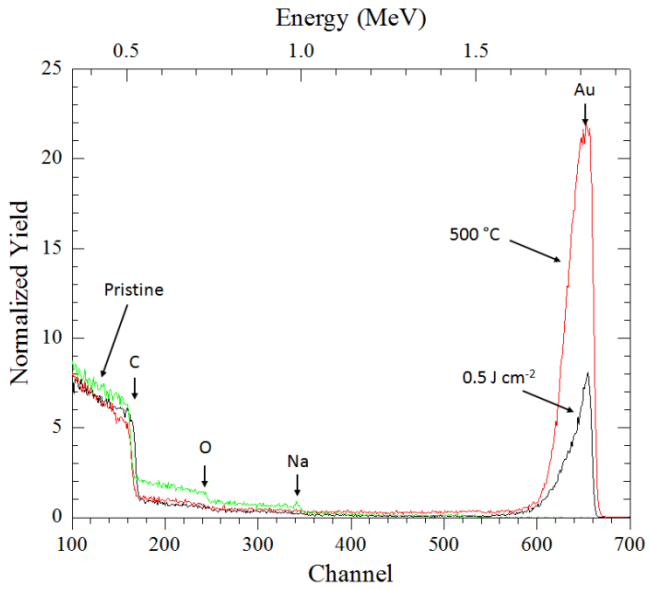

Figure 3.3.6 Rutherford Backscattering spectra of pristine graphene paper and of gold nanostructures obtained by thermal (500 °C) and laser (0.5 Jcm^{-2}) dewetting.

Table 3.3.2 Determination of gold content on the electrode surfaces at various numbers of voltammetry cycles between -0.5 / +1 V in presence of glucose at pH 12.

Sample	Whole number of cycles	Q_{Au} (cm^{-2}) $\times 10^{16}$
As deposited	0	4.69
300 °C	52	3.25
400 °C	10	4.28
	25	3.54
500 °C	10	4.69
	25	3.74
0.25 Jcm^{-2}	10	1.45
	15	1.47
0.5 Jcm^{-2}	52	1.17
1.5 Jcm^{-2}	10	0.38

Table 3.3.2 reports the gold content measured on the electrode surfaces prepared by different dewetting conditions and after ageing. In thermal dewetted electrodes the gold content is partially reduced as increasing the number of cycles, as consequence of partial dissolution and/or debonding from the substrate. However, the electrode shows a high stability

even after 50 cycles. The laser dewetted electrodes show less gold content by increasing the fluence, which is related to a partial ablation during laser irradiation. Moreover, they exhibit a high stability towards the electrochemical measurements, compared to the thermal dewetted electrodes.

3.3.5 XPS characterization of GP-Au Nanostructures

XPS analyses were performed on pristine graphene paper (GP) and on gold metalized electrodes. The survey spectra (not reported) show the signals of carbon, oxygen and gold. Figure 3.3.7a reports the C1s core-shell spectra of pristine GP and of GP-Au as deposited and after 400 °C thermal and 0.5 Jcm^{-2} laser dewetting. The main line is centered at 284.5–284.7 eV [122] and is characterized by high asymmetry, largely because the material is good electric conductor. Additional contribution to the asymmetry originates from the presence of C1s component at about 286.6 and 288 eV (deconvolution not shown) that are assigned to C–O and C=O functional groups, respectively. The features of the main line are in agreement with sp^2 hybridized carbon atoms, associated to π type valence electrons free-like present in the GP. On the high binding energy side of the C1s spectra, π type shake-up satellites are present.

Figure 3.3.7b reports the enlarged spectral regions of these satellite structures normalized to the intensity of the C1s main peak, after linear background subtraction. In the spectra of pristine GP and as deposited GP-Au the satellite features are observed at about 5 eV from the core-shell peaks, which are assigned to the $\pi^* \leftarrow \pi$ transition. Similar shake-up structure was found at 4.4 eV in the case of HOPG [123]. In the thermal and laser dewetted electrodes, the main satellites are found at 6 and 6.4 eV respectively, from the core-shell peaks. These satellites are assigned the dipole like $\pi^* \leftarrow \pi$ shake-up transition ($\Delta L = 1$). The significant intensity and the binding energy shift of the shake-up features observed in the spectra of dewetted samples can be attributed, at least in part, to the interaction of π valence electrons with plasmon excitations in the nanostructure form of gold. Additional satellite with minor intensity was found at 10 eV from the main peak.

The spectrum of laser dewetted sample shows a less intense shake up feature that can be attributed to a partial loss

of π conjugation of the outermost graphene layers. Figure 3.2.7c reports the corresponding Au 4f core-shell spectra. The Au $4f_{7/2}$ peak is centered at 84 eV in the case of as deposited and thermal dewetted samples, which is assigned to gold in the metallic state Au(0), whereas the spectrum of laser dewetted sample shows the peak centered at 84.2–84.3 eV that can be assigned to Au(I), likely in the form of Au-O, as consequence of partial gold nanoparticles oxidation [124].

Figure 3.3.7d reports the corresponding O 1s core-shell spectra. The spectra were deconvoluted using Gaussian components centered at 531.6–531.8 and 533 eV (Gaussians 1–2) that are assigned to C=O and C–O groups, respectively. Moreover, the spectrum of thermal dewetted electrode shows two additional components centered at about 534.6 and 536.3 eV, respectively (Gaussians 3–4), which can be assigned to adsorbed water and adsorbed oxygen [125]. The component in the O 1s spectrum of laser dewetted electrode that would be assigned to Au-O, which is expected weak and centered at 529.4 eV [126], maybe masked by the tail of the components at

531.8 eV. For these reasons, it was not distinguished in the spectrum. It has been proven that gold in the form of nanoparticles can be easily oxidized still maintain the high catalytic activity toward oxidation of organic molecules [126]. Table 3.3.3 reports typical quantitative surface compositions of the as deposited GP-Au and thermal and laser dewetted electrodes measured by XPS. The amount of gold detected on the surface of dewetted electrodes is lower than that deposited, according to the minor exposes surface area by the former, to minimize the surface energy.

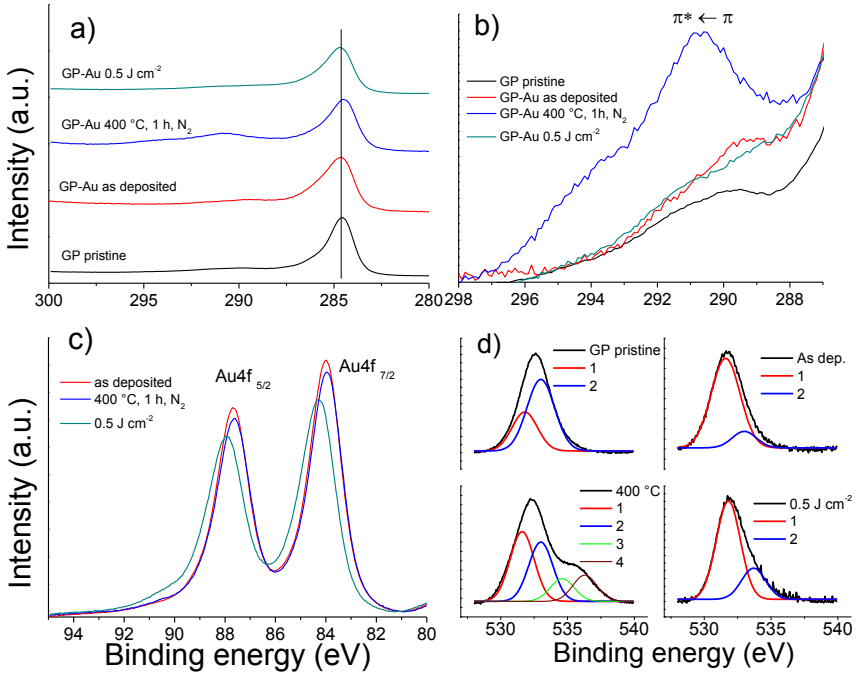

Figure 3.3.7 (a) C1s X-ray Photoelectron core-shell spectra of pristine GP and GP-Au as deposited and after 400 °C thermal dewetting and 0.5 Jcm^{-2} laser dewetting. The vertical line has the function to facilitate visualization. (b) Enlarged spectral regions showing the satellite structure normalized to the C1s core-shell peak, after linear background subtraction; (c) corresponding Au4f spectra; (d) corresponding O1s spectra.

Table 3.3.3 Elemental composition of gold metalized nanoelectrodes (Atomic concentration %).

Sample	Au	C	O
As deposited	12.3	77.4	10.3
400 °C, 1 h, N_2	5.3	67.3	27.4
0.5 Jcm^{-2}	3.9	86.5	9.6

3.3.6 Glucose and fructose electrochemical sensing

Figure 3.3.8a reports the voltammograms of glucose 30 mM in phosphate buffer solution at pH 12, registered by thermal dewetted at 300, 400 and 500 °C GP-AuNPs nanoelectrodes, respectively. For comparison, the voltammogram obtained by the 300 °C dewetted electrode in absence of glucose was reported (blank). In the voltammogram of blank one substantial weak broad peak in the forward scan is observed at -0.1 V, corresponding to the adsorption of OH^- ions on the surface and gold oxidation. Furthermore, no separate peak was observed for gold oxidation, maybe it is broad and overlapped on the background capacitive current. In the backward scan, the gold oxide becomes reduced (broad peak around 0.1 V) and the gold hydroxide layer ($AuOH_{ads}$) is desorbed (-0.25 V). The peaks assigned to the OH^- adsorption and desorption were observed by Pasta at higher potential in presence of chlorine or fluorine ions and using flat gold electrode [127]. The

voltammograms of glucose shows two peaks at 0.25 V and 0.45 V in the forward scan.

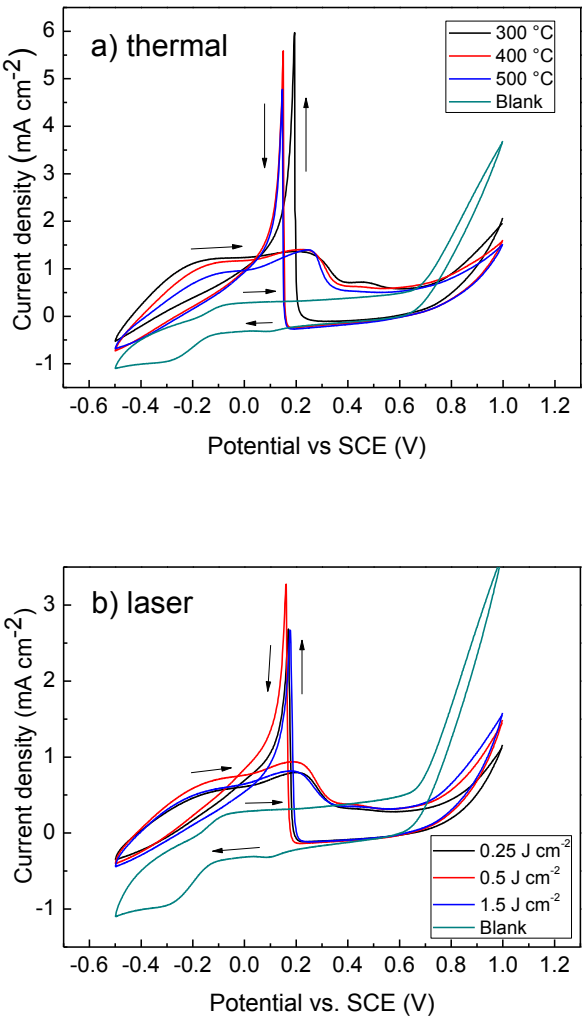

Figure 3.3.8 Voltammograms of glucose 30 mM in phosphate buffer solution at pH 12 detected by GP-AuNPs electrodes: a) thermal dewetted at 300 °C; b) laser dewetted at 0.5 Jcm^{-2}.

The peak at 0.25 V is assigned to gold hydroxide forming on the electrode surface and the adsorbed glucose intermediate is oxidized to gluconolactone. Proceeding further to more positive potentials, the peak at 0.45 V is assigned to the oxidation of the gold hydroxide layer that became oxidized to gold oxide, and the glucose oxidation is inhibited. In the backward scan, the gold oxide was reduced back to gold hydroxide. The peak attributed to the second oxidation of glucose (located at 0.19 V for the 300 °C and at 0.15 V for the 400 and 500 °C) is observed. This very intense and sharp peak is assigned to two-electron process resulting in substantially higher current than in the case of two single electron oxidative reactions observed in the forward scan [68].

Figure 3.3.8b reports the voltammograms of glucose 30 mM in phosphate buffer solution at pH 12 obtained by laser dewetted GP-AuNPs electrodes at 0.25, 0.5 and 1.5 Jcm^{-2} of fluence, respectively. The voltammogram in absence of glucose (blank) was obtained by the 0.5 Jcm^{-2} electrodes and is similar to that observed by the thermal dewetted electrode.

In the forward scan of glucose voltammogram two peaks are observed. The first, centered at 0.19 V is assigned to gold hydroxide forming on the electrode surface and the adsorbed glucose intermediate is oxidized to gluconolactone. The peak is slightly shifted towards lower potential with respect to that observed at 0.25 V for thermal dewetted electrodes, which would indicate slightly better electro-catalytic activity of laser dewetted electrodes. The second peak at 0.45 V, proceeding further to more positive potentials, is assigned to the oxidation of the gold hydroxide layer. In the backward scan, the peak corresponding to the second oxidation of glucose is located around 0.17 V.

I hypothesize that the significant intensity and sharpness of peak corresponding to the second glucose oxidation can be ascribed to the combination of the electro-catalytic properties of gold nanostructures with the electronic properties of high structural order graphene paper. It has been demonstrated that the electronic structure, charge neutrality point and electron-phonon coupling of graphene remain nearly intact

upon gold deposition. The charge carrier density at a graphene-gold contact is not pinned [128]. These properties can favor the electron transfer from the gold nanoparticle towards the graphene paper and, then, the two electron process of glucose oxidation resulted with very high efficiency.

Table 3.3.4 reports the peak current density, corresponding to the two electrons oxidation of glucose 30 mM, measured by different nanoelectrodes. The peak current density depends on the real area of the whole gold nanostructures, which, in turn, depends on the gold content present on the electrode surface. Figure 3.3.9 reports the ratio of the peak current density to the gold content reported in Table 3.3.2. Laser dewetted electrodes show a significant increase of the analytical performance compared to the thermal dewetted electrodes, when referred to the same gold content.

Table 3.3.4 Current density of the anodic peak corresponding to the two electron oxidation of glucose.

Sample	J_{peak} (mA·cm^{-2})
300 °C	6.13 ±0.37
400 °C	5.7±0.19
500 °C	4.9±0.07
0.25 Jcm^{-2}	2.8±0.12
0.5 Jcm^{-2}	3.0±0.23
1.5 Jcm^{-2}	2.7±0.26

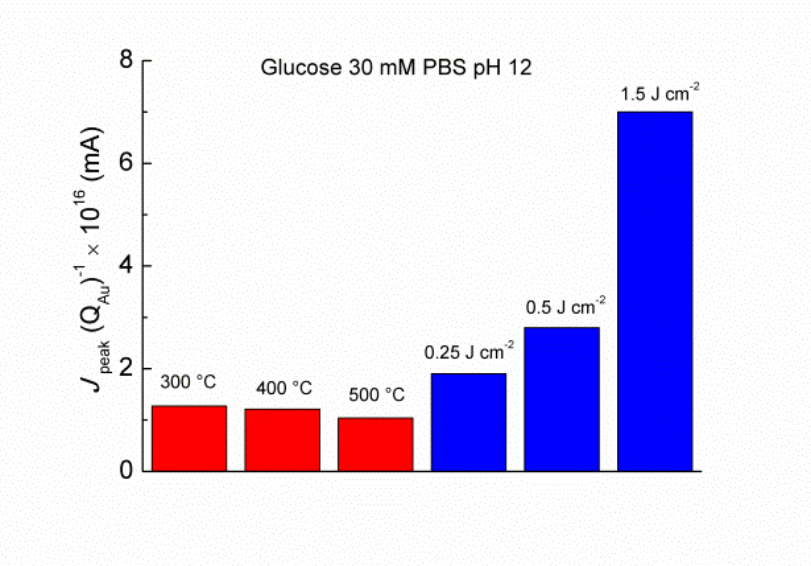

Figure 3.3.9 Ratio of the current density corresponding to the two electron oxidation of glucose to the sensor gold content.

The electro-catalytic activity is significant even at very low gold content as 3.85×10^{15} Au cm^{-2} (electrode dewetted at 1.5 Jcm^{-2}).

The electro-catalytic activity towards the oxidation of fructose was investigated in phosphate buffer solution at pH 12.

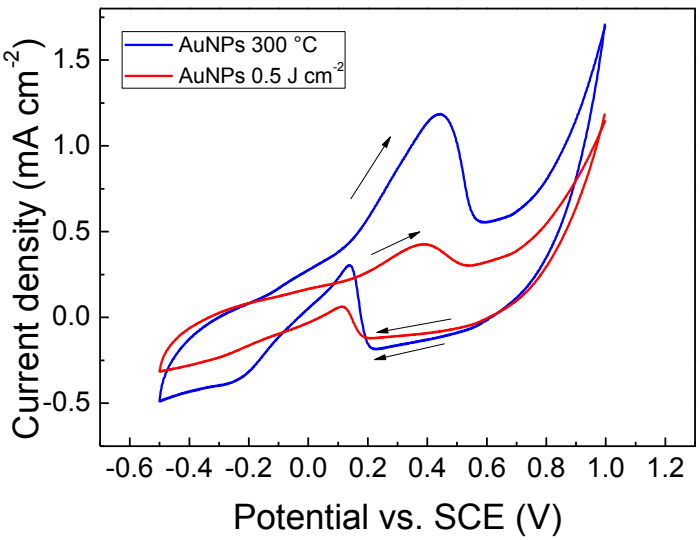

Figure 3.3.10 Voltammograms of fructose 30 mM in phosphate buffer solution at pH 12 detected by GP-AuNPs electrodes thermal dewetted at 300 °C and laser dewetted at 0.5 Jcm^{-2}.

Figure 3.3.10 reports the voltammograms of fructose 30 mM measured by GP-AuNPs electrodes dewetted at 300 °C and at fluence of 0.5 Jcm^{-2}. In forward scan, single well defined oxidative peak located at 0.43 V or 0.38 V was observed for thermal and laser dewetted electrodes,

respectively. The peak can be assigned to the direct anodic oxidation of fructose. In the backward scan peak located at 0.15 V or 0.13 V, respectively, were observed. In alkali solution D-fructose tautomerizes to D-glucose and D-mannose, the peak observed in backward scan can be assigned to the two electron oxidation of glucose and mannose.

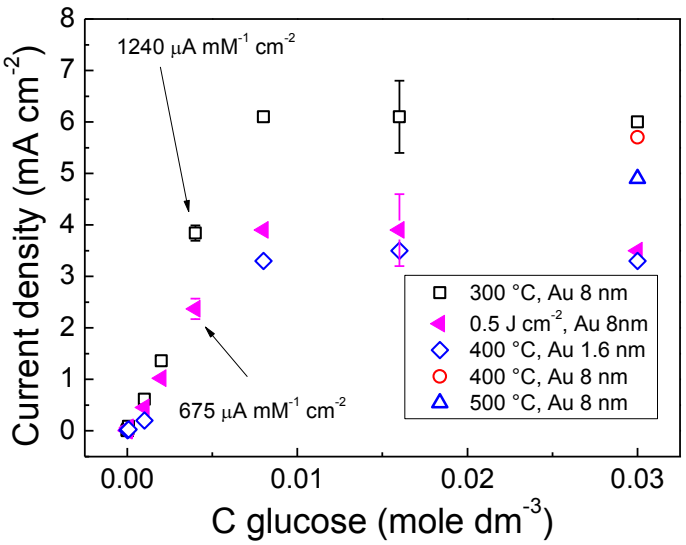

Figure 3.3.11 Current density calibration of glucose detected by GP-AuNPs electrodes obtained by thermal or laser dewetting.

Figure 3.3.11 reports the current calibration curves for glucose obtained at a potential of 0.19 V (thermal electrode) and 0.17 V (laser electrode). The response to glucose was determined in the concentration range of 2.5 μM to 30 mM. There is little influence of dewetting temperature in the range 300–500 °C on the nanoelectrode response. In this temperature range there is no significant variation of gold content (see Paragraph 3.6). Moreover, Figure 3.3.11 reports the response of the sensor obtained by dewetting at 400 °C a gold layer 1.6 nm thin. The thickness of 1.6 nm was chosen to have a final average gold quantity comparable to that of the 0.5 Jcm^{-2} laser dewetted sensor (see Paragraph 3.3.4). The response to glucose of the 400 °C 1.6 nm gold sensors was found similar to that of the 0.5 Jcm^{-2} laser dewetted sensor obtained by gold layer 8 nm thick. Based on this finding, the amount of gold present in the form of nanostructures on the sensor surface determines the nanoelectrode response. In fact, gold is not just a catalyst, but participate in the oxidation reaction of glucose. The response of the nanoelectrodes

reflects the gold concentrations at surface reported in Table 3.3.3. According, the apparent lower response of the laser dewetted electrode can be attributed to the lower gold content. The presence of Au(I) in the laser dewetted electrodes seems to influence the peak position of the two-electron oxidation, but not the sensor current response.

The errors bars, calculated as the relative standard deviation on five measurements, are reported only for the concentrations of 4 and 16 mM to facilitate visualization. The highest error was within the 10 % of the mean value. In the concentration range from 20 μM to 8 mM a quasi-linear current response was obtained by both types of nanoelectrodes. Not linear response was observed in the range of concentration 8-30 mM, where the diffusion controlled mechanism limits the sensitivity of the nanoelectrodes. Highest sensitivities of 1240 $\mu A \cdot mM^{-1} \cdot cm^{-2}$ and of 675 $\mu A \cdot mM^{-1} \cdot cm^{-2}$, were obtained in the concentration range of 2-4 mM by thermal and laser dewetted electrodes, respectively. Table 3.3.5 reports the analytical performance of the

nanoelectrodes. The limit of detection (LOD) and the limit of quantification (LOQ) have been calculated by using a current value corresponding to 3 or 10 times of the background current I_{rms} = 1.77 μA, measured without glucose analyte, respectively (3×S/N or 10×S/N method). The equations of least square regression line with the coefficient of determination R^2 were also reported. For comparison, the Table reports recent literature results concerning carbon-AuNPs and enzymatic based glucose biosensors. The results of sensitivity, detection limit and linear range present good values compared to recent studies related to the detection of glucose on gold nanostructured based materials [68, 129-131].

Table 3.3.5 Comparison of the analytical performance of Au nanoporous and carbon-AuNPs to enzymatic based glucose biosensors.

Material	Detection limit (μM)	Sensitivity ($\mu A \cdot mM^{-1} \cdot cm^{-2}$)	Linear range	Ref.
Gelatin-templated gold nanostructures	90	1165	32 μM-10 mM	[68]
Glucose oxidase (GOx)/carbon quantum dots (CQDs)-gold nanoparticles (AuNPs)	13.6	626.06	0.16-4.32 mM	[129]
Carbon nanotubes/AuNPs	4.1	2.77	4.1 μM-25 mM	[130]
CQDs/AuNPs	17	47.24	50 μM-2.85 mM	[131]
Graphene paper/AuNPS dewetted 300 °C	2.5	1240	15 μM-8 mM $\Delta J = 4.97\times10^{-6} + 0.664$ C R^2 0,997	This work
Graphene paper/AuNPs laser dewetted 0.5 Jcm^{-2}	2.5	675	20 μM-8 mM $\Delta J = 4.67\times10^{-6} + 0.497$C R^2 0.996	This work

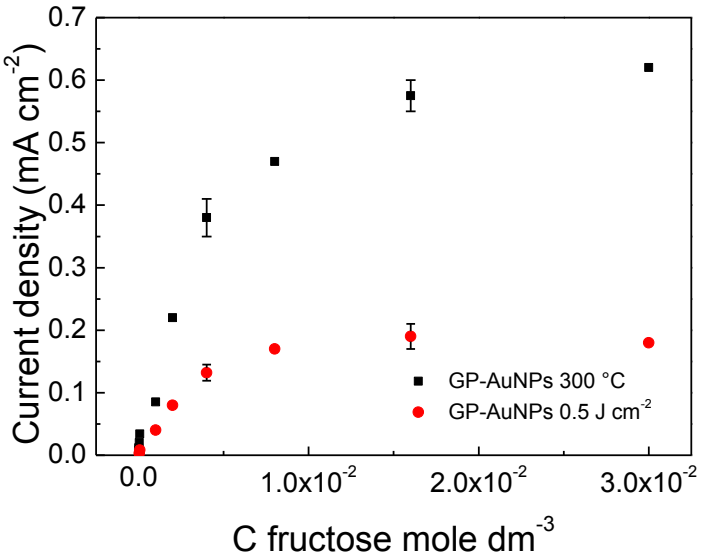

Figure 3.3.12 Current density calibration curves of fructose at 0.4 V vs. SCE obtained by GP-AuNPs electrodes thermal dewetted at 300 °C (black square) and laser dewetted at 0.5 Jcm^{-2} (red circle).

Figure 3.3.12 reports the current calibration curves of fructose detection obtained at a potential of 0.4 V by both thermal and laser dewetted electrodes. Table 3.3.6 summarizes the analytical performance. The thermal dewetted electrode shows a linear response in the range 5µM-4 mM, a detection limit of 2.5 µM and a sensitivity of 394 $\mu A \cdot mM^{-1} \cdot cm^{-2}$. Whereas, the laser dewetted electrode shows

linear response in the range 40 μM-4 mM, a detection limit of 20 μM and a sensitivity of 32 $\mu A \cdot mM^{-1} \cdot cm^{-2}$. Table 3.3.6 reports, for comparison, recent literature data for the electrochemical detection of fructose [132-135]. It is worthy of note that in the cited references the electro-active materials are of enzymatic/non-enzymatic hybrid type.

Table 3.3.6 Comparison of the analytical performance of GP-AuNPs sensor to fructose biosensors reported in the literature.

Material	LOD (μM)	Sensitivity ($\mu A \cdot mM^{-1} \cdot cm^{-2}$)	Linear range	Ref.
2-carboxy-6-naphtoyl diazonium-fructose dehydrogenase (ND-FDH) modified AuNPs	1.2	3.7	50 μM-0.3 mM	[132]
SAM of MPS + FDH/TTF on Au (*)	2.5	29.1	10 μM-1mM	[133]
Os-polymer modified FDH on screen printed graphene	0.8	2.15	0.1-8 mM	[134]
FDH immobilized on ferrocyanide/ SPCE (§)	50	1.2	0.1-1 mM	[135]
Graphene paper/AuNPS dewetted at 300 °C	2.5	394	5 μM -4 mM $\Delta J = 3.24 \times 10^{-6} + 0.394$ C R^2 0.989	This work
Graphene paper/AuNPs laser dewetted 0.5 Jcm^{-2}	≥20	32	40 μM-4 mM $\Delta J = 6.19 \times 10^{-6} + 0.032$ C R^2 0.986	This work

(*) self-assembled monolayer (SAM) of 3-mercaptopropionic acid (MPA) on which fructose dehydrogenase (FDH) and the mediator tetrathiafulvalene (TTF) are co-immobilized by cross-linking with glutaraldehyde on dealloyed Ag-Au alloy. (§) Screen printed carbon electrode.

3.3.7 Interference study

The response to interferences was examined at concentration of glucose and fructose 8 mM in presence of ascorbic acid (AA) at 0.25 mM and uric acid (UA) at 0.1 mM in buffered pH 12 solutions. The employed concentrations of interferents are comparable to that present in human serum of adult. Table 3.3.7 reports the current density variation (mean value) for the detection of glucose and fructose in presence of AA and AA+UA. There is significant interference in the sensing of glucose and fructose, with a reduction in the current density on addition of AA and UA. The most significant effect was observed with UA. The glucose and fructose responses are almost entirely restored by electrode washing in water. The observed interference effect, according to Branagan [130], is attributed to electrode surface fouling produced by surface adsorption of UA. Oxidation potential of UA on gold-nafion modified screen printed carbon electrodes was found at 0.5-0.6 V [136], which is far from the potential used by us in the detection of glucose and fructose. In fact,

very low operating potential offered by GP-AuNPs sensors is beneficial regarding a lower effect of direct electrochemical interferences in real sample matrixes [68, 130-132]. The results indicate high electrochemical selectivity of the proposed sensors toward the detection of glucose and fructose in comparison to the normally co-existing electro-active interfering species.

Table 3.3.7 Current density ($mAcm^{-2}$) measured at potential of: 0.19 V (electrode dewetted at 300 °C) and 0.17 V (electrode laser dewetted at 0.5 Jcm^{-2}) for the detection of glucose 8 mM; 0.4 V for the detection of fructose 8 mM in presence of AA 0.25 mM and UA 0.1 mM. The error is represented by the standard deviation calculated on five measurements.

	GP-AuNPs 300 °C	% of variation	GP-AuNPs 0.5 Jcm^{-2}	% of variation
Glucose	6.1±0.07		3.9±0.10	
Glucose + AA	5.3±0.05	-13	4.2±0.06	+7
Glucose+AA+UA	3.3±0.12	-46	2.5±0.11	-35
Fructose	0.47±0.02		0.22±0.02	
Fructose + AA	0.46±0.05	-2	0.20±0.05	-9
Fructose+AA+UA	0.47±0.1	0	0.18±0.05	-18

3.3.8 Electrode stability

The stability of laser dewetted in comparison to the thermal dewetted electrodes was studied at pH 12 employing glucose solutions at different concentrations. Figure 3.3.13 shows the most significant modification of nanoelectrode response observed by glucose solution 30 mM. In the Figure the 1st and the 50th cycles of voltammograms registered by GP-AuNPs sensors dewetted at 400 °C and at fluence of 0.25 Jcm^{-2} respectively, are compared. The laser dewetted electrode shows almost identical voltammograms, indicating a huge stability under the adopted conditions, whereas the thermal dewetted electrode shows a modification of the shape of the voltammogram. In particular, the two electron oxidation peak is reduced in intensity and sharpness and shifted to lower potential on going from the 1st to the 50th cycle. Simultaneously, an increase of the peak at 0.45 V was observed. These findings can be ascribed to a reduced and/or modified electro-catalytic property of the gold nanostructures. Figures 3.3.14a, 3.3.14b show the SEM pictures of the sensor

obtained by thermal dewetting at 400 °C before and after 50 voltammogram cycles between −0.5 to 1 V, respectively. The morphology of the gold faceted nanostructures is, clearly, heavily modified. Conversely, the laser dewetted sensor at 0.5 Jcm^{-2} of fluence shows almost unmodified morphology after 50 voltammogram cycles between −0.5 to 1 V (Figures 3.3.14c, 3.3.14d). According to XPS data, the high stability of laser dewetted electrode can be attributed to the presence of Au(I) in the AuNPs. The presence of bonds with oxygen blocks the self-diffusion of the gold atoms and preserves the nanostructures. Figure 3.3.15 reports the gold content measured by RBS as function of voltammogram cycles for various nanoelectrodes. In thermal dewetted electrode the gold content decreases with the number of voltammogram cycles. This is related to a partial gold dissolution during the cycles. Conversely, laser dewetted electrodes show an almost unmodified gold content. The gold content in laser dewetted electrodes is related to the fluence, and is reduced by partial laser ablation.

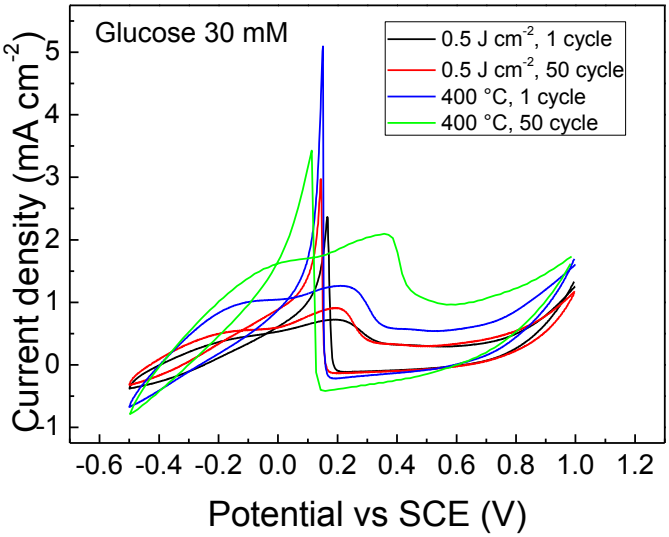

Figure 3.3.13 Cyclic voltammograms of glucose 30 mM detected by GP-AuNPs electrodes thermally and laser dewetted at fluence of 0.25 Jcm^{-2}. Comparison of the 1st and the 50th cycles.

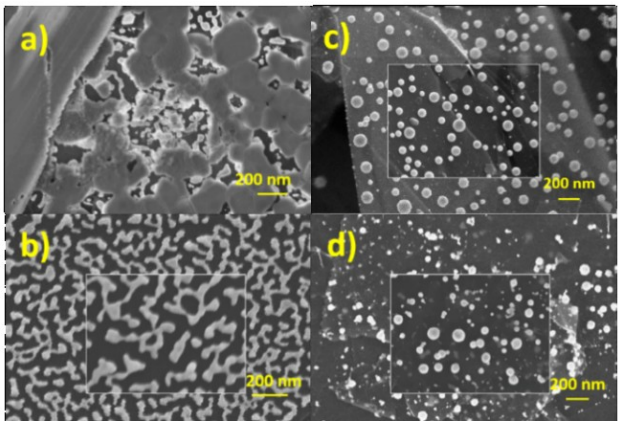

Figure 3.3.14 Scanning Electron Microscopy images of electrodes prepared by thermal dewetting at (a) 400 °C and (b) after 50 voltammogram cycles between −0.5 to 1 V; (c) laser dewetting at 0.5 Jcm^{-2} of fluence and (d) after 50 voltammogram cycles between −0.5 to 1 V.

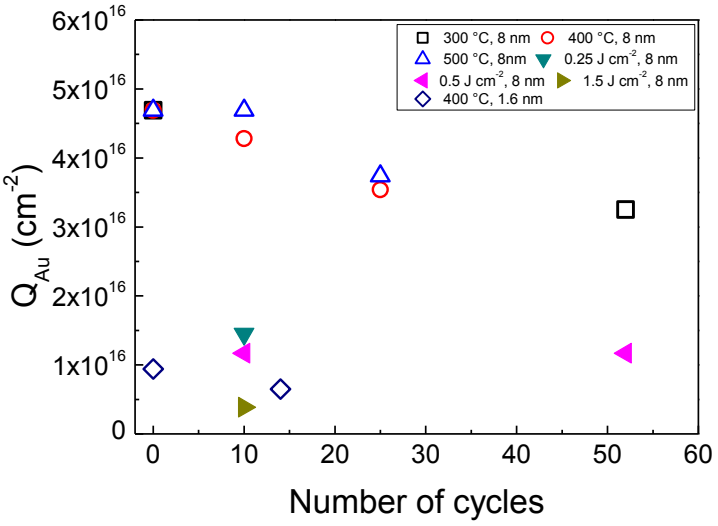

Figure 3.3.15 Gold content measured by Rutherford Backscattering Spectrometry as function of initial thickness and the number of voltammogram cycles (buffer solution at pH 12) for: 8 nm layer thermal dewetted at 300 °C, 400 °C and 500 °C; 1.6 nm layer thermal dewetted at 400 °C; 8 nm layer laser dewetted at 0.25, 0.5 and 1.5 Jcm^{-2} of fluence.

3.4 Conclusions

The work presented here demonstrates the feasibility of stable and disposable electrochemical sensors with nanostructured gold onto graphene paper substrate for sensitive glucose and fructose detection. The nanoelectrodes have been prepared by furnace or laser dewetting of 1.6 and 8 nm thick gold layers onto graphene paper.

One of the main difference exhibited by the solid state (furnace) and liquid state (laser) dewetting lies in the size and shape of the resulting nanostructures. Laser dewetting originates particles with size in the ranges of 10-150 nm. Furnace dewetting originates faceted nanostructures with typical size of 200-400 nm. The particles obtained by laser dewetting are almost spherical, while those obtained by furnace process present a characteristic faceting. Moreover, laser dewetted electrodes show a high electro-catalytic activity even at very low gold content as 3.85×10^{15} Au cm^{-2}.

Both type of nanoelectrode exhibited a high sensitivity for glucose detection up to 1240 $\mu A \cdot mM^{-1} \cdot cm^{-2}$, low detection limit

down to 2.5 μM and wide linear range (15 μM- 8 mM). The nanoelectrodes show good response for the detection of fructose, and good stability (possibility of reusing the test stripes tested up to 50 times even after 6 months).

The electro-catalytic oxidation of glucose on gold surface is highly pH dependent, and is favored in alkali media. This has been interpreted considering the significant role of negatively charged reaction intermediates, such as the crucial step of OH^- adsorption. Graphene based support can act synergistically with gold nanoparticles, enhancing the sensitivity and selectivity of gold alone. This enhancement can be interpreted by the efficient charge transfer from the Au nanostructures to the π delocalized orbitals in the graphene paper. This phenomenon may explain the significant sensitivity of the proposed sensors. The electrode sensitivity is related to the total amount of gold present on the surface, according to the fact that gold is not just a catalyst, but participates to the oxidation reaction of glucose. The exfoliation of graphene paper produced by nanosecond laser

irradiation leads to an increase of the nanoelectrode real area up to about a factor two. This phenomenon increases further the sensor analytical performances. XPS analyses of laser dewetted electrodes evidenced the formation of gold oxide. Oxidized gold nanoparticles are characterized by high morphology stability under the alkali glucose detection test and unmodified electro-catalytic activity.

The proposed fabrication methods are characterized by few simple and fully dry steps, compared to the other methods, which are, however, based on multi-steps solution processes and/or on the use of enzymes. In particular, compared to the methods reported in literature, our fabrication methods are characterized by low cost if compared to the high throughput, simplicity, high purity of the electrode, absence of toxic materials and low generation of dangerous waste during the production. The proposed nanoelectrodes are expected to be biocompatible and highly tolerated by the skin, thanks to the absence of metals such as nickel or copper. Moreover, the absence of wet chemical processes and, then, of

ion contamination, makes more easy the integration of the proposed nanoelectrodes with microelectronic silicon chip for the data acquisition and processing. The resulting analytical performances for the glucose and fructose detection are very promising since comparable or better than the actual state of art for nanostructured gold electrodes.

Chapter 4. Bismuth-nafion nanoelectrode for metal trace analysis

4.1 Trace analysis of heavy metal contamination

Lead and cadmium are two of the most poisonous cumulative metals that affect multiple body systems. The two metals are particularly harmful to young children, because affect cognitive functions and intellectual development [137]. Both metals in the human body are distributed to the blood, brain, liver, kidney and bones. They are stored in the teeth and bones, where accumulate over time. Human exposure is

usually assessed through the determination of the metals in blood [138, 139]. Lead in bone is released into blood during pregnancy and becomes a source of exposure to the developing fetus. There is no known level of lead exposure that is considered safe. Fortunately, lead and cadmium exposure is preventable. Cadmium possesses toxic effects on the kidneys as well as the skeletal and respiratory systems. Moreover, it is carcinogen [138]. Usually, natural concentrations of cadmium and lead in the ground water are less than 0.5 ppb [138, 139]. Human activity has greatly increased levels of both lead and cadmium in environmental media relevant to population exposure [138, 139]. Exposures potential of particular concern for human include, but not limited to mining, disposal and recycling of lead acid car batteries, ethyl-leaded fuels, electronic and electrical waste, Ni-Cd batteries, as well as toys, jewelry and plastics containing cadmium, emissions from municipal solid waste incineration, fossil fuels. Corrosion of zinc plated water containers as well as soldered pipes are additional significant sources of lead and cadmium

contamination. The aforementioned contamination sources have a potentially impact on drinking water as consequence of aquifers contamination. U.S. Environmental Protection Agency (EPA) established in the Drinking Water Requirements for lead and cadmium that actions have to be taken at level of 15 and 5 ppb, respectively [140]. The European Directive on the quality of water intended for human consumption established that action have to be taken at level of 10 and 5 ppb for lead and cadmium, respectively [141]. Among the analytical techniques for the detection of heavy metals at sub-ppb level such as inductively coupled mass spectrometry (ICP-MS) [142] or high performance liquid chromatography (HPLC) [143], square wave anodic stripping voltammetry (SWASV) is one of the most powerful, being characterized by sensitivity below the ppb level [144, 145], combined with low cost of the sensors and light instrumentation, which give the possibility of on-site measurements [146]. SWASV combines an accumulation step of the analyte on the electrode surface, by *in-situ or ex-situ*

method, with a high sensitivity electro-analytical detection technique. About two decades ago, bismuth thin film electrode has been proposed instead of mercury drop electrode for the alloying of heavy metals. Lu compared the sensing performance of four kinds of nanomaterials capable to replace mercury that are based on metallic nanoparticles, metal oxides, carbon nanomaterials and their nanocomposites and chelating additives for analyte metal ions [147]. However, among the various kinds of nanomaterials, bismuth based electrodes are the most promising substitutes in the analysis of lead and cadmium by SWASV for their suitable working potential window and not-poisonous properties [148-152]. Numerous works described the realization of electrodes by electro-deposition of bismuth on substrate consisting of modified glassy carbon [153, 154], graphene oxide [155], modified multiwalled carbon nanotubes [156] and screen printed carbon paste [157, 158]. Carbon based materials used as substrate exhibit some advantages, which include the absence of interfering metal ions, the possibility of a variety of

chemical functionalization, the low cost, the high electrical conductivity and the large amplitude of working potential [159, 160]. To further improve the electrode sensitivity, in the last years, adsorptive electrode or hybrid adsorptive-Bi alloying based electrodes have been described in literature [161]. Three-dimensional graphene-carbon nanotubes hybrid nanomaterials have been described with improved selectivity and detection limit to 0.1 and 0.2 ppb for cadmium and lead respectively [145]. In particular, nafion was reported in literature as capping layer, binding material, in combination with bismuth and glassy carbon electrode [162-164], or forming dispersion of bismuth nanoparticles supported on graphene [165]. The use of nafion alone or in combination with a chelating agent improves further the selectivity and sensitivity towards detection of cadmium and lead with respect to bismuth coated carbon based materials alone. Zhao proposed a multi-walled carbon nanotube-emeraldine base polyaniline-nafion composite modified glassy carbon electrode, obtaining the sensitive detection of trace Pb(II) and

Cd(II), with a detection limit of 0.06 ppb for Cd(II) and 0.08 ppb for Pb(II) [153]. Segura proposed a glassy carbon electrode modified with nafion, 1-nitroso-2-naphthol and bismuth film for adsorptive stripping voltammetry determination of Pb(II) and Cd(II) in tap water. The detection and quantification limits were 0.08 and 0.29 ppb for Pb(II) and 0.07 and 0.24 ppb for Cd(II), with a linear detection range from 10 ppb to 70 ppb [161]. Mau Thanh proposed a glassy carbon electrode modified by *in-situ* co-deposition of bismuth and 8-hydroxyquinoline as chelating agent, obtaining detection limits of Pb(II), Cd(II), and Zn(II) of 0.45, 0.17, and 0.78 ppb, respectively, in the range from 2 ppb to 110 ppb [166]. However, some of the electrodes described in literature present weak points, the most important are related to the complex preparation and the use of many reagents. These facts lead to not reproducible and costly electrodes. Thus, an increasing demand for low-cost, sensitive and easy reading electrodes still exists, despite the several efforts that have been done by the scientific community [156-170].

In this activity I studied a simple procedure for the fabrication of high performances, stable, environmentally friendly, low cost nano electrochemical sensors for high sensitive Pb^{2+} and Cd^{2+} detection in solution. The nanoelectrode consists of graphene paper, nafion and bismuth composite materials. The novelty of the proposed nanoelectrode consists in the combined use of the graphene paper that acts as support, substrate and electrical conductive path, with nafion and bismuth nanostructures. Moreover, a key process step consisting in the H^+ ion exchange with Bi^{3+} in the ionomer has been proposed. The step is aimed to increases the accumulation of bismuth in the nafion film during the electro-deposition.

4.2 Experimental

4.2.1 Fabrication of graphene paper-nafion-Bi nanoelectrode

Sodium hydroxide, acetic acid, graphene paper 240 μm thick (XG Science), nafion (perfluorosulfonic acid ionomer) 5 % wt. solution (Figure 4.2.1), Bi^{3+}, Pb^{2+} and Cd^{2+} respectively, at 1 g dm^{-3} reference standard material (RSM) traceable to National Institute of Standards and Technology (NIST) solutions were purchased from Sigma Aldrich, Milan, Italy.

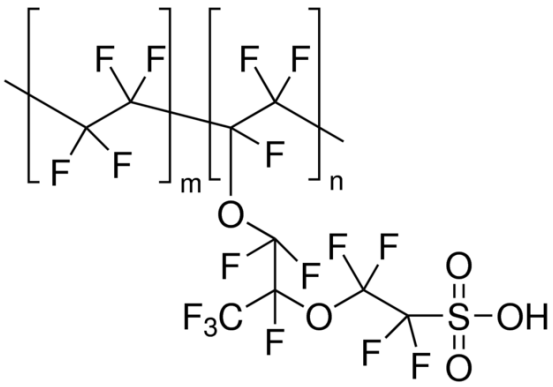

Figure 4.2.1 Chemical structure of nafion (picture available online at: www.sigmaaldrich.com).

All reagents were of trace analysis grade and all aqueous solutions were made by Milli-Q water. Solutions of Bi^{3+}, Pb^{2+} and Cd^{2+} at various concentrations were prepared diluting the stock solutions by 0.1 M acetic buffer solution at pH 4.5.

Strips of graphene paper 1 cm × 3 cm were used with the function of support, electrical conductor and active material of the electrode. About 15 μl of nafion solution was casted onto 1 cm^2 on both side of graphene paper and dried at 70 °C, 10 min in air. The remaining part of strip of graphene paper was isolated from the solution and represents the conductive path of electrode. Casted amount of solution corresponds to a thickness of nafion layer of about 0.5-0.7 μm. Then, a first batch of electrodes was overnight soaked into buffer solution at pH 4.5 with Bi^{3+} 100 mg dm^{-3}, (GP_naf_ex_Bi), according to the procedure reported in Figure 4.2.2 and summarized in Table 4.2.1.

Table 4.2.1 Nanoelectrode structures used in this work.

Electrode name	Nafion layer	Bi electro-deposition
GP_Bi	Not present	yes
GP_naf_Bi	Overnight soaked without ion exchange	yes
GP_naf_ex_Bi	Overnight soaked with Bi^{3+} ion exchange	yes

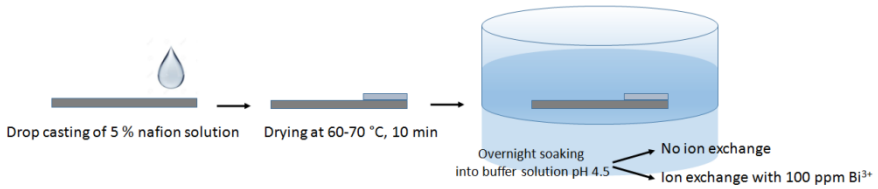

Figure 4.2.2 Scheme of nanoelectrodes preparation.

The latter method was employed to ensure a thorough exchange of the H^+ ions of the sulfonic groups in the ionomer with Bi^{3+}:

$$3\,[R\text{-}SO_3^-\,H^+] + Bi^{3+} \rightleftarrows [3(R\text{-}SO_3^-)\,Bi^{3+}] + 3H^+$$

For comparison, to study the effects of overnight ion exchange a second batch of electrodes was overnight soaked into buffer solution in absence of bismuth ions (GP_naf_Bi). Bi was electrochemically deposited at room temperature

through the nafion layer at – 1V vs. SCE for 600 s in stirred solution at 250 rpm. To study the effect of nafion on the electrode analytical performance, in a third batch of electrodes bismuth was deposited directly onto graphene paper (GP_Bi). Table 4.2.1 summarizes the structure of electrodes employed in this work.

4.2.2 Instrumental characterization

Characterization by Electrochemical Impedance Spectroscopy (EIS) was done in potentiostatic mode at 10 mV RMS (Root Mean Square) employing a 100 ppm Bi^{3+} into 0.1 M acetic buffered solution at pH 4.5. This solution acts both as electrolyte and bismuth deposition bath. Pb^{2+} alone or Pb^{2+} and Cd^{2+} were concentrated on the electrode surface at – 1.2 V vs. SCE for 1200 s in stirred solution at 250 rpm. SWASV was done after a quiet period of 30 s (see Fig. 4.2.3). All the measurements were performed in acetic buffer solution 0.1 M at pH 4.5, which enhances Pb and Cd deposition and stripping response [167]. The electrodes were cleaned for successive measurements applying a potential of -0.4 V vs. SCE for 200 s to strip residual Pb and Cd present on the electrode surface. The analytical parameters were chosen on the basis of the literature data [145, 162], whereas the instrumental parameters of SWASV were optimized experimentally (see Figures 4.2.4a, b). Figure 4.2.3 reports the typical waveform of

potential used in the SWASV. The experimental parameters consist of pulse height (E_{pulse}), step (E_{step}) and frequency. The values used in this work were E_{pulse} 75 mV, E_{step} 2 mV and frequency 2 Hz. In the experiment, the potential is scanned over the range that comprises the peaks corresponding to the analytes. The current is measured twice during each cycle, once at the end of the forward pulse (I_F), and again at the end of the reverse pulse (I_R). The differential value is plotted versus the applied potential.

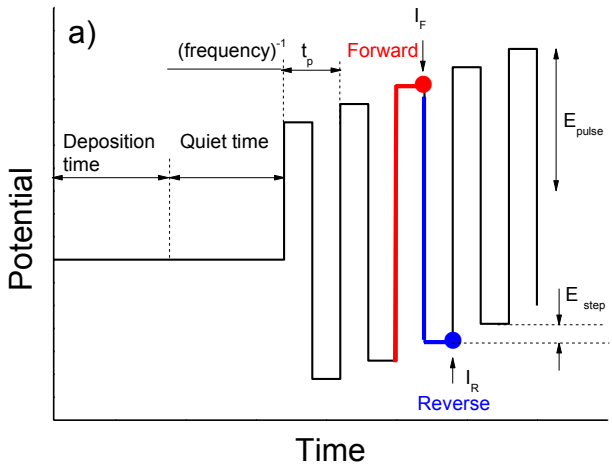

Figure 4.2.3 Typical waveform of potential used in Square Wave Anodic Stripping Voltammetry.

The instrumental parameters of SWASV have been optimized to obtain anodic stripping peak with highest symmetry and lowest full width at half maximum (FWHM). Figures 4.2.4a and 4.2.4b report the effect of pulse height and frequency, respectively, studied by a Pb^{2+} 100 ppm buffered solution at pH 4.5. Pulse height was explored in the range of 25-100 mV at constant step increment of 2 mV and frequency of 10 Hz. The peak current intensity increases significant with the pulse height. The frequency was explored in the range of 2-25 Hz at constant pulse height and step increment of 75 and 2 mV, respectively. The best peak shape was obtained at a frequency of 2 Hz, which corresponds to a pulse period of 0.5 s. The step increment was explored in the range of 5-20 mV. The best combination of parameters was pulse height 75 mV, frequency 2 Hz and step increment of 2 mV, which corresponds to a scan rate of 4 mV s^{-1}. A FWHM of about 100 mV was obtained for the peak of lead. The selected parameters values are closest to that used by other authors [145, 162].

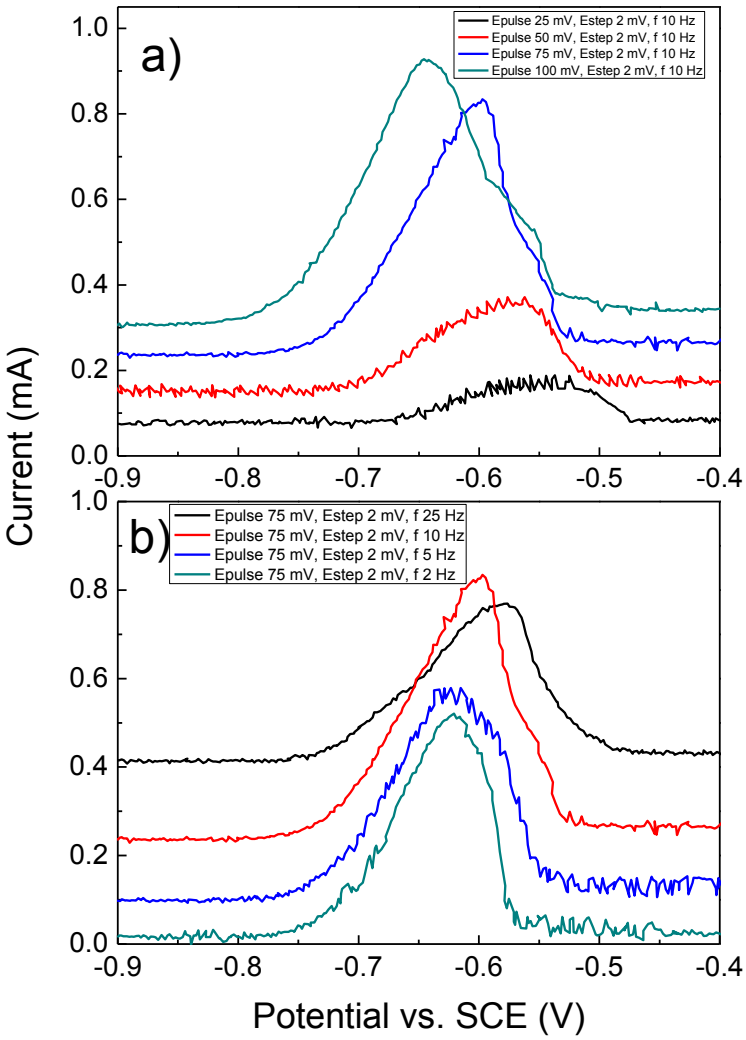

Figure 4.2.4 Square Wave Anodic Stripping Voltammograms of Pb^{2+} 100 ppm obtained at pH 4.5: a) effect of E_{pulse} and b) effect of frequency (f) on the shape and intensity of peak.

The AFM analyses were performed by a Bruker-Innova microscope operating in high-amplitude mode and ultra-sharpened Si tips were used (MSNL-10 from Bruker, with anisotropic geometry, radius of curvature ~2 nm, tip height ~2.5 μm, front angle ~15°, back angle ~25°, side angle 22.5°). The Si tips were substituted as soon as a resolution loose was observed during the AFM images acquisition. The AFM images were analyzed by using the SPMLABANALYSES V7.00 software (Veeco Corp., Santa Barbara, CA, USA). The surface roughness was quantified by the RMS parameter defined as $RMS=\langle z(x, y)^2\rangle^{1/2}$ being $z(x, y)=h(x, y)-\langle h(x, y)\rangle$ with $h(x, y)$ the height function and $\langle z(x, y)\rangle$ the spatial average over a planar reference surface.

XPS characterization was obtained by VG Microtech CLAM4 instrument (see Paragraph 3.2.2). The binding energy scale has been corrected for surface charging up, assuming the C1s core-shell which originates from adventitious carbon contamination, at 284.8 eV. For the description and

characteristics of the other instrumental characterizations see Paragraphs 2.2.2 and 3.2.2.

4.3 Results and discussion

4.3.1 Morphology characterization

Figures 4.3.1a and 4.3.1b report the SEM images of the GP_Bi nanoelectrode acquired in the centre and at the edge, respectively, showing a significant amount of Bi nanostructures. In the centre of the active area small bismuth crystals were detected. Conversely, on the edge the growth of large dendritic (or nanowalls) crystals of bismuth was observed. The findings may be related to the presence of the step edges that are numerous at the cut edge of the graphene paper. Step edges of graphene planes favorite the bismuth nanoparticles growth. Some authors exploited the graphite step edge to grow selectively nanoparticles by modulating the potential in a pulsed electrode-position [168, 169]. Furthermore, a possible cause of the different bismuth content observed may be related to the inhomogeneity of the potential along the large active macroscopic area of the nanoelectrode.

Potential is expected higher on the borders, leading to an increased rate of bismuth electro-deposition. The ratio of the centre to edge areas is roughly 70 to 30; both types of regions are representative of the nanoelectrode. The pictures reported in Figure 4.3.1c refer to the edge of the sample GP_naf_ex_Bi. In this region, once again, dendritic crystals of bismuth were detected. The bismuth crystals are larger and more homogeneous with respect to the GP_Bi case. Figure 4.3.1d reports the SEM image of GP_Bi in the edge of the active area and the corresponding EDX chemical maps showing the specific contribution of bismuth and oxygen are reported in Figures 4.3.1e and 4.3.1f, respectively. The presence of oxygen signal is likely due to the surface oxidation of air exposed electrode. The SEM picture of the centre of GP_naf_ex_Bi (Figure 4.3.2) does not show features related to the bismuth nano-crystals, being formed mainly of porous film of ionomer.

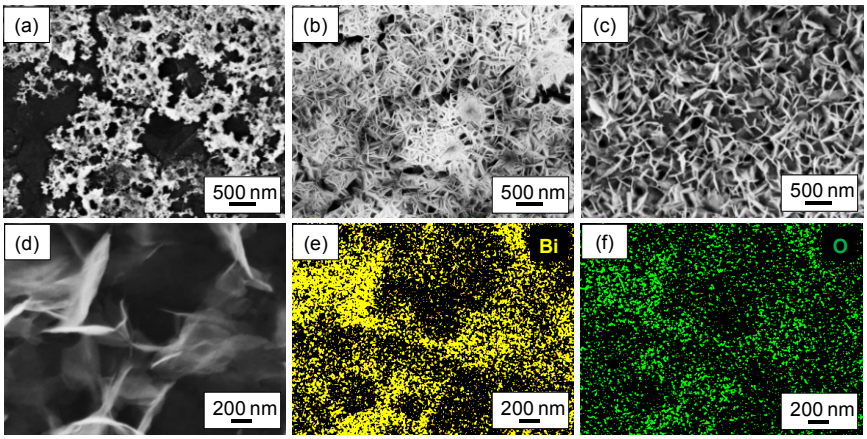

Figure 4.3.1 a) Scanning Electron Microscopy images of: a) GP_Bi in the centre; b) at the edge of the active area; c) GP_naf_ex_Bi at the edge of the active area; d) Scanning Electron Microscopy image and e-f) corresponding chemical maps obtained by Energy Dispersive X-ray Spectroscopy images of bismuth and oxygen of GP_Bi at the edge of the active area.

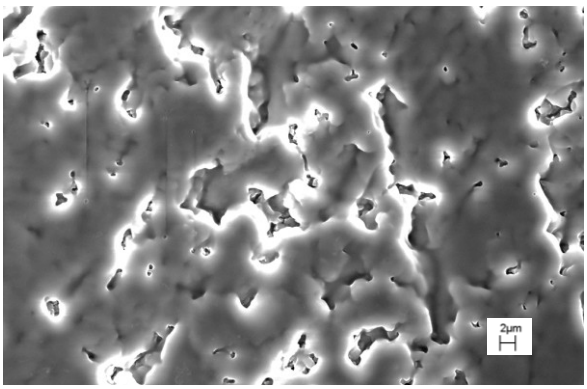

Figure 4.3.2 Scanning Electron Microscopy image of the GP_naf_ex_Bi in the centre of active area. The surface morphology is characterized by significant porosity that is useful to improve the nanoelectrode sensitivity.

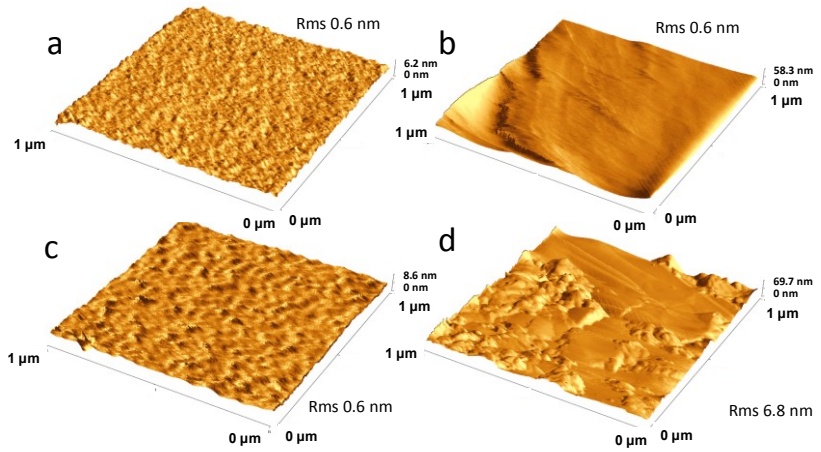

Figure 4.3.3 Atomic Force Microscopy images of a) GP_naf_ex_Bi before Bi electro-deposition; b)-d) GP_naf_ex_Bi in three different representative regions.

AFM analyses have been performed to further characterize this region (Figure 4.3.3). The AFM analysis with a lateral scan of 1 µm of the GP_naf_ex_Bi before the Bi deposition (a) shows that the nanoelectrode surface is flat with a roughness characterized by a rms of 0.6 nm. After bismuth deposition the surface of GP_naf_ex_Bi shows three different representative regions. The first (b) is characterized by absence of significant features and by a roughness with RMS of 0.6 nm. The second (c) shows very small structures, with a lateral size in the range of few nm, with height of 1-1.5 nm homogeneously distributed on the surface. The roughness has

an RMS 0.6 nm. The third region (d) shows aggregated structures that exhibits a lateral size of about 100 nm and height of about 10-20 nm (roughness 6.8 nm). I attributed the structures to the bismuth nanoparticles. The characterization of the GP_naf_Bi was not reported because this electrode does not show improvements of the analytical performance (see next Paragraph). The results of SEM and AFM investigations show the presence of a high density of bismuth nanoparticles whose morphology depends on the different nanoelectrode structure (presence of nafion).

4.3.2 Analytical performance

Figure 4.3.4 reports typical voltammograms obtained by GP_Bi nanoelectrode of Pb^{2+} at concentrations of 25 (red line) and 200 (black line) ppb, respectively. The voltammograms show two peaks centered at about -0.67 and -0.22 V vs. SCE that are assigned to Pb^{2+} and Bi^{3+}, respectively [151]. The anodic stripping peak corresponding to Bi^{3+} is typically broad and exhibits asymmetry that may be attributed to different Bi phases, structures or partial bismuth oxidation. Broad Bi peak was observed by Zhao using a double Bi deposition technique and MWCNT–Nafion/glassy carbon electrode [151]. The peak of Pb^{2+} at concentration of 25 ppb is slightly shifted and centered at about -0.70 V.

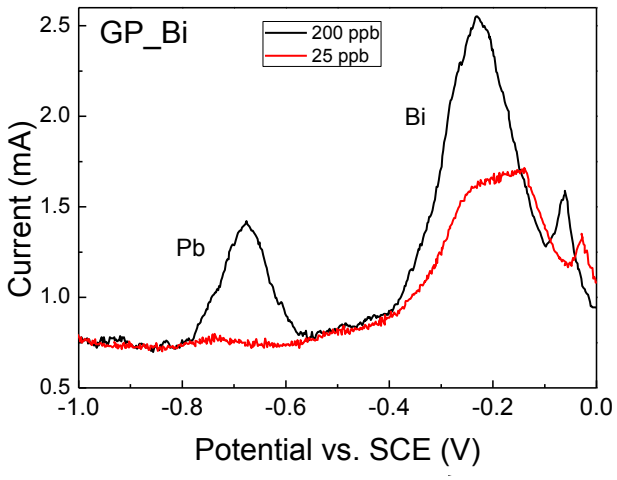

Figure 4.3.4 Square Wave Anodic Stripping voltammograms of Pb^{2+} at concentrations of 200 and 25 ppb, respectively, obtained at pH 4.5, pulse height 75 mV, step 2 mV and frequency 2 Hz, by GP_Bi.

Afterwards, the case of simultaneous detection of cadmium and lead has been considered. Figure 4.3.5a shows the SWASV of simultaneous detection of Pb^{2+} and Cd^{2+} at concentration of 200 ppb by GP_Bi (red line), GP_naf_Bi (blue line) and GP_naf_ex_Bi (black line) nanoelectrodes, respectively. Voltammograms show well-defined, intense and resolved peaks corresponding to Cd^{2+} and Pb^{2+} and Bi^{3+}.

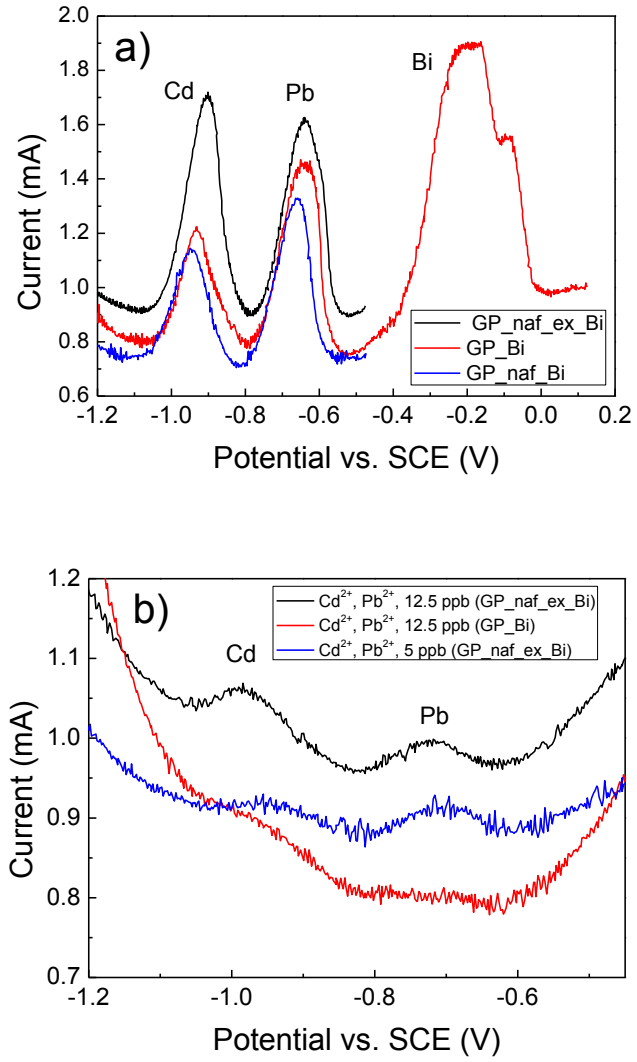

Figure 4.3.5 Square Wave Anodic Stripping voltammograms of Cd^{2+} and Pb^{2+} at concentration of: a) 200 ppb obtained by GP_naf_ex_Bi, GP_Bi and GP_naf_Bi nanoelectrodes; (b) 12.5 and 5 ppb obtained by GP_Bi and GP_naf_ex_Bi nanoelectrodes. Conditions: pH 4.5, pulse height 75 mV, step 2 mV and frequency 2 Hz.

The characteristic peaks of Cd^{2+} and Pb^{2+} are observed at -0.93 V and -0.65 V vs. SCE for GP_Bi, at -0.95 V and -0.67 V vs. SCE for GP_naf_Bi and at -0.91 V and -0.63 V vs. SCE for GP_naf_ex_Bi, respectively. The values of stripping peaks of lead and cadmium are very close to that reported in literature [151, 161]. The observed variations in the stripping potentials of Pb^{2+} and Cd^{2+} may be related to the variation of impedance modulus of the nanoelectrodes (as discussed later on). The GP_naf_ex_Bi nanoelectrode shows a significant increase of the response towards the Cd^{2+} detection, with respect to the other two nanoelectrodes. Conversely, the GP_naf_Bi nanoelectrode shows a reduced response of both Cd^{2+} and Pb^{2+} detection compared with the other nanoelectrodes. The explanation of this finding is not straightforward. The experimental finding may be attributed to a minor number of active sites in the GP_naf_Bi with respect to GP_naf_ex_Bi nanoelectrode. Further considerations will be discussed later on. The analytical performance of GP_naf_Bi is worst also compared with the

GP_Bi nanoelectrode, because shows the lowest peak current intensity both for lead and cadmium stripping. Figures 4.3.5b shows the voltammograms of simultaneous detection of Pb^{2+} and Cd^{2+} at concentrations of 12.5 ppb and 5 ppb by GP_Bi and GP_naf_ex_Bi nanoelectrodes, respectively. In the voltammogram of the latter nanoelectrode, the peaks are well defined and centered at -0.97 V and -0.72 V vs. SCE, respectively. The shift of the stripping potentials of Cd^{2+} and Pb^{2+} at low concentration with respect to that observed at concentration of 200 ppb occurs because the amount of deposited and, then, of stripped metals is different, as previous reported by other authors [170, 171]. Figure 4.3.6a reports the calibration curves for simultaneous detection of cadmium and lead by GP_Bi, in the concentration range of 12.5-200 ppb. The response curve of lead alone was also reported. The calibration curves were constructed from the voltammograms by measuring the intensity of the anodic peaks of cadmium and lead at various analyte concentrations, by subtracting the baseline. The error bars represents the

standard deviation calculated on five measurements. The simultaneous co-deposition and stripping of cadmium and lead does not worsen significant the current responses. The GP_Bi nanoelectrode shows a linear response in the overall range with good linear fittings I(μA) = -19 + 3.99c (ppb) characterized by linear correlation coefficients R^2 of 0.983 (Pb alone), I(μA) = -35.6 + 3.56c (ppb), R^2 0.814 and I(μA) = -27.4 + 3.43c (ppb), R^2 0.917 for Pb^{2+} and Cd^{2+}, in simultaneous analysis, respectively. Calibration curves for simultaneous detection of Cd^{2+} and Pb^{2+} obtained by the GP_naf_ex_Bi nanoelectrode are reported in Figure 4.3.6b. Linear response has been observed in the concentration range of 5-100 ppb I(μA) = -14.7 + 7.36c (ppb) with R^2 of 0.984 and I(μA) = -18.4 + 7.41c (ppb) with R^2 0.988 for Pb^{2+} and Cd^{2+}, respectively. The fitting lines are very close together and not distinguishable in the plot. The slopes of current responses by GP_naf_ex_Bi nanoelectrode are higher than that observed by GP_Bi nanoelectrode. In particular, 3.56 and 3.43 μA/ppb by GP_Bi and 7.36 and 7.41 μA/ppb by GP_naf_ex_Bi for

Pb^{2+} and Cd^{2+}, respectively, are observed. Table 4.3.1 reports the limit of detection (LOD) of Cd^{2+} and Pb^{2+} by the GP_Bi and GP_naf_ex_Bi nanoelectrodes calculated by the lest square regression line method and the linear detection range. LOD was estimated by the least square regression line method $LOD = 3\ S_{y/x} \cdot b^{-1}$, where $S_{y/x}$ represents the uncertainty of slope of the regression line and b is the slope of the signal/concentration functional relationship, obtained by least squares regression [172]. For comparison, Table 4.3.1 reports some of the most performing literature electrodes used in SWASV and differential pulse anodic stripping voltammetry (DPASV), for the detection of cadmium and lead. Moreover, in the third column of Table 4.3.1 numbers of fabrication steps of the electrode employed by various authors are reported. According, our results are encouraging and competitive with many studies for the Cd^{2+} and Pb^{2+} detection. The best performing nanoelectrode is the GP_naf_ex_Bi one, demonstrating the efficient Bi ion exchange step.

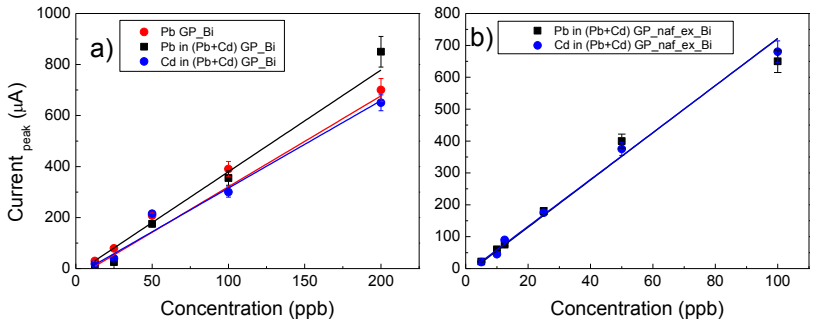

Figure 4.3.6 a) Current calibration curves for Pb^{2+} and for simultaneous Cd^{2+} and Pb^{2+} determination by GP_Bi nanoelectrode, in the concentration range of 12.5-200 ppb; b) current calibration curves for Cd^{2+} and Pb^{2+} determination by GP_naf_ex_Bi nanoelectrode in the concentration range of 5-100 ppb. Conditions: pH 4.5, pulse height 75 mV, step 2 mV and frequency 2 Hz.

Table 4.3.1 Limit of detection (LOD) and linear detection range of Cd^{2+} and Pb^{2+} by the GP_Bi and GP_naf_ex_Bi nanoelectrodes obtained by the least square regression line method. For comparison, some of the most performing electrodes described in literature are reported.

Analyte	Electrode structure	Steps of production[1]	LOD (ppb)		Method	Linear detection range (ppb)	Ref.
			Cd^{2+}	Pb^{2+}			
Pb + Cd	Bi dendritic on glassy carbon H_2 template	2	0.4	0.1	SWASV	5-50	170
Pb + Cd + Zn	Nafion coated Bi electrode	5	0.17	0.17	DPASV	4-36	163
Pb + Cd	Mesoporous graphene	5	0.5	0.1	DPASV	0.5-110	155
Pb + Cd	MWCNT + graphene oxide	16	0.1	0.2	DPASV	0.5-30	145
Pb + Cd	Bi PSS composite	5	0.1	0.27	DPASV	5-40	157
Pb + Cd	Graphene oxide + nafion + BMIM-PF_6 [2]	7	0.33	0.42	SWASV	2.4-70	162
Pb	Bi electro-deposition on graphene paper	1	-	0.15	SWASV	12.5-200	This work
Pb + Cd	Bi electro-deposition on graphene paper	1	0.25	0.12	SWASV	12.5-200	This work
Pb + Cd	nafion deposition on graphene paper, Bi^{3+} ion exchange + Bi electro-deposition	3	0.1	0.1	SWASV	5-100	This work

[1] Graphene paper, graphene or graphene oxide preparation steps are not included.

[2] 1-Butyl-3-methylimidazolium hexafluorophosphate.

4.3.3 Electrode stability

The stability of GP_naf_ex_Bi nanoelectrode was evaluated measuring the current response 75 days after the preparation. The test has the aim to estimate the storage time at room temperature of the electrodes for their reliable use. Before the use the aged electrodes were re-hydrated by soaking overnight into acetic buffer solution. Alternatively, they can be stored in wet condition into a sealed sachet. Figure 4.3.7 reports the histogram of the current response for the simultaneous detection of Cd^{2+} and Pb^{2+} at the concentrations of 200 and 5 ppb, registered by fresh and 75 days stored electrodes, respectively. Little variation, within the experimental error, in the current response was observed by the aged electrodes, indicating, however, good stability. The stability is competitive with that of some literature references, e.g. tested after only 15 days of storage at 5 °C, which retain about 96 % of initial response [162].

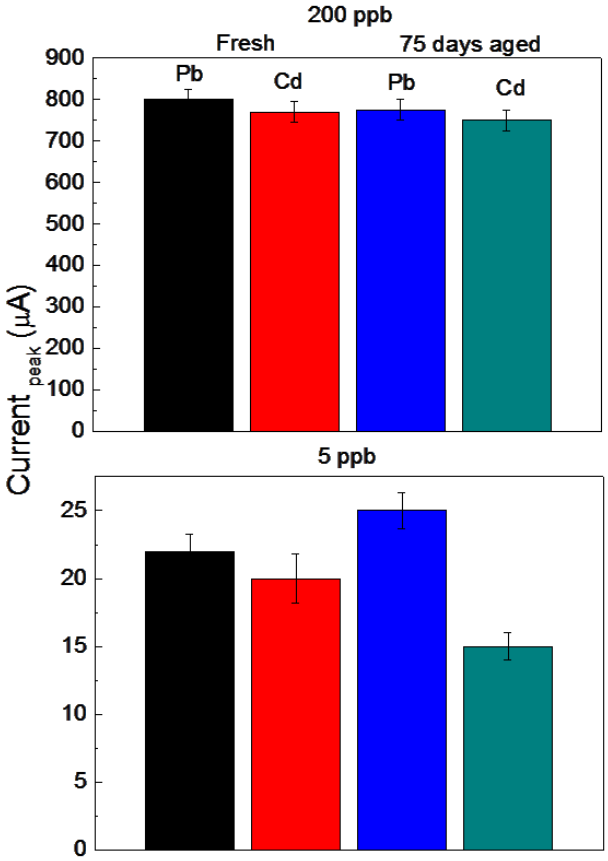

Figure 4.3.7 Current response for Pb^{2+} and Cd^{2+} at concentrations of 200 and 5 ppb, respectively, by fresh and 75 days aged at room temperature GP_naf_ex_Bi electrode. Conditions: pH 4.5, pulse height 75 mV, step 2 mV and frequency 2 Hz.

4.3.4 Electrochemical impedance spectroscopy of nanoelectrodes

The EIS were done before (GP, GP_naf, GP_naf_ex electrodes, respectively) and after the electro-deposition of Bi (GP_Bi, GP_naf_Bi, GP_naf_ex_Bi nanoelectrodes, respectively). Figure 4.3.8a reports the Bode plot of impedance (modulus). The impedance was measured in the frequency range of 10^{-1} - 10^{4} Hz. Figure 4.3.8b reports the corresponding Bode plot for the impedance phase. The presence of bismuth reduces the modulus of the impedance and values of phase in the explored frequency range, in all electrodes. Figure 4.3.8c reports the Nyquist plot of the imaginary impedance component (Zim) as function of real impedance component (Zre). The plot shows that the lowest values of both Zim and Zre impedances are exhibited by the GP_naf_ex_Bi nanoelectrode (see inset in Figure 4.3.8c). According to our findings, low impedance of the electrode is expected to improve the analytical performances in SWASV,

both in the metal accumulation step as well as increasing the stripping current.

The observed variation in the impedance modulus and phase can be related to the physico-chemical properties of the nanoelectrodes. The GP_naf_Bi nanoelectrode shows an increase of the impedance modulus and phase with respect to GP_Bi. This may be related to the presence of ionomer layer not completely saturated by Bi^{3+} and Bi^{0} nanoparticles. In fact, the duration of bismuth electro-deposition (1200 s) may be insufficient for the complete diffusion of Bi^{3+} into the nafion layer. Ion exchange step in the preparation of GP-naf_ex_Bi nanoelectrode produces a reduction of impedance modulus and phase, in particular at low frequencies. In this case the overnight soaking into bismuth solution allows to the Bi^{3+} ions to completely diffuse into the ionomer layer. Moreover, Figure 4.3.8d reports the histogram that compares the modulus of impedance and phase measured at a frequency of 0.1 Hz, to facilitate visualization. This frequency is close to that adopted in the SWASV. Low electrode impedance is expected to

improve the detection sensitivity, thus the combination of ion exchange and Bi deposition in the electrode preparation allows an improvement of the electrode performances.

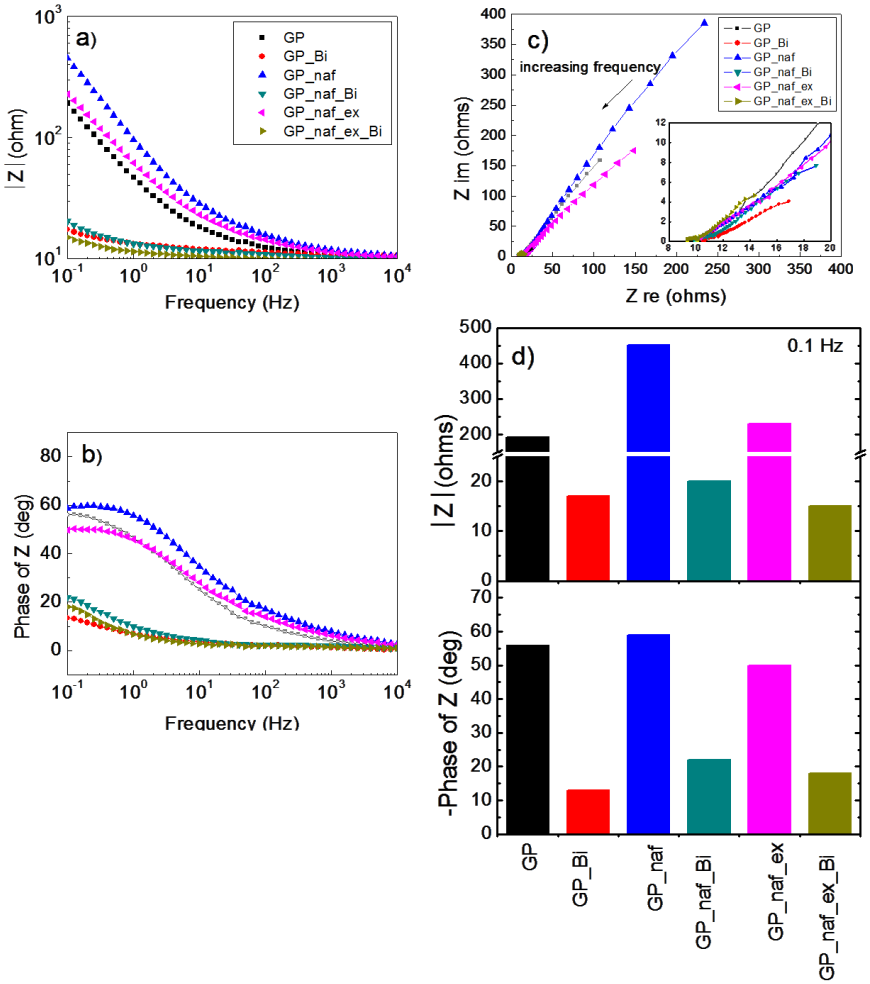

Figure 4.3.8 a) Modulus of impedance as function of frequency for different electrodes, measured before and after Bi deposition; b) corresponding phase spectra; c) corresponding Nyquist plot; d) impedance modulus |Z| (ohms) and phase of Z (deg) of electrodes measured at a frequency of 0.1 Hz. Solution: 100 ppm of Bi^{3+} in 0.1 M acetic buffer at pH 4.5.

4.3.5 XPS characterization of the electrode surface

XPS analyses were performed on the most performing GP_naf_ex_Bi nanoelectrode, to better understand the chemistry of Pb and Cd detection. Survey XPS spectrum (not shown) exhibits the F, O, C, Na, S and Bi signals. Figure 4.3.9a shows the XPS C 1s core-shell spectrum that was deconvoluted by four Gaussian components centered at 293, 292, and 288 eV that are assigned to CF_3-, -CF_2-, -$CF(CF_3)O$- functional groups, respectively, characteristics of the nafion structure [172]. The weak component centered at 284.8 eV can be attributed to adventitious carbon. Figure 4.3.9b shows the XPS spectrum in the 180-150 eV of binding energy regions, which comprises the S 2p and Bi 4f core-shell signals. The spectrum was deconvoluted using four Gaussian components centered at 154.7 eV (assigned to Bi° $4f_{7/2}$), 159.4 eV (Bi° $4f_{5/2}$), 160.4 eV (Bi(III)-sulfone $4f_{7/2}$) and 166 eV (Bi(III)-sulfone $4f_{5/2}$). Moreover, two additional components at binding energy of 164 eV and 172.3 eV (each formed by not resolved S $2p_{1/2}$

and $S2p_{3/2}$ doublets) were assigned to R-SH/R-S-R' and sulfonic groups, respectively [173]. The R-SH/R-S-R' groups maybe formed during electrochemical reduction at the bismuth deposition step. The –SH group has a high binding affinity towards lead and cadmium ion, which acts as chelating specie, further improving the electrode sensitivity [174]. The XPS spectrum suffers of differential charging up, due to the insulating nature of nafion in the dry condition. As consequence of the differential charging up, the binding energy assigned to Bi^0 $4f_{7/2}$ and $R\text{-}SO_3^-$ S 2p are slightly different with respect to the literature references. The differential charging up effect, often, is a powerful tool and helps in the structural study of nanomaterials [175, 176]. The observed differential charging up between the Bi^0 and Bi(III) components present in the spectrum of Figure 4.3.9 may be attributed to the presence of bismuth in the forms of Bi(III) as well as in the metallic Bi^0. Component peak areas were used to calculate the concentration of bismuth in comparison to the sulfur groups, as far as the chemical composition of the first

layers can be measured relatively to the technique resolution. Atomic sensitivity factors of 9.19 and 0.668 for Bi4f and S2p respectively, were used [177]. The relative composition of Bi°, Bi(III) and sulfur containing groups is reported in Table 4.3.2. The overall amount of bismuth is about one third of the amount of sulfur containing groups.

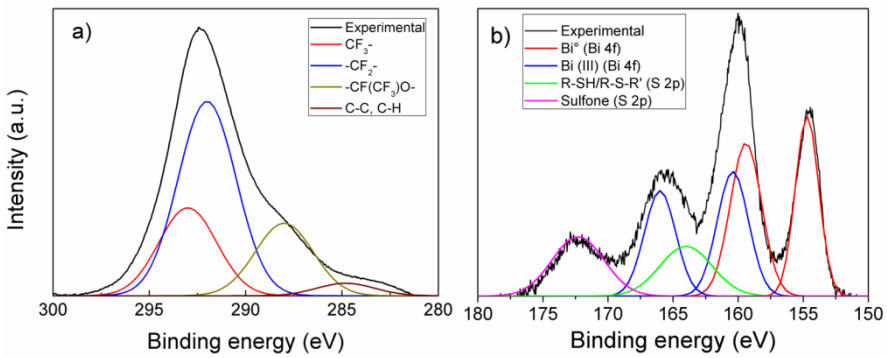

Figure 4.3.9 a) C 1s and b) S2p and Bi 4f X-ray Photoelectron core-shell spectra of GP_naf_ex_Bi.

Table 4.3.2 Elemental composition (atomic concentration %) corresponding to Bi°, Bi(III), R-SO_3^- and R-SH/R-S-R' of GP_naf_ex_Bi nanoelectrode.

	Bi°	Bi(III)	R-SO_3^-	R-SH/R-S-R'
GP_naf_ex_Bi	16.2	11.2	39.5	33.1

4.3.6 Interfering species and application to real sample analysis

The applicability of the proposed nanoelectrode to the analysis of real sample of drinking water could be, in principle, affected by the presence of interfering species. Interfering species maybe expected by metal ions that can compete with Pb^{2+} or Cd^{2+} for the active sites on the electrode surface. Zhao [153] has identified Cu^{2+} as the most common interfering ion in the detection of Pb^{2+} and Cd^{2+} in soil analysis. However, this interfering agent can be eliminated by precipitation with ferrocyanide before Pb and Cd analysis. Segura [161] for an electrode similar to ours found that Fe^{3+}, Mo^{3+}, Cu^{2+}, As^{3+}, Al^{3+}, Zn^{2+}, Co^{2+}, and Ni^{2+} ions do not cause significant interfering effect in the analysis of water real samples. Additionally, interference can also be due to species present in real samples that complex the metal ions such as CN^-, oxalate, NH_3. As good practice, it is recommended to eliminate the interfering species before performing the

analysis. On the other hand, the analysis of drinking water still requires the use of pH buffer reagents (acetic acid and sodium acetate) using the standard addition method, which provide the buffering of pH and also the stabilization of ion strength, limiting the matrix effects of potential interfering ions. According to previous studies performed by electrodes similar to ours [161, 170], the proposed nanoelectrode can be successful applicable to the analysis of real samples of drinking water.

4.4 Conclusions

Facile, reproducible, stable and low cost sensor for ultra-trace and simultaneous analysis of Cd^{2+} and Pb^{2+} by square wave anodic stripping voltammetry has been proposed. The sensor consists of graphene paper, a film of nafion and dispersed bismuth particles few nm large. The adopted ion exchange step allows the bismuth ions to be readily available for the electrochemical reduction inside the ionomer. Ion exchange and electro-deposition steps produce a finely dispersion of bismuth nanoparticles in the ionomer film.

During the electro-deposition of bismuth, the sulfonic groups are partially reduced to –SH and organic sulfides, which further improves the electrode sensitivity, particularly towards cadmium. EIS shows that the GP_naf_ex_Bi nanoelectrode presents the lowest impedance over the entire explored frequency range. In the latter nanoelectrode a combination of adsorptive and alloying-based mechanisms is active in the accumulation of heavy metals. Three main

mechanisms can be taken into account to explain the high sensitivity of the nanoelectrode: a) negative charges of sulfonic groups $-SO_3^-$ in the nafion attract the positive ions and repulse the negative counter ions; b) the sulfonic and its reduced group thiol –SH bind the Cd^{2+} and Pb^{2+} ions increasing the accumulation; c) finely dispersed metallic bismuth binds the reduced cadmium and lead to form metallic alloys. The sensor shows good stability and unmodified response to both Cd^{2+} and Pb^{2+} after almost three months from its preparation. The analytical performance is very competitive to the state of the art concerning electrodes for the detection of heavy metals by SWASV.

Conclusions

Nanomaterials have great potentials of development and application for the fabrication of facile, low cost and reliable nanoelectrodes for electro-analysis applied in human health and environmental monitoring. Despite the large effort done by the scientific community, an increasing demand for low-cost, sensitive, easy reading and friendly user electrodes still exists.

The demand of sensors is of significant evidence in the monitoring of physico-chemical parameters of interest in human health and environmental monitoring, such as pH of Earth's water and human body fluids, glucose and fructose

detection in human blood and industrial applications and heavy metals detection at sub-ppb level in drinking water.

In this PhD thesis, I presented three research topics concerning the potential applications of some classes of nanomaterials for the fabrication of nano electrochemical sensors; the first topic is related to the microscopic mechanisms that influence the sensitivity of pH sensors based on zinc oxide nanostructures. Nanowalls made of zinc hydroxynitrate or ZnO structures have been prepared by chemical bath deposition and the potentiometric response to pH 4, 7 and 9 was evaluated. Zinc hydroxynitrate showed a super-Nernstian behavior (+83.7 mV/decade) with transient response depending on the pH value. This was explained with the insertion of H^+ into octahedral empty sites and with a secondary simultaneous and independent complexing of H^+ that forms bridging bond between two NO_3^- groups from two vicinal zinc hydroxide layers. Zinc oxide NWLs showed a sub-Nernstian behavior (+27.1 mV/decade) with transient response almost independent of the pH value. In this case a

simultaneous and independent response to H^+ and OH^- of zinc oxide explain the evidenced sensitivity. In a similar manner here reported, the described model could explain the different literature data, if all the involved parameters are fully taken into accounts. From a practical point of view, zinc oxide nanowalls confirm their sensitivity toward H^+ activity in solution and their great potential to be used as disposable, low cost, environmental friendly nanoscale pH sensors.

In the second research topic, I show the feasibility of fabrication of non-enzymatic electrochemical sensors based on nanostructures of gold onto graphene paper substrate for sensitive glucose and fructose determination. The proposed fabrication methods are characterized by few simple and fully dry steps, compared to the literature methods, which are, however, based on multi-steps solution processes and/or on the use of enzymes. The nanoelectrodes have been prepared by furnace or laser dewetting of 1.6 or 8 nm thick gold layers onto graphene paper. One of the main difference exhibited by the solid state (furnace) and liquid state (laser) dewetting lies

in the size and shape of the resulting nanostructures. Laser dewetting originates particles with size in the ranges of 10-150 nm. Furnace dewetting originates faceted nanostructures with typical size of 200-400 nm. The particles obtained by laser dewetting are almost spherical, while those obtained by furnace process present a characteristic faceting. Moreover, laser dewetted electrodes show a high electro-catalytic activity even at very low gold content as 3.85×10^{15} Au cm^{-2}.

Both type of nanoelectrode exhibited a high sensitivity for glucose detection up to 1240 $\mu A \cdot mM^{-1} \cdot cm^{-2}$, low detection limit down to 2.5 μM and wide linear range (15 μM- 8 mM). The nanoelectrodes show good response for the detection of fructose, and good stability (possibility of reusing the test stripes tested up to 50 times even after 6 months). Compared to the methods reported in literature, the fabrication methods here proposed are characterized by low cost if compared to the high throughput, simplicity, high purity of the electrode, absence of toxic materials and low generation of dangerous waste during the production. The proposed nanoelectrodes are

expected to be biocompatible for the absence of metals such as nickel or copper. Moreover, the absence of wet chemical processes and, then, of ion contamination, makes more easy the integration of the proposed nanoelectrodes with microelectronic silicon chip for the circuit conditioning, data acquisition and processing. The resulting analytical performances for the glucose and fructose detection are very promising since comparable or better than the actual state of art for nanostructured gold electrodes.

Finally, I described facile, reproducible, stable and low cost sensors for ultra-trace and simultaneous analysis of Cd^{2+} and Pb^{2+} by square wave anodic stripping voltammetry. The sensor consists of graphene paper substrate, a film of nafion deposited onto graphene paper containing dispersed bismuth particles few nm large. The adopted ion exchange step allows the bismuth ion to be readily available for the electrochemical reduction inside the ionomer. Ion exchange and electro-deposition steps produce a finely dispersion of bismuth nanoparticles in the ionomer film. During the electro-

deposition of bismuth, the sulfonic groups are partially reduced to –SH which further improves the electrode detection limit, particularly towards cadmium. EIS shows that the GP_naf_ex_Bi nanoelectrode presents the lowest impedance over the entire explored frequency range. In the latter electrode a combination of adsorptive and alloying-based mechanisms is active in the accumulation of heavy metals. Three main mechanisms can be taken into account to explain the low detection limit of the electrode: a) negative charges of sulfonic groups $-SO_3^-$ in the nafion attract the positive ions and repulse the negative counter ions; b) the sulfonic and its reduced group thiol –SH bind the Cd^{2+} and Pb^{2+} ions increasing the accumulation; c) finely dispersed metallic bismuth binds the reduced cadmium and lead to form metallic alloys. The sensor shows good stability and unmodified response to both Cd^{2+} and Pb^{2+} after almost three months from its preparation. The analytical performance is very competitive to the state of the art concerning electrodes for the detection of heavy metals by SWASV.

The scientific literature and the research activity of this PhD thesis shows that the best performances in several fields of electro-analysis are obtained by nanostructures formed by carbon based matrices in combination with nanostructures of metals as oxides-hydroxides or in the metallic state. In future perspectives, the use of nanomaterials in electro-analysis is expected to further increases. In particular, hybrid nanostructured carbon materials and metal nanoparticles obtained by non-conventional fabrication methods still deserve further investigation of potential fields of application.

References

[1] C.M. Welch, R.G. Compton, The use of nanoparticles in electroanalysis: a review, Anal. Bioanal. Chem. 384, (2006), 601–619 DOI 10.1007/s00216-005-0230-3.

[2] L.A. Kolahalam, I.V. Kasi Viswanath, B.S. Diwakar, B. Govindh, V. Reddy, Y.L.N. Murthy, Review on nanomaterials: Synthesis and applications, Mat. Today Proc. 18, (2019), 2182–2190.

[3] L. Falciola, lesson to Introduction to Electrochemical Methods of Analysis, Università degli Studi La Statale di Milano (Italy).

[4] A.O. Simm, S. Ward-Jones, C.E. Banks, R.G. Compton, Novel Methods for the Production of Silver Microelectrode-Array: Their Characterisation by Atomic Force Microscopy and Application to the Electro-reduction of Halothane, Anal. Sci. 21, (2005), 667-671.

[5] S. J. Hood, D. K. Kampouris, R. O. Kadara, N. Jenkinson, F. Javier del Campo, F. X. Muñoz and C. E. Banks, Why 'the bigger the better' is not always the case when utilizing microelectrode arrays: high density vs. low density arrays for the electroanalytical sensing of chromium(VI), Analyst, 2009, 134, 2301–2305,

[6] A.J. Bard, L.R. Faulkner, (1982) Electrochemical methods: fundamentals and applications. Wiley, New York.

[7] E. Katz, I. Willner, J. Wang, Electroanalytical and Bioelectroanalytical Systems Based on Metal and Semiconductor Nanoparticles, Electroanalysis, 16, (2004), 19-44, https://doi.org/10.1002/elan.200302930.

[8] A. Borunda, Ocean acidification, explained. Available online: https://www.nationalgeographic.com/environment/oceans/critical-issues-ocean-acidification/. (Accessed on 17 August, 2020).

[9] National Oceanic and Atmospheric Administration: Ocean Acidification Program. Available online: https://oceanacidification.noaa.gov (Accessed on 17 August, 2020).

[10] E. Bruno, V. Strano, S. Mirabella, N. Donato, S.G. Leonardi and G. Neri, Comparison of the Sensing Properties of ZnO Nanowalls-Based Sensors Toward Low Concentrations of CO and NO_2, Chemosensors 5, (2017), 20; doi:10.3390/chemosensors5030020.

[11] Z. Lin Wang, Zinc oxide nanostructures: growth, properties and applications, J. Phys., Condens. Matter 16, (2004), R829–R858.

[12] K.O. Iwu, V. Strano, A. Di Mauro, G. Impellizzeri, and S. Mirabella, Enhanced Quality, Growth Kinetics, and Photocatalysis of ZnO Nanowalls Prepared by Chemical Bath Deposition, Cryst. Growth Des. 15, (2015), 4206–4212.

[13] Y. Ya, C. Jiang, T.Li, J. Liao, Y. Fan, Y. Wei, F. Yan and L. Xie, A Zinc Oxide Nanoflower-Based Electrochemical Sensor for Trace Detection of Sunset Yellow, Sensors 17, (2017), 545; doi:10.3390/s17030545.

[14] C. Ye, Y. Bando, G. Shen, and D. Golberg, Thickness-Dependent Photocatalytic Performance of ZnO Nanoplatelets, J. Phys. Chem. B 110, (2006), 15146-15151.

[15] A. Tsukazaki, A. Ohtomo, T. Onuma, M. Ohtani, T.Makino, M. Sumiya, K. Ohtani, S.F. Chichibu, S. Fuke, Y. Segawa, H. Ohno, H. Koinuma, M. Kawasaki, Repeated temperature modulation epitaxy for p-type doping and light-emitting diode based on ZnO, Nat. Mater. 4, (2005), 42.

[16] A. Janotti and C.G. Van de Walle, Fundamentals of zinc oxide as a semiconductor, Rep. Prog. Phys. 72, (2009), 126501

[17] W. Liu, Preparation of a Zinc Oxide-Reduced Graphene Oxide Nanocomposite for the Determination of. Cadmium(II), Lead(II), Copper(II), and Mercury(II) in Water, Int. J. Electrochem. Sci., 12, (2017), 5392 – 5403, doi: 10.20964/2017.06.06.

[18] A. Rodrigues, M.V. Castegnaro, J. Arguello, M.C.M. Alves, J. Morais, Development and surface characterization of a glucose biosensor based on a nanocolumnar ZnO film, Appl. Surf. Sci. 402, (2017), 136–141.

[19] S. M. Fulati, A. Usman, M. Riaz, G. Amin, O. Nur and M. Willander, Miniaturized pH Sensors Based on Zinc Oxide Nanotubes/Nanorods, Sensors 9, (2009), 8911-8923; doi:10.3390/s91108911.

[20] S. Kang, F. Ren, Y.W. Heo, L.C. Tien, D.P. Norton, and S.J. Pearton, pH measurements with single ZnO nanorods integrated with a microchannel, Appl. Phys. Lett. 86, (2005), 112105.

[21] P.Y. Yang, J.L. Wang, P.C. Chiu, J.C. Chou, C.W. Chen, H.H. Li, and H.C. Cheng, pH Sensing Characteristics of Extended-Gate Field-Effect Transistor Based on Al-Doped ZnO Nanostructures Hydrothermally Synthesized at Low Temperatures, IEEE Electron Device Lett. 32, (2011), 1603.

[22] J.L. Wang, P.Y. Yang, T.Y. Hsieh, C.C. Huang, and M.H. Juang, pH-Sensing Characteristics of Hydrothermal Al-Doped ZnO Nanostructures. J. Nanomater. (2013), 152079 https://doi.org/10.1155/2013/152079.

[23] L. Maiolo, S. Mirabella, F. Maita, A. Alberti, A. Minotti, V. Strano, A. Pecora, Y. Shacham-Diamand, and G. Fortunato, Flexible pH sensors based on polysilicon thin film transistors and ZnO nanowalls, Appl. Phys. Lett. 105, (2014), 093501 doi: 10.1063/1.4894805.

[24] S. J. Ahmadi, M. Hosseinpour, F. Javadi, and R. Tayebee, Optimization Study on Formation and Decomposition of Zinc Hydroxynitrates to Pure Zinc Oxide Nanoparticles in Supercritical Water, Ind. Eng. Chem. Res. 52, (2013), 1448–1454.

[25] V. Strano, R.G. Urso, M. Scuderi, K.O. Iwu, F. Simone, E. Ciliberto, C. Spinella, and S. Mirabella, Double Role of HMTA in ZnO Nanorods Grown by Chemical Bath Deposition, J. Phys. Chem. C, 118, (2014), 28189-28195.

[26] J. Auffrdic, E.D. Louër, Enthalpies de formation des hydroxinitrates. Thermochim. Acta 16, (1976), 223–229.

[27] S.P. Newman and W. Jones, Comparative Study of Some Layered Hydroxide Salts Containing Exchangeable Interlayer Anions, J. Solid State Chem. 148, (1999), 26-40.

[28] T. C. Bharat, Shubham, S. Mondal, H. S.Gupta, P. K. Singh, A. K. Das, Synthesis of Doped Zinc Oxide

Nanoparticles: A Review, Mater. Today: Proc. 11, (2019), 767–775.

[29] A. Cursino, J. da Costa Gardolinski, F. Wypych, Intercalation of anionic organic ultraviolet ray absorbers into layered zinc hydroxide nitrate, J. Colloid Interf. Sci., 347, (2010), 49.

[30] T. Yukia, S. Uenob, M. Hagiwaraa, S. Fujihara, Fabrication of layered hydroxide zinc nitrate films and their conversion to ZnO nanosheet assemblies for use in dye-sensitized solar cells, J. Asian Ceram. Soc. 3, (2015), 144–150.

[31] S.P. Newman and W. Jones, Comparative Study of Some Layered Hydroxide Salts Containing Exchangeable Interlayer Anions, J. Solid State Chem., 148, (1999), 26–40.

[32] W. Sun, K. Wu, M.A. Thomas, F. Meng, X. Song, Z. Sun, Z. Zhang and J. Cui, Current Oscillations in the Layer-by-Layer Electrochemical Deposition of Vertically Aligned Nanosheets of Zinc Hydroxide Nitrate, J.Electrochem. Soc., 160, (2013) D558–D564.

[33] Q. Hou, L. Zhu, H. Chen, H. Liu and W. Li, Growth of flower-like porous ZnO nanosheets by electrodeposition with $Zn_5(OH)_8(NO_3)_2•2H_2O$ as precursor, Electrochim. Acta, 78, (2012), 55–64

[34] P. Li, Z.P. Xu, M. A. Hampton, D.T. Vu, L. Huang, V. Rudolph, and A.V. Nguyen, Control Preparation of Zinc Hydroxide Nitrate Nanocrystals and Examination of the Chemical and Structural Stability, J. Phys. Chem. C 116, (2012), 10325–10332.

[35] M. Scuderi, V. Strano, C. Spinella, G. Nicotra and S. Mirabella, Low-cost synthesis of pure ZnO nanowalls

showing three-fold symmetry, Nanotechnology 29, (2018), 135707.

[36] E. L. Sciuto, C. Bongiorno, A. Scandurra, S. Petralia, T. Cosentino, S. Conoci, F. Sinatra and S. Libertino, Functionalization of Bulk SiO2 Surface with Biomolecules for Sensing Applications: Structural and Functional Characterizations, Chemosensors 6, (2018), 59; doi:10.3390/chemosensors6040059.

[37] Y. Zeng, Z. Zhu, D. Du, Y. Lin, Nanomaterial-based electrochemical biosensors for food safety, J. Electroanal. Chem. 781, (2016), 14–154.

[38] M. Medina-Sánchez, C.C. Mayorga-Martinez, T.W. Tribidasari, A. Ivandini, Y. Honda, F. Pino, K. Nakata, A. Fujishima, Y. Einaga, A. Merkoc, Microfluidic platform for environmental contaminants sensing and degradation based on boron-doped diamond electrodes, Biosens. Bioelectron. 75, (2016), 365–374.

[39] M. Guarnaccia, G. Gentile, E. Alessi, C. Schneider, S. Petralia, S. Cavallaro, Is this the real time for genomics, Genomics 103, (2014), 177–182.

[40] S. Chen, Y. Liu, C. Shao, R. Mu, Y. Lu, J. Zhang, D. Shen, X. Fan, Structural and optical properties of Uniform ZnO Nanosheets, Adv. Mater. 17, (2005) 5, 586 – 590.

[41] A. Sardarinejad, D. K. Maurya and K. Alameh, The pH Sensing Properties of RF Sputtered RuO2 Thin-Film Prepared Using Different Ar/O2 Flow Ratio, Materials 8, (2015), 3352-3363; doi:10.3390/ma8063352.

[42] P.D. Batista and M. Mulato, ZnO extended-gate field-effect transistors as pH sensors, Appl. Phys. Lett. 87, (2005), 143508.

[43] G. Kumar Mani, M. Morohoshi, Y. Yasoda, S. Yokoyama, H. Kimura, and K. Tsuchiya, ZnO-Based Microfluidic pH Sensor: A Versatile Approach for Quick Recognition of Circulating Tumor Cells in Blood, Appl. Mater. Interfaces, 9, (2017), 5193–5203 doi:10.1021/acsami.6b16261.

[44] M.P. Briggs, Seah (Eds.), Practical Surface Analysis, second edn, vol. 1, John Wiley & Sons, Chichester, (1990).

[45] J.F. Moulder, W.F. Stickle, P.E. Sobol and K.D. Bombe, Handbook of X-ray Photoelectron Spectroscopy, J. Castain Ed., published by Physical Electronics Division, USA (1992).

[46] R. Al-Gaashani, S. Radiman, A.R. Daud, N. Tabet, Y. Al-Douri, XPS and optical studies of different morphologies of ZnO nanostructures prepared by microwave methods, Ceram. Int., 39, (2013), 2283-2292.

[47] D. Steinle, S. Amemiya, P. Bühlmann, and M.E. Meyerhoff, Origin of Non-Nernstian Anion Response Slopes of Metalloporphyrin-Based Liquid/Polymer Membrane Electrodes, Anal. Chem. 72, (2000), 5766-5773.

[48] S. Amemiya, P. Bühlmann, and K. Odashima, A Generalized Model for Apparently Non-Nernstian Equilibrium Responses of Ionophore-Based Ion-Selective Electrodes. 1. Independent Complexation of the Ionophore with Primary and Secondary Ions, Anal. Chem. 75, (2003), 3329-3339.

[49] W. Stählin, H.T. Oswald, The Crystal Structure of Zinc Hydroxide Nitrate, Zn5(OH)8(NO3)2.2H2O, Acta Cryst., B26, (1970), 860.

[50] S. Nakagaki, K.M. Mantovani, G.S. Machado, K. Aparecida D. de Freitas Castro and F. Wypych, Recent Advances in Solid Catalysts Obtained by Metalloporphyrins Immobilization on Layered Anionic Exchangers: A Short Review and Some New Catalytic Results, Molecules 21, (2016), 291 doi:10.3390/molecules21030291.

[51] M.W. Allen, D. Y. Zemlyanov, G.I.N. Waterhouse, J.B. Metson, T.D. Veal, C.F. McConville, and S.M. Durbin, Polarity effects in the X-ray photoemission of ZnO and other wurtzite semiconductors, Appl. Phys. Lett. 98, (2011), 101906.

[52] S. Petralia, E.L. Sciuto, S. Conoci, A novel miniaturized biofilter based on silicon micropillars for nucleic acid extraction, Analyst 142, (2017), 140–146.

[53] Y. Zeng, Z. Zhu, D. Du, Y. Lin, Nanomaterial-based electrochemical biosensors for food safety, J. Electroanal. Chem. 781, (2016), 14–154.

[54] M. Medina-Sánchez, C.C. Mayorga-Martinez, T.W. Tribidasari, A. Ivandini, Y.Honda, F. Pino, K. Nakata, A. Fujishima, Y. Einaga, A. Merkoc, Microfluidic platform for environmental contaminants sensing and degradation based on boron-doped diamond electrodes, Biosens. Bioelectron. 75, (2016), 365–374.

[55] M. Guarnaccia, G. Gentile, E. Alessi, C. Schneider, S. Petralia, S. Cavallaro, Is this the real time for genomics, Genomics 103 (2014) 177–182.

[56] Diabetes, World Health Organization. Available online: https://www.who.int/news-room/fact-sheets/detail/diabetes. (Accessed on 19 July 2020).

[57] G. Schmelzeisen-Redeker, A. Staib, M. Strasser, U. Müller, M. Schoemaker, Overview of a novel sensor for

continuous glucose monitoring, J. Diabetes. Sci. Technol. 7, (2013), 808-814.

[58] Global Glucose Monitoring System Market Forecast 2019-2028. Available online: https://www.inkwoodresearch.com/reports/glucose-monitoring-system-marke, 169, Harrison avenue Boston, MA 02111, (accessed on May 14, 2020).

[59] Global Blood Glucose Sensor Market Research Report (2018), Marketresearchpro, https://marketresearchpro.net, 535 Middlefield Rd 280, Menlo Park,CA 94025, USA.

[60] S.L. Yu, D.C. Li, H. Chong, C.Y. Sun, K.X. Xu, Continuous glucose determination using fiber-based tunable mid-infrared laser spectroscopy, Opt. Lasers Eng. 55, (2014), 78–83.

[61] A.M. Wilson, T.M. Work, A.A. Bushway, R.J. Bushway, HPLC determination of fructose, glucose, and sucrose in potatoes, J. Food Sci. 46, (1981), 300–301.

[62] D. Nakayama, Y. Takeoka, M. Watanabe, K. Kataoka, Simple and precise preparation of a porous gel for a colorimetric glucose sensor by a templating technique, Angew. Chem. Int. Ed. 115, (2003), 4329–4332.

[63] J. Wang, Electrochemical glucose biosensors, Chem. Rev. 108, (2008), 814–825.

[64] T.M. Herne, M.J. Tarlov, Characterization of DNA probes immobilized on gold surfaces. J. Am. Chem. Soc., 119, (1997), 8916–8920.

[65] P.A.E. Piunno, U.J. Krull, Fiber-optic DNA sensor for fluorimetric nucleic acid determination. Anal. Chem., 67, (1995), 2635–2643.

[66] S. Libertino, M. Fichera, V. Aiello, G. Statello, P. Fiorenza, F. Sinatra, Experimental characterization of proteins immobilized on Si-based materials. Microelectron. Eng., 84, (2007), 468–473.

[67] S. Libertino, A. Scandurra, V. Aiello, F. Giannazzo, F. Sinatra, M. Renis, M. Fichera, Layer uniformity in glucose oxidase immobilization on SiO2 surfaces. Appl. Surf. Sci., 253, (2007), 9116–9123.

[68] S. Libertino, F. Giannazzo, V. Aiello, A. Scandurra, F. Sinatra, M. Renis, M. Fichera, XPS and AFM characterization of the enzyme glucose oxidase immobilized on SiO2 surfaces. Langmuir, 24, (2008), 1965–1972.

[69] S. Libertino, M. Fichera, V. Aiello, S. Lombardo, A. Scandurra, M. Renis, F. Sinatra, Electrical characterization of biological molecules deposition in MOS capacitors. Sens. Lett., 6, (2008), 531–536.

[70] Y.Y. Fu, F.F. Liang, H.F. Tian, J.B. Hu, Nonenzymatic glucose sensor based on ITO electrode modified with gold nanoparticles by ion implantation, Electrochim. Acta 120, (2014), 314–318.

[71] Y.J. Lee, S.J. Park, K.S. Yun, J.Y. Kang, S.H. Lee, Enzymeless glucose sensor integrated with chronically implantable nerve cuff electrode for in-situ inflammation monitoring, Sens. Actuators B Chem. 222, (2016), 425–432.

[72] S.J. Park, H.K. Boo, T.D. Chung, Electrochemical non-enzymatic glucose sensors, Anal. Chim. Acta 556, (2006), 46–57.

[73] X.H. Kang, Z.B. Mai, X.Y. Zou, P.X. Cai, J.Y. Mo, A sensitive non-enzymatic glucose sensor in alkaline media with a copper nanocluster/multiwall carbon nanotube

modified glassy carbon electrode, Anal. Biochem. 363, (2007), 143–150.

[74] Y. Zhong, T. Shia, Z. Liu, S. Cheng, Yuanyuan Huang, Xiangxu Taoa,Guanglan Liao, Zirong Tang, Ultrasensitive non-enzymatic glucose sensors based on different copper oxide nanostructures by in-situ growth, Sens. Actuators B Chem. 236, (2016), 326–333.

[75] M. Mathew, N. Sandhyarani, A highly sensitive electrochemical glucose sensor structuring with nickel hydroxide and enzyme glucose oxidase, Electrochim. Acta 108, (2013), 274–280.

[76] A. Saei, J.E.N. Dolatabadi, P. Najafi-Marandi, A. Abhari, M. de la Guardia, Elec-trochemical biosensors for glucose based on metal nanoparticles, Trends Anal. Chem. 42, (2013), 216–227.

[77] S. Petralia, E. L. Sciuto, M.A. Messina, A. Scandurra, S. Mirabella, F. Priolo, S. Conoci, “Miniaturized and multi-purpose electrochemical sensing device based on thin Ni oxides”, Sens. Actuators B Chem. 263, (2018), 10–19.

[78] H. Shekarchizadeh, M. Kadivar, A. A. Ensafi, Rapid nonenzymatic monitoring of glucose and fructose using a CuO/multiwalled carbon nanotube nanocomposite-modified glassy carbon electrode, Chinese J. Catal. 34, (2013), 1208–1215.

[79] X. Liu, W. Yanga, L. Chena, J. Jia, “Three-Dimensional Copper Foam Supported CuO Nanowire Arrays: An Efficient Non-enzymatic Glucose Sensor”, Electrochim. Acta 235, (2017), 519–526.

[80] T. Juríka, P. Podešvab, Z. Farka, D. Kovár, P. Skládal, F. Foret, Nanostructured gold deposited in gelatin template applied for electrochemical assay of glucose in serum, Electrochim. Acta 188, (2016), 277–285.

[81] M. Guo, P. Wang, C. Zhou, Y. Xia, W. Huang, Z. Li, An ultrasensitive non-enzymatic amperometric glucose sensor based on a Cu-coated nanoporous gold film involving co-mediating, Sens. Actuators B Chem. 203, (2014), 388–395.

[82] N. Stasyuk, O. Smutok, O. Demkiv, T. Prokopiv , G. Gayda, M. Nisnevitch and M. Gonchar, Synthesis, Catalytic Properties and Application in Biosensorics of Nanozymes and Electronanocatalysts: A Review, Sensors 20, (2020), 4509; doi:10.3390/s20164509.

[83] H. du Toit, M. Di Lorenzo, Electrodeposited highly porous gold microelectrodes for the direct electrocatalytic oxidation of aqueous glucose, Sens. Actuators B Chem. 192, (2014), 725–729.

[84] S. Hebie, L. Cornu, T.W. Napporn, J. Rousseau, B.K. Kokoh, Insight on the Surface Structure Effect of Free Gold Nanorods on Glucose Electrooxidation, J. Phys. Chem. C 117, (2013), 9872–9880.

[85] J.G. Wang, X.W. Cao, X. Wang, S. Yang, R. Wang, Electrochemical Oxidation and Determination of Glucose in Alkaline Media Based on Au (111)-Like Nanoparticle Array on Indium Tin Oxide Electrode, Electrochim. Acta 138, (2014), 174–186.

[86] M. Choudhary, S.K. Shukla, A. Taher, S. Siwal, K. Mallick, Organic-Inorganic Hybrid Supramolecular Assembly: An Efficient Platform for Nonenzymatic Glucose Sensor, ACS Sustain. Chem. Eng. 2, (2014), 2852–2858.

[87] B. Singh, E. Dempsey, F. Laffir, Carbon nanochips and nanotubes decorated PtAuPd-based nanocomposites for glucose sensing: Role of support material and efficient Pt utilisation, Sens. Actuators B Chem. 205, (2014), 401–410.

[88] J. Luo, S.S. Jiang, H.Y. Zhang, J.Q. Jiang, X.Y. Liu, A novel non-enzymatic glucose sensor based on Cu nanoparticle modified graphene sheets electrode, Anal. Chim. Acta 709, (2012), 47–53.

[89] X.H. Kang, Z.B. Mai, X.Y. Zou, P.X. Cai, J.Y. Mo, A novel sensitive non-enzymatic glucose sensor, Chin. Chem. Lett. 18, (2007), 189–191.

[90] H. Zhou, L. Jin, W. Xu, New approach to fabricate nanoporous gold film, Chin. Chem. Lett. 18, (2007), 365–368.

[91] S. Dawan, R. Wannapob, P. Kanatharana, W. Limbut, A. Numnuam, S. Samanman, P. Thavarungkul, One-step porous gold fabricated electrode for electrochemical impedance spectroscopy immunosensor detection, Electrochim. Acta 111, (2013), 374–383.

[92] S.Y. Huang, X.Y. Liu, Q.Y. Li, M.W. Meng, T.F. Long, H.Q. Wang, Z.L. Jiang, The preparation of nanoporous gold electrodes by electrochemical alloying/dealloying process at room temperature and its properties, Mater. Lett. 64, (2010), 2296–2298.

[93] C.R. Martin, D.T. Mitchell, Template-synthesized nanomaterials in electrochemistry, Electroanal. Chem. 21, (1999), 1–74.

[94] M. Kang, Sang-Gil Park and Ki-Hun Jeong, Repeated Solid-state Dewetting of Thin Gold Films for Nanogap-rich Plasmonic Nanoislands, Sci. Rep. 5, (2015), 14790 https://doi.org/10.1038/srep14790.

[95] Y.J. Oh, and K. H. Jeong, Glass Nanopillar Arrays with Nanogap-Rich Silver Nanoislands for Highly Intense Surface Enhanced Raman Scattering. Adv. Mater. 24, (2012), 2234–2237.

[96] R. Seemann, S. Herminghaus, and K. Jacobs, Dewetting Patterns and Molecular Forces: A Reconciliation, Phys. Rev. Lett. 86, (2001), 5534 –5537.

[97] F. Ruffino and M.G. Grimaldi, Controlled dewetting as fabrication and patterning strategy for metal nanostructures, Phys. Status Solidi A 212, (2015), 1662–1684 doi 10.1002/pssa.201431755.

[98] F. Ruffino and M.G. Grimaldi, Template-confined dewetting of Au and Ag nanoscale films on mica substrate, Appl. Surf. Sci. 270, (2013), 697– 706.

[99] J. Bischof, M. Reinmuth, J. Boneberg, S. Herminghaus, T. Palberg and Paul Leiderer, Behavior of Thin Metallic Films Melted with a Nanosecond Laser Pulse, Proc. Intern. Symp. on Adv. Mat. for Optics and Optoelectronics SPIE. 2777, (1996) 119–127.

[100] S. Herminghaus, K. Jacobs, K. Mecke, J. Bischof, A. Fery, M. Ibn-Elhaj, S. Schlagowski, Spinodal Dewetting in Liquid Crystal and Liquid Metal Films, Science, 282 (1998), pp. 916–919.

[101] R. L. McCreery, Advanced Carbon Electrode Materials for Molecular Electrochemistry, Chem. Rev. 108, (2008), 2646–2687.

[102] M. Zhou, Y. Zhai, and S. Dong, “Electrochemical Sensing and Biosensing Platform Based on Chemically Reduced Graphene Oxide”, Anal. Chem. 81, (2009), 5603–5613.

[103] P.T. Yin, T-H. Kim, J-W. Choi, and K-B. Lee, “Prospects for graphene–nanoparticle-based hybrid sensors”, Phys Chem Chem Phys. 15, (2013), 12785–12799.

[104] Y.J. Wan, P.L. Zhu, S.H. Yu, R. Sun, C.P. Wong, W.H. Liao, Graphene paper for exceptional EMI shielding

performance using large-sized graphene oxide sheets and doping strategy, Carbon 122, (2017), 74-81.

[105] F. Ruffino, V. Torrisi, R. Grillo, G. Cacciato, M. Zimbone, G. Piccitto, M.G. Grimaldi, Nanoporous Au structures by dealloying Au/Ag thermal- or laser-dewetted bilayers on surfaces, Superlattices and Microst. 103, (2017), 28-47.

[106] A.C. Ferrari, D.M. Basko, Raman spectroscopy as a versatile tool for studying the properties of graphene. Nat. Nanotechnol. 8, (2013), 235–246.

[107] L. D'Urso, G. Compagnini, O. Puglisi, A. Scandurra, and R.S. Cataliotti, Vibrational and Photoelectron Investigation of Amorphous Fluorinated Carbon Films, J. Phys. Chem. C 111, (2007), 17437–17441.

[108] P. Klar, E. Lidorikis, A. Eckmann, I.A. Verzhbitskiy, A.C. Ferrari, and C. Casiraghi, "Raman scattering efficiency of graphene", Phys. Rev. B 87, (2013), 205435.

[109] A.C. Ferrari, "Raman spectroscopy of graphene and graphite: Disorder, electron–phonon coupling, doping and nonadiabatic effects", Solid State Commun. 43, (2007), 47–57.

[110] A.C. Ferrari, J.C. Meyer, V. Scardaci, C. Casiraghi, M. Lazzeri, F. Mauri, S. Piscanec, D. Jiang, K.S Novoselov, S. Roth, "Raman spectrum of graphene and graphene layers", Phys. Rev. Lett. 97, (2006), doi:10.1103/PhysRevLett.97.187401.

[111] C. Ferrante, A. Virga, L. Benfatto, M. Martinati, D. De Fazio, U. Sassi, C. Fasolato, A. K. Ott, P. Postorino, D. Yoon, G. Cerullo, F. Mauri, A. C. Ferrari and T. Scopigno, "Raman spectroscopy of graphene under ultrafast laser excitation", Nat. Commun. 9, 308 (2018) doi:10.1038/s41467-017-02508-x.

[112] F. Tuz Johra, J.-W. Lee, W.-G. Jung, Facile and safe graphene preparation on solution based platform, J. Ind. Eng. Chem. 20, (2014), 2883–2887.

[113] E. Ziambaras, J. Kleis, E. Schröder, P. Hyldgaard, Potassium intercalation in graphite: A van der Waals density-functional study. Phys. Rev. B 76, (2007), 155425.

[114] M. Zhou,; Y. Zhai, S. Dong, Electrochemical sensing and biosensing platform based on chemically reduced graphene oxide. Anal. Chem. 81, (2009), 5603–5613.

[115] J.E.B. Randles, Kinetics of rapid electrode reactions. Part 2.—Rate constants and activation energies of electrode reactions. Trans. Faraday Soc. 48, (1952), 828–832.

[116] R.N. Adams, Electrochemistry at Solid Electrodes; Marcel-Dekker: New York, NY, USA, 1969.

[117] R.S. Nicholson, Theory and application of cyclic voltammetry for measurement of electrode reaction kinetics. Anal. Chem. 37, (1965), 1351–1355.

[118] R.O. Kadara, N. Jenkinson, C.E. Banks, Characterisation of commercially available electrochemical sensing platforms. Sens. Actuators B Chem. 138, (2009), 556–562.

[119] L. Zhang, F. Cosandey, R. Persaud, T. E. Madey, Initial growth and morphology of thin Au films on TiO2 (110), Surf. Sci. 439, (1999), 73–85.

[120]D.R. Lide, ed., Handbook of Chemistry and Physics, 2005, CRC Press, Boca Raton, FL.

[121] S. Namsani and J. K. Singh, “Dewetting dynamics of a gold film on graphene: implications for nanoparticle formation”, Faraday Discuss. 186, (2016), 153-170.

[122] A. Nikitin, L. Näslund, Z. Zhang, A. Nilsson, C–H bond formation at the graphite surface studied with core level spectroscopy, Surf. Sci. 602, (2008), 2575–2580.

[123] J.A.Leiro, M.H. Heinonen, T. Laiho, I.G. Batirev, Core-level XPS spectra of fullerene, highly oriented pyrolytic graphite, and glassy carbon. J. Electron. Spectrosc. Relat. Phenom. 128, (2003), 205–213.

[124] V. Yong, H.T. Hahn, Synergistic effect of fullerene-capped gold nanoparticles on graphene electrochemical supercapacitors. Adv. Nanopart. 2, (2013), 1–5.

[125] A.M. García, A.J. Hunt, V.L. Budarin, H.L. Parker, P.S. Shuttleworth, G.J. Ellis, J.H. Clark, Starch-derived carbonaceous mesoporous materials (Starbon®) for the selective adsorption and recovery of critical metals. Green Chem. 17, (2015), 2146–2149.

[126] A.Y. Klyushin, T.C.R. Rocha, M. Hävecker, A. Knop-Gericke, R. Schlögl, A near ambient pressure XPS study of Au oxidation. Phys. Chem. Chem. Phys. 16, (2014), 7881–7886.

[127] M. Pasta, F. La Mantia, Y. Cui, Mechanism of glucose electrochemical oxidation on gold surface, Electrochim. Acta 55, (2010), 5561–5568.

[128] R. S. Sundaram, M. Steiner, H-Y. Chiu, M. Engel, A. A. Bol, R. Krupke, M. Burghard, K. Kern and P. Avouris, “The Graphene-Gold Interface and Its Implications for Nanoelectronics”, Nano Lett. 11, (2011), 3833–3837.

[129] V. Buk, M. E. Pemble, A highly sensitive glucose biosensor based on a micro disk array electrode design modified with carbon quantum dots and gold nanoparticles, Electrochim. Acta 298, (2019), 97-105.

[130] D. Branagan and C.B. Breslin, Electrochemical detection of glucose at physiological pH using gold nanoparticles deposited on carbon nanotubes, Sens. Actuators B Chem. 282, (2019), 490–499.

[131] V. Buk, M.E. Pemble, K. Twomey, Fabrication and evaluation of a carbon quantum dot/gold nanoparticle nanohybrid material integrated onto planar micro gold electrodes for potential bioelectrochemical sensing applications, Electrochimica Acta 293 (2019) 307-317.

[132] T. Siepenkoetter, U. Salaj-Kosla and E. Magner, The Immobilization of Fructose Dehydrogenase on Nanoporous Gold Electrodes for the Detection of Fructose ChemElectroChem 4, (2017), 905-912.

[133] S. Campuzano, R. Gálvez, M. Pedrero, F. el deVillena, J. M. Pingarrón, An integrated electrochemical fructose biosensor based on tetrathiafulvalene-modified self-assembled monolayers on gold electrodes, Anal. Bioanal. Chem. 377, (2003), 600–607 doi 10.1007/s00216-003-2123-7.

[134] R. Antiochia, L. Gorton, A new osmium-polymer modified screen-printed graphene electrode for fructose detection, Sens. Actuators B chem. 195, (2014), 287–293.

[135] J. Biscay, E. Cista Rama, M. Begona Gonzalez Garcia, A.J. Reviejo, J.M. PingarronCarrazon, A. Costa Garcia, Amperometric fructose sensor based on ferrocyanide modified screen-printed carbon electrode, Talanta 88, (2012), 432–438.

[136] N. Stozhko, M. Bukharinova, L. Galperin and K, Brainina, A Nanostructured Sensor Based on Gold Nanoparticles and Nafion for Determination of Uric Acid, Biosensors 8, (2018), 21; doi:10.3390/bios8010021.

[137] M. Reuben, A. Elliott, Caspi, Implications of legacy lead for children's brain development, Nat. Med. 26, (2020), 23–25 doi:10.1038/s41591-019-0731-9.

[138] International Programme on Chemical Safety: cadmium. Available online: www.who.int/ipcs/assessment/public_health/cadmium/en/ (Accessed on 15 August 2020).

[139] Lead poisoning and health. Available online: www.who.int/news-room/fact-sheets/detail/lead-poisoning-and-health (Accessed on 15 August 2020).

[140] EPA's 2018 Edition of the Drinking Water Standards and Health Advisories Tables. Available online: https://nepis.epa.gov/ (Accessed on 15 August 2020).

[141] European Council Directive 98/83/EC of 3 November 1998 on the quality of water intended for human consumption. Available online: https://eur-lex.europa.eu/ (Accessed on 15 August 2020).

[142] K. Julshamn, A. Maage, H. S. Norli, K. H. Grobecker, L. Jorhem, P. Fecher, Determination of Arsenic, Cadmium, Mercury, and Lead by Inductively Coupled Plasma/Mass Spectrometry in Foods after Pressure Digestion: NMKL Interlaboratory Study, Journal of AOAC Int. 90, (2007), 844.

[143] C. Brombach, B. Chen, Warren T. Corns, J. Feldmann, E. M. Krupp, Methylmercury in water samples at the pg/L level by online preconcentration liquid chromatography cold vapor-atomic fluorescence spectrometry, Spectrochim. Acta B 105, (2015), 103–108, http://dx.doi.org/10.1016/j.sab.2014.09.014.

[144] S.H. Yu, C. Lee and T.H. Kim, Electrochemical Detection of Ultratrace Lead Ion through Attaching and Detaching DNA Aptamer from Electrochemically Reduced

Graphene Oxide Electrode, Nanomaterials 9, (2019), 817 doi:10.3390/nano9060817.

[145] H. Huang, T. Chen, X.L.H. Ma, Ultrasensitive and simultaneous detection of heavy metal ions based on three-dimensional graphene-carbon nanotubes hybrid electrode materials, Anal. Chim. Acta 852, (2014), 45–54, http://dx.doi.org/10.1016/j.aca.2014.09.010.

[146] S. Frutos-Puerto, C. Miró and E. Pinilla-Gil, Nafion-Protected Sputtered-Bismuth Screen-Printed Electrode for On-site Voltammetric Measurements of Cd(II) and Pb(II) in Natural Water Samples, Sensors 19, (2019), 279 doi:10.3390/s19020279.

[147] Y. Lu, X. Liang, C. Niyungeko, J. Zhou, J. Xu, G. Tian, A review of the identification and detection of heavy metal ions in the environment by voltammetry, Talanta 178, (2018), 324–338 http://dx.doi.org/10.1016/j.talanta.2017.08.033.

[148] J. Wang, J. Lu, S. B. Hocevar, and P. Farias, Bozidar Ogorevc, Bismuth-Coated Carbon Electrodes for Anodic Stripping Voltammetry, Anal. Chem., 72, (2000), 3218-3222.

[149] A. Economou, Bismuth-film electrodes: recent developments and potentialities for electroanalysis, Trends in Analytical Chemistry, 24, (2005), 334-340 DOI: 10.1016/j.trac.2004.11.006.

[150] N. Serrano, J. Diaz-Cruz, C. Ariño, M. Esteban, Ex situ Deposited Bismuth Film on Screen-Printed Carbon Electrode: A Disposable Device for Stripping Voltammetry of Heavy Metal Ions, Electroanalysis 22, (2010), 1460 – 1467.

[151] G. Zhao, H. Wang and G. Liu, Sensitive determination of trace Cd(II) and Pb(II) in soil by an improved stripping

voltammetry method using two different in situ plated bismuth-film electrodes based on a novel electrochemical measurement system, RSC Adv. 8, (2018), 5079.

[152] J. Sochr, M. Machková, L. Machyňák, F. Čacho, L. Švorc, Heavy metals determination using various in situ bismuth film modified carbon-based electrodes, Acta Chim. Slov., 9, (2016), 28—35, doi: 10.1515/acs-2016-0006.

[153] G. Zhao, Y. Yin, H. Wang, G. Liu, Z. Wang, Sensitive stripping voltammetric determination of Cd(II) and Pb(II) by a Bi/multi-walled carbon nanotube-emeraldine base polyaniline-Nafion composite modified glassy carbon electrode, Electrochim. Acta 220, (2016), 267–275.

[154] G. Kefala, A. Economou, A. Voulgaropoulos, M. Sofoniou, A study of bismuth-film electrodes for the detection of trace metals by anodic stripping voltammetry and their application to the determination of Pb and Zn in tap water and human hair, Talanta 61, (2003), 603-610.

[155] L. Xiao, B. Wang, L. Jic, F. Wang, Qunhui Yuand, Guangzhi Hu, Angang Dong, Wei Gan, An efficient electrochemical sensor based on three-dimensionally interconnected mesoporous graphene framework for simultaneous determination of Cd(II) and Pb(II), Electrochim. Acta 222, (2016), 1371–1377.

[156] A. Alam, M. Howlader, N. Hu, M. J. Deen, Electrochemical sensing of lead in drinking water using β-cyclodextrin modified MWCNTs, Sens. Actuators B Chem. 296, (2019), 126632.

[157] R. María-Hormigos, M. Gismera, J. R. Procopio, M. Sevilla, Disposable screen-printed electrode modified

with bismuth–PSS composites as high sensitive sensor for cadmium and lead determination, J. Electroanal. Chem. 767, (2016), 114–122.

[158] F. Salih, A. Ouarzane, M. Rhazi, Electrochemical detection of lead (II) at bismuth/Poly(1,8-diaminonaphthalene) modified carbon paste electrode, Arab. J. Chem. 10, (2017), 596–603, http://dx.doi.org/10.1016/j.arabjc.2015.08.021.

[159] R.L. McCreery, Advanced carbon electrode materials for molecular electrochemistry. Chem. Rev. 108, (2008), 2646–2687.

[160] A. Scandurra, F. Ruffino, S. Sanzaro, M.G. Grimaldi, Laser and thermal dewetting of gold layer onto graphene paper for non-enzymatic electrochemical detection of glucose and fructose. Sens. Actuators B Chem. 301, (2019), 127113, doi:10.1016/j.snb.2019.127113.

[161] R. Segura, J. A. Pizarro, M. P. Oyarzun, A. D. Castillo, K. J. Díaz, A. B. Placencio, Determination of Lead and Cadmium in Water Samples by Adsorptive Stripping Voltammetry Using a Bismuth film/1-Nitroso-2-Napthol/Nafion Modified Glassy Carbon Electrode, Int. J. Electrochem. Sci., 11, (2016), 1707 – 1719.

[162] S. K. Pandey, S. Sachan, S. K. Singh, Ultra-trace sensing of cadmium and lead by square wave anodic stripping voltammetry using ionic liquid modified graphene oxide, Mat. Sci. Energy Technol. 2, (2019), 667–675.

[163] H. Xu, L. Zeng, D. Huang, Y. Xian, L. Jin, A Nafion-coated bismuth film electrode for the determination of heavy metals in vegetable using differential pulse anodic stripping voltammetry: An alternative to mercury-based electrodes, Food Chem. 109, (2008), 834–839.

[164] S. Lee, S. Bong, J. Ha, M. Kwak, S. Park, Y. Piao, Electrochemical deposition of bismuth on activated graphene-nafion composite for anodic stripping voltammetric determination of trace heavy metals, Sens. Actuators B Chem. 215 ,(2015), 62–69.

[165] S. Palisoc, V. A. Sowa and M. Natividad, Fabrication of a bismuth nanoparticle/Nafion modified screen-printed graphene electrode for in situ environmental monitoring, Anal. Methods, 11, (2019), 1591, 0.1039/c9ay00221a.

[166] N. Mau Thanh, N. Dinh Luyen, T. Thanh Tam Toan, N. Hai Phong, N. Van Hop, Voltammetry Determination of Pb(II), Cd(II), and Zn(II) at Bismuth Film Electrode Combined with 8-Hydroxyquinoline as a Complexing Agent, J. of Anal. Methods in Chem. Vol. 2019, 1-11, Article ID 4593135 https://doi.org/10.1155/2019/4593135.

[167] L. Baldrianova, P. Agrafiotou, I. Svancara, A.D. Jannakoudakis, S. Sotiropoulos, The effect of acetate concentration, solution pH and conductivity on the anodic stripping voltammetry of lead and cadmium ions at in situ bismuth-plated carbon microelectrodes, J. Electroanal. Chem. 660, (2011), 31–36, doi:10.1016/j.jelechem.2011.05.028.

[168] C. N. Tharamani, H. C. Thejaswini and S. Sampath, Synthesis of size-controlled Bi particles by electrochemical deposition, Bull. Mater. Sci., 31, (2008), 207–212.

[169] E. C. Walter, M. P. Zach, F. Favier, B. J. Murray, K. Inazu, J. C. Hemminger, and R. M. Penner, Metal Nanowire Arrays by Electrodeposition, ChemPhysChem, 4, (2003), 131-138.

[170] H. Zhou, H. Hou, L. Dai, Y. Li, J. Zhu, L.Wang, Preparation of dendritic bismuth filmelectrodes and

their application for detection of trace Pb (II) and Cd (II), Chin. J. Chem. Eng., 24, (2016), 410–414, http://dx.doi.org/10.1016/j.cjche.2015.08.012.

[171] J. Saturno, D. Valera, H. Carrero, L. Fernández, Electroanalytical detection of Pb, Cd and traces of Cr at micro/nano-structured bismuth film electrodes, Sens. Actuators B Chem. 159, (2011), 92– 96, 10.1016/j.snb.2011.06.055.

[172] E. Desimoni and B. Brunetti, About Estimating the Limit of Detection by the Signal to Noise Approach, Pharm Anal Acta, 6, (2015), 355, doi: 10.4172/2153-2435.1000355.

[173] Q. Zeng, Y. Li, K. Wu, N. Huang, S. Dalapati, B. Su, L. Jang, I.R. Gentle, D. Jiang, D. Wang, Long-chain solid organic polysulfide cathode for high-capacity secondary lithium batteries, Energy Storage Mater. 12, (2018), 30–36.

[174] I. L. Lagadic, M. K. Mitchell, B. D. Payne, Highly Effective Adsorption of Heavy Metal Ions by a Thiol-Functionalized Magnesium Phyllosilicate Clay, Environ. Sci. Technol. 35, (2001), 984-990, https://doi.org/10.1021/es001526m.

[175] S. Suzer, Differential Charging in X-ray Photoelectron Spectroscopy: A Nuisance or a Useful Tool?, Anal. Chem. 75, (2003), 7026-7029.

[176] A. Scandurra, A. Cavallaro, S. Pignataro, R. Tiziani, L. Gobbato, C. Cognetti, Curing and electrical conductivity of conductive glues for die attach in microelectronics, Surf. Interf. Anal., 38, (2006), 429-432, doi: 10.1002/sia.2164.

[177] X-ray Photoelectron Spectroscopy (XPS) Reference Pages. Available online: www.xpsfitting.com (Accessed on 4 February 2020).

List of publications and talks at conferences

[1] Antonino Scandurra, Francesco Ruffino, Mario Urso, Maria Grazia Grimaldi and Salvo Mirabella, Disposable and low cost electrode based on graphene paper-nafion-Bi nanostructures for ultra-trace analysis of Pb(II) and Cd(II), Special Issue "Development and Evaluation of Nanostructured Electrochemical Sensors", Nanomaterials 10, (2020), 1620; https://doi.org/10.3390/nano10081620

[2] Antonino Scandurra, Francesco Ruffino, Maria Censabella, Antonio Terrasi, and Maria Grazia Grimaldi, Dewetted Gold Nanostructures onto Exfoliated Graphene Paper as High Efficient Glucose

Sensor, Special Issue Carbon-Based Nanostructures and Nanocomposites for Health and Environmental Applications, Nanomaterials 9, (2019), 1794, https://doi.org/10.3390/nano9121794

[3] Antonino Scandurra, Francesco Ruffino Salvatore Sanzaro and Maria Grazia Grimaldi, Laser and Thermal Dewetting of Gold Layer onto Graphene Paper for non-Enzymatic Electrochemical Detection of Glucose and Fructose, Sens. Actuators B Chem., 301, (2019), 127113, https://doi.org/10.1016/j.snb.2019.127113

[4] Antonino Scandurra, Francesco Ruffino and Maria Grazia Grimaldi, Graphene Paper-Gold Nanostructured Electrodes Obtained by Laser Dewetting for High Sensitive Non-Enzymatic Glucose Sensing, Proceedings of the 7th International Symposium on Sensor Science, 15, (2019); https://doi.org/10.3390/proceedings2019015001

[5] Antonino Scandurra, Elena Bruno, Guglielmo Guido Condorelli, Maria Grazia Grimaldi and Salvatore Mirabella, Microscopic Model for pH Sensing Mechanism in Zinc-based Nanowalls, Sens. Actuators B Chem. 296, (2019), 126614, https://doi.org/10.1016/j.snb.2019.05.091

[6] Emanuele Luigi Sciuto, Corrado Bongiorno, Antonino Scandurra, Salvatore Petralia, Tiziana Cosentino, Sabrina Conoci, Fulvia Sinatra, Sebania Libertino, Functionalization of Bulk SiO_2 Surface with Biomolecules for Sensing Applications: Structural and Functional Characterizations, Chemosensors 6, (2018), 59, https://doi.org/10.3390/chemosensors6040059

[7] Salvatore Petralia, Emanuele L Sciuto, Maria Anna Messina, Antonino Scandurra, Salvatore Mirabella, Francesco Priolo, Sabrina Conoci, Miniaturized and multi-purpose electrochemical sensing device based on thin Ni oxides, Sens. Actuators B Chem., 263, (2018) 10-19; https://doi.org/10.1016/j.snb.2018.02.114

Talks at Conferences

[1] A. Scandurra, M. Urso, M.G. Grimaldi and S. Mirabella, Graphene paper-perfluorosulfonic ionomer-Bi composite electrode for stripping voltammetry determination of sub-ppb level of Pb^{2+} and Cd^{2+} in solution, 8th International Symposium on Sensor Science, accepted for oral presentation, postponed to 26-28 May, 2021, Dresden, Germany

[2] A. Scandurra, M. Urso, M.G. Grimaldi and S. Mirabella, Ultra trace analysis of Pb^{2+} and Cd^{2+} in drinking water by SWASV employing graphene paper-perfluorosulfonic ionomer-Bi composite electrode, accepted for oral presentation to the Sensors Europe 2020, Berlin, Germany, date to be defined

[3] Antonino Scandurra, Francesco Ruffino and Maria Grazia Grimaldi, Non-Enzymatic Electrochemical Glucose Sensing by Gold Nanostructures onto Graphene Paper Obtained by Laser Dewetting, submitted to FisMat 2019, Italian National Conference on the Physics of Matter, September 30, October 4, 2019, Catania, Italy

[4] Antonino Scandurra, Elena Bruno, Guglielmo Guido Condorelli, Maria Grazia Grimaldi and Salvatore Mirabella, Structure-based Modeling of pH Sensing in Zinc-based Nanowalls, submitted to FisMat 2019, Italian National Conference on the Physics of Matter, September 30, October 4, 2019, Catania, Italy

[5] Antonino Scandurra, Francesco Ruffino and Maria Grazia Grimaldi, Graphene Paper-Gold Nanostructured Electrodes Obtained by Laser Dewetting for High Sensitive Non-Enzymatic Glucose Sensing, presented at

the 7th International Symposium on Sensor Science 9–11 May 2019, Napoli, Italy

Full list at https://scholar.google.com/citations; https://orcid.org/0000-0002-5281-5776

BIOGRAPHY

Antonino Scandurra received his diploma in industrial chemistry (EQF-L5) at the public Institute *"Stanislao Cannizzaro"* in 1982 and his graduation degree in chemistry in 1988 at the Catania University, Italy. From 1989 to 1990 he was a research fellow at the Institute for Microelectronics and Microsystems of National Research Council of Italy (CNR). He has been a senior scientist at the Consorzio Catania Ricerche (Italy) since 1993 until 2015. He is authors of about 80 research papers published in peer-reviewed international journals in the field of surface physical-chemistry, material science and nanotechnology applied to microelectronics, sensors and biosensors. He has been a PhD candidate at the Material Science and Nanotechnology course at the

Department of Physics and Astronomy *"Ettore Majorana"* of Catania University in the 2017-2020.